Understanding Low Work Function Perovskite Thermionic Emission Materials

by

Lin Lin

A dissertation submitted in partial fulfillment of

the requirements for the degree of

Doctor of Philosophy

(Materials Science and Engineering)

at the

UNIVERSITY OF WISCONSIN-MADISON

2022

Date of final oral examination: 8/15/2022

The dissertation is approved by the following members of the Final Oral Committee:

Dane Morgan, Professor, Materials Science and Engineering
John Booske, Professor, Electrical and Computer Engineering
Ryan Jacobs, Scientist II, Materials Science and Engineering
Jason Kawasaki, Assistant Professor, Materials Science and Engineering
Song Jin, Professor, Chemistry

Acknowledgement

My 6-year research for pursuing my Ph.D. was filled with challenges and exiting moments, eventually reaching this stage with shining outcomings. There are so many people to thank when looking back to this journey.

First, I would like to thank my advisors, Prof Dane Morgan and Prof John Booske. You are excellent advisors, not only teaching me abundant science knowledge, but also mentoring me how to do research and how to deal with challenging problems. I would like to thank Dr Ryan Jacobs with all the advice and continuous support on my research and life. Of course, I would like to thank Prof Jason Kawasaki and Prof Song Jin to be on my committee and the valuable input on this dissertation.

I would like to thank my colleagues and good friends, Dr Dongzheng Chen and Dr Tianyu Ma. We worked on the INVEST project for years with thoughtful discussions on scientific aspects, as well as the help on setting up and maintaining normal operation of lab equipment and releasing mental pressure when research was not going smoothly. I really appreciated Dr Qiang Zheng's help on experimental development of perovskite synthesis and knowledges on vacuum electronics. I would like to thank Dr Md Sariful Sheikh on the help on lab instrumentations, perovskite synthesis and testing, as well as thoughtful discussions on perovskites.

During my Ph.D. research I had chances to work with a lot of amazing collaborators. I would like to thank Prof Martin Kordesch on the continuous support of the thermionic emission testing heaters help on PEEM and ThEEM experiments, as well as the discussion on emission physics. I would like to thank the help from Prof Jason Kawasaki on UPS

instrumentation (although not finally used in my experiments) and insightful discussion on photoemission spectroscopy. I would also like to thank my other collaborators and supporters, Prof Jose A. Alonso, Dr Bernard Vancil, Prof John Balk, Prof John Perepezko, Prof Paul Evans, Dr Samuel Marks, Dr Patrick Strohbeen, Dr Vasilios Vlahos, and Dr Otto Lu-Steffes.

Meanwhile, I would like to thank the funding agencies supporting my research, to make things happen. These include Defense Advanced Research Projects Agency (DARPA) through the Innovative Vacuum Electronic Science and Technology (INVEST) program, the Wisconsin Alumni Research Foundation (WARF), the facilities and instrumentation at the UW-Madison Wisconsin Centers for Nanoscale Technology (wcnt.wisc.edu) partially supported by the National Science Foundation (NSF) through the University of Wisconsin Materials Research Science and Engineering Center (MRSEC) (DMR-1720415) and Characterization Facility of University of Minnesota partially supported by NSF through the MRSEC (DMR-2011401) and the National Nanotechnology Coordinated Infrastructure (NNCI) (ECCS-2025124) programs.

Finally, I would like to thank the constant support from my parents Shaotian Lin and Shuhui Liu, my family, as well as my friends. Most importantly, I could not say enough thanks to my soul mate and fiancé Dr Jianing Li for the support and love along the journey of pursuing Ph.D. degrees together. This dissertation is dedicated to you.

Contents

Abstract

Work function, the surface energy barrier for electron migration towards vacuum, is one of the most important properties in science and technology involving material surfaces and interfaces such as vacuum and solid-state electronics, catalysis, energy harvesting, etc. However, there has been widely existing confusion on work function definition, measurement, and interpretation.

Pursuing lower work function emitters is particularly crucial for thermionic emission cathodes used in vacuum electronics, as it will boost the emission performance, especially with intrinsically polar materials such as perovskite oxides, since it is possible with these materials to overcome shortcomings of contamination and lifetime existing in current dispenser cathodes. However, the experimentally measured work functions of the perovskites are generally much higher than the DFT predictions, leaving a question on whether such proposed polar material idea is practical.

In this dissertation, deeper understanding of work function physics has been developed with an electrostatic energy treatment, together with the realization of the roles of external and patch fields. Such treatment clarifies the confusions in interpreting the work function definition and measurements. Also, the work function is understood as the benchmark for relative energy level alignment that is critical in a vast array of applications, and the two main strategies of tuning work functions, namely tuning bulk electronic structures and surface dipoles, are emphasized.

The experimental demonstrations of low work function perovskites $SrVO_3$ and $BaMoO_3$ have benefited a lot from the development fundamental understanding of work

function. Particularly, with the recognition and proper treatment on surface oxidation and patch field effect, $SrVO_3$ has shown low 2.3 to 2.7 eV effective work function with thermionic emission, which is the lowest work function observed from a bulk monolithic conductive oxide material, promising for work function engineering including thermionic emission applications. $BaMoO_3$ indicated multi-scale patch fields, with the micron-scale patch field being fully overcome, further proving the patch field theory. On the other hand, significant phase transformation that might be associated with Ba migration similar as dispenser cathodes is observed, possibly suggesting a simpler approach for cathode fabrication, although future research is still necessary to more thoroughly understand the properties of $BaMoO_3$.

List of Peer-reviewed Publications during Ph.D.

L. Lin, R. Jacobs, D. Chen, V. Vlahos, O. Lu-Steffes, J. A. Alonso, D. Morgan and J. Booske, "Demonstration of low work function perovskite $SrVO_3$ using thermionic electron emission", *Advanced Functional Materials* (2022).

L. Lin, R. Jacobs, T. Ma, D. Chen, J. Booske, and D. Morgan, "Work function: Fundamentals, measurement, calculation, engineering, and applications", in the revision and resubmission process with *Physical Review Applied.*

S. D. Marks, **L. Lin**, P. Zuo, P. J. Strohbeen, R. Jacobs, D. Du, J. R. Waldvogel, R. Liu, D. E. Savage, J. H. Booske, J. K. Kawasaki, S. E. Babcock, D. Morgan, and P. G. Evans. "Solid-phase epitaxial growth of the correlated-electron transparent conducting oxide $SrVO_3$". *Physical Review Materials*, **5**, 8, 083402 (2021).

L. Lin, R. Jacobs, D. Morgan, and J. Booske. "Investigation on polycrystalline $BaMoO_3$ as a thermionic emitter". In preparation.

List of Conference Presentations and Papers

L. Lin, R. Jacobs, D. Morgan, and J. Booske. "Heterogeneous cathode work function measurement and interpretation: A case study with $SrVO_3$". *IEEE International Conference on Vacuum Electronics (IVEC)*, (2022). (April 2022, Monterey, CA)

S. Marks, **L. Lin**, P. Zuo, P. Strohbeen, R. Jacobs, D. Du, J. Waldvogel, R. Liu, D. Savage, S. Babcock, J. Kawasaki, J. Booske, D. Morgan, and P. Evans. "High transparent conductor figure-of-merit in SrVO3 grown by solid-phase epitaxy". *Bulletin of the American Physical Society*, (2022). (Co-authored conference paper)

L. Lin, R. Jacobs, S. D. Marks, P. G. Evans, D. Morgan, and J. Booske. "Experimental Investigation of Bulk and Thin Film Perovskite $SrVO_3$ as a Thermionic Cathode Material". *IEEE 21st International Conference on Vacuum Electronics (IVEC)*, 161, (2020). (October 2020, virtual)

L. Lin, R. Jacobs, D. Morgan, and J. Booske. "Realizing Bulk, Stable Low Work Function Perovskite Materials". Poster in *Material Research Society Fall meeting*, (2019). (December 2019, Boston, MA)

L. Lin, R. Jacobs, D. Chen, V. Vlahos, O. Lu-Steffes, D. Morgan and J. Booske, "Experimental Development of Perovskite $SrVO_3$ Thermionic Emission Cathodes". Oral presentation in *Joint IEEE International Vacuum Nanoelectronics Conference (IVNC) and International Vacuum Electron Source Conference (IVESC)*, (2019). (July 2019, Cincinnati, OH)

R. Jacobs, **L. Lin**, T. Ma, O. Lu-Steffes, V. Vlahos, D. Morgan, and J. Booske. "Perovskite electron emitters: Computational prediction and preliminary experimental

assessment of novel low work function cathodes". *IEEE International Conference on Vacuum Electronics (IVEC)*, 37, (2018). (Co-authored conference paper)

List of Figures

and smoothing effect of electron clouds[32], creating dipole moments on a simple metal. (d) The atomic structure of a perovskite, an example of polar materials where the AO- and BO2-terminated surfaces have opposite surface atomic arrangements and therefore opposite dipoles (From Ref. 67 ©2016 John Wiley & Sons, Inc.). (e) DFT-calculated platinum electrode's work function dependence on different adsorbed halide functional groups (from Ref. 143. Copyright: open access, credit to the original authors).

Fig 2.7. (a) A set of real data for UPS-measured ITO work function (reprinted from Ref. 148 with the permission of AIP Publishing). (b) Measured work function with UPS on a heterogeneous surface with weak field, resulting in an average value across the surface (from Ref. 149 ©2017 John Wiley & Sons, Inc). (c) An example of PEEM image on polycrystalline copper (from Ref. 162 ©2006 John Wiley & Sons, Inc.), with different work functions indicated by brightness differences. This suggests the local work functions for microscopic grains are resolvable under high applied field. (d) An example of KPFM work function mapping for a heterogeneous surface (from Ref. 149 ©2017 John Wiley & Sons, Inc). The zebra-crossing pattern deposited with two different organic molecules, namely FSH and CSH, have a local work function difference of 1 eV, which is directly detectable via KPFM.

Fig 2.8. Simulation and fitting of the thermionic emission from a heterogeneous cathode with a checkerboard work function distribution, inspired by Dr Dongzheng Chen's Ph.D. dissertation[178] with different numerical values inserted. (a) The surface work function distribution and anode setup. The surface consists of 10 μm patches with 4 eV and 2 eV local work functions. (b) The simulated current density, full space charge limited current density and fitted curve for low temperature region, clearly showing a fitted work function (1.6 eV) much lower than any surface local work function, and a very small A (10^{-3} of the theoretical value). (c) The classical fitting procedure for the simulated emission current density by plotting $\ln(J/T^2)$ versus $1/T$ and linearly fitting the low temperature part.

Fig 3.1. (a) Stability phase diagram of SrVO3 calculated through DFT (from Marks et al.[236]), with pellet sintering, over-reducing and emission testing conditions labeled as A, B and C, respectively. Reprinted figure with permission from Marks et al., *Phys. Rev. Mater. 5*, 83402, 2021. Copyright (2021) by the American Physical Society. (b) Plotted logarithm of the equilibrium constant of water formation reaction using values reported by Wagman et al.[237] The original data set was up to 1500K, and the trend curve is the fitting result towards Van 't Hoff equation (Eq. 3.2).

Fig 3.2. (a) Schematic diagram of thermionic emission testing fixture, chamber, circuit and optics for temperature measurement. (b) The photograph of the e-beam heater. (c) The photograph of the anode fixture. (d) A snapshot of one set of emission current and grid voltage data point. The large spikes in the emission current right after the pulse on and off

are due to the capacitor charging and discharging. The non-zero current at a stable non-zero pulse bias on the grid is the actual measured emission current.

Fig 3.3. (a) Powder XRD data for polycrystalline $SrVO_3$ with retrieved record from database, showing a high phase purity. (b) Morphology of the sintered polycrystalline $SrVO_3$ pellet captured by SEM, suggesting the possible existence of (001) surfaces in comparison with Wulff shape predicted by DFT. The typical observed grain size is estimated to be between 0.5 to 2 μm. (c) XRD results for the top region of an over-reduced sample and the region beneath the top. The Top region contains perovskite $SrVO_3$, over-reduced phase Sr_2VO_4, as well as VN or VO. The region beneath contains mainly $SrVO_3$ with a very small amount of VN or VO. (d) SEM image of the top surface and cross-sectional profile of an over-reduced pellet, showing the over-reduced region serving as a capping layer on top of the perovskite beneath, with a thickness of ~1 μm.

Fig 3.4. The XPS results of an $SrVO_3$ pellet. (a) The survey scan, with the corresponding atomic concentration summarized. (b) The vanadium core level scan before and after Ar^+ ion sputter-etching, with peak fitting processed by CasaXPS software, showing a predominantly V^{5+} component before etching and a majority of V^{4+} component after etching off the top few nanometers, suggesting that the over-oxidation is limited within the near-surface region.

Fig 3.5. The work function measurement and thermionic emission test results on $SrVO_3$ pellets. (a) The UPS measured bias-corrected secondary electron cutoffs on an as-sintered pellet, and a pellet after Ar^+ ion sputter-etching plus annealing at 700 ˚C for 0.5 h, and after cooling down, suggesting 3.45, 4.06, and 4.07 eV, respectively. It is not unexpected that these values do not match the DFT prediction due to surface contamination and patch field effect. (b) The thermionic emission *J-V* plots from an over-reduced and cleaved sample at different temperatures, suggesting an increasing emission current as A-K voltage becomes larger, consistent with the patch field effect. (c) The thermionic emission *J-T* plots of several over-reduced-and-cleaved samples within the temperature-limited regime, with datasets #1 to #7 collected at 1.5 kV A-K voltage, and the A-K voltage of #8 unknown. These datasets indicate an *effective* 2.7 eV work function under the testing condition together with a few samples showing an *effective* work function close to 2.3 eV.

Fig 3.6. The reproducibility testing of a $SrVO_3$ thermionic emitter sample. The sample was heated up and tested for 3 cycles, labelled as Runs #1, #2 and #3. The theoretical RLD equations with 2.7, 2.8 and 2.9 eV work functions are also plotted for reference.

Fig 3.7. (a) Plots of the calculated $SrVO_3$ slab surface energies for various surfaces under Sr-rich limit. The vertical blue dashed lines denote approximate O chemical potential values representative of the experimental $SrVO_3$ processing condition, thermionic emission

test condition, XPS characterization condition, and room condition. The detailed structures of these surfaces are introduced in Section 5. (b) The calculated Wulff construction shapes under the Sr-rich limit considering the lowest energy (001)-, (011)-, and (111)-oriented surface terminations under thermionic emission condition. The red and blue colors denote (001) and (111) surface facets, respectively. Legend description: SVO_001_AO: native AO layer, SVO_001_BO2: native BO_2 layer, SVO_001_AO_double: AO double layer, SVO_001_AO_Ovac: AO surface + O vacancy, SVO_001_BO2_Ovac50: BO_2 surface + O vacancy, SVO_001_BO2_Ovac100: BO_2 surface + two O vacancies, SVO_001_AO_BO2_1uc: mixed AO and BO2 1 unit cell wide, SVO_001_AO_BO2_2uc; mixed AO and BO2 2 unit cells wide. SVO_011_ABO: native ABO-terminated surface, SVO_011_O: native O-terminated surface. SVO_111_AO3: native AO_3-terminated surface, SVO_111_B: native B-terminated surface, SVO_r2xr2: (001) $\sqrt{2} \times \sqrt{2}$ reconstruction, SVO_r5xr5: (001) $\sqrt{5} \times \sqrt{5}$ reconstruction.

Fig 3.8. (a) Comparison between $SrVO_3$'s emission current density and FSCL current density, suggesting the emission is mainly temperature-limited because J_{FSCL} is much higher than the emission data, and the data curves deviate from any straight $V^{3/2}$ lines. (b) Comparison between the ln$J$ vs $\sqrt{V}$ slopes of $SrVO_3$ and Schottky slopes with the same corresponding temperatures, showing that the Schottky slopes are much smaller than those of $SrVO_3$.

Fig 4.1. Stability phase diagram of $BaMoO_3$ calculated through DFT, also suggested a stable window for $BaMoO_3$.

Fig 4.2. The modification of the emission testing fixture for $BaMoO_3$ testing due to the Ba contamination issue. (a) The anode was a solid piece of W metal with a hole rather than a mesh grid, and the electron catcher was further extended. (b) Electron flow during emission testing. Only the emission from the area directly aligned with the anode hole (presumably $BaMoO_3$ sample) would be collected by the extended catcher.

Fig 4.3. (a) Powder XRD data for polycrystalline $BaMoO_3$ with retrieved record from database, showing a high phase purity. (b) Morphology of the sintered polycrystalline $BaMoO_3$ pellet captured by SEM, suggesting the possible existence of (001) surfaces by evaluating the facet shape. The typical observed grain size is estimated to be between 2 to 10 μm.

Fig 4.4. XPS results on as-sintered $BaMoO_3$ pellets. (a) Survey scan, showing the near-surface region contained Ba, Mo, O and C. (b) Mo 3d core level scan, indicating a mixed oxidation states of Mo 6+, 4+ and 0. The predominantly Mo 6+ suggested the surface was also over-oxidized during sample preparation and/or transition.

List of Tables

List of Abbreviations

2PPES: Two-photon photoelectron spectroscopy

A-K: Anode-cathode

AFM: Atomic force microscopy

CBM: Conduction band minimum

CPD: Contact potential difference

DFT: Density functional theory

EA: Electron affinity

EDS: Energy dispersive spectroscopy

F-N: Fowler-Nordheim

FSCL: Full spaced charge limit(ed)

GGA: Generalized gradient approximation

HER: Hydrogen evolution reaction

HOMO: Highest occupied molecular orbital

IE: Ionization energy

ITO: Indium tin oxide

KP: Kelvin probe

KPFM: Kelvin probe force microscopy

LUMO: Lowest unoccupied molecular orbital

NEA: Negative electron affinity

OER: Oxygen evolution reaction

ORR: Oxygen reduction reaction

PAX: Photoelectron spectroscopy of adsorbed xenon

PEEM: Photoemission electron microscopy

RLD: Richardson-Laue-Dushman

SEM: Scanning electron microscopy

TCO: Transparent conductive oxides

ThEEM: Thermionic emission electron microscopy

TL: Temperature limit(ed)

UHV: Ultrahigh vacuum

UPS: Ultraviolet photoelectron spectroscopy

VASP: Vienna *Ab Initio* Simulation Package

VBM: Valence band maximum

XPS: X-ray photoelectron spectroscopy

XRD: X-ray diffraction

Chapter 1 – General Introduction

Being the surface energy barrier of the electron migration, work function is one of the central properties in surface and interfacial science and engineering[1,2], which plays an important role in vacuum and solid-state electronics[3,4], (electro)catalysis[5], energy harvesting and conversion[6], as well as other critical application fields. However, despite the 100-year long history, the extreme importance, and the seemingly simple definition of work function, there is much confusion remaining in the work function definition and interpretation. Specifically, the existence of external electric field and surface heterogeneity often lead to contradictory understandings on the work functions of material surfaces, affecting the correct comprehension of the corresponding engineering fields[7–9]. In this dissertation, the physics of work function has been discussed in detail with an electrostatic energy profile treatment[1]. With the introduction of the *observed work function* and the careful consideration of the externally applied electric field and patch field effect induced by surface heterogeneity, an informative clarification on the work function measurement and interpretation confusion has been provided. Additionally, a systematic review of the role of work function in various applications has been provided in terms of relative energy level alignment, and the basic strategies of work function tuning mechanisms have been discussed, which is a promising strategy for performance improvements in various applications.

One specific application of work function engineering is thermionic electron emitters used in vacuum electronic devices including electron beam lithography, electron microscopes, gyrotrons, klystrons, traveling wave tubes, etc.[3], where a low work function is desirable for boosting the device performance by enabling higher brightness electron

beams and lower operating temperatures. The cathodes currently commercialized are dispenser cathodes, which integrate W matrix and Ba-containing impregnates[10]. During operation, Ba evaporates and forms a BaO monolayer on top of W matrix to lower the work function, which causes the intrinsic contamination and lifetime issues for these cathodes. Such issues are proposed to be overcome with intrinsic polar materials such as conductive perovskite oxides that have been predicted to have low work functions by density functional theory (DFT). However, there was a lack of experimental validation of the low work functions on these materials, making it questionable whether this proposed polar perovskite idea could work in real life. This dissertation solves this problem by experimentally exploring the thermionic emission of perovskite $SrVO_3$, which provides the first observation of low 2.3 to 2.7 eV work function on a bulk, monolithic, conductive, robust oxide material[11]. The surface chemistry and work function physics with patch field effect provide key guidance on the experimental demonstration of $SrVO_3$, suggesting its potential as an intrinsic polar oxide that is promising for thermionic emission applications.

Additionally, the thermionic emission behavior of another perovskite with low DFT predicted work function[12], $BaMoO_3$, has also been experimentally explored. The thermionic emission testing of this material indicates a complete cancellation of micron-sized-grain patch fields. However, the thermionic effective work function that is much higher than the DFT prediction suggests the existence of multi-scale patch field effects. Moreover, the complex emission behavior after high-temperature *in situ* annealing likely suggests the phase transformations related to Ba volatility with a similar manner of dispenser cathodes. Such highly speculative finding might suggest the potential of $BaMoO_3$

in cathode fabrication industry, but a significant amount of work is needed to gain more thorough understanding of this material and its emission.

This dissertation contains 5 chapters in total and is organized as follows. Chapter 1 provides a general introduction towards the background, motivation and main spirits of the other chapters. Chapter 2 covers a systematic summary of the deeper understanding on work function history, physics, measurement, calculation, current impact on a vast array of cutting-edge applications, and mechanism of work function engineering, which provides much fundamental science basis for the other chapters. Chapter 3 discusses the experimental realization of the low work function and promising thermionic emission behavior on perovskite $SrVO_3$. Chapter 4 introduces the interesting emission behavior, phase evolution and related physics and chemistry issues observed on $BaMoO_3$. Finally, Chapter 5 provides a summary with the potential impact of this dissertation, and points out some future research direction on work function and perovskite thermionic emission.

Chapter 2 – Deeper Understanding on Work Function

This chapter is based on the journal article I first authored: **L. Lin**, R. Jacobs, T. Ma, D. Chen, J. Booske, and D. Morgan, "Work function: Fundamentals, measurement, calculation, engineering, and applications", which is currently in the revision and resubmission process with *Physical Review Applied*[1]. During the exploration of low work function perovskite oxide for thermionic emission applications, I was facing much confusion related to work function that was seldomly clarified by previous researchers. This made me feel it was important and timely to provide a systematic review on work function physics, measurements, calculations, applications and engineering methods, in order to clarify the confusion with the following deeper understanding on work function.

2.1 History and current impact of work function

2.1.1 History of work function

The work function has been studied for over 100 years[2]. Research on this topic originated with an extensive investigation of the photoelectric effect. In 1882, when performing electromagnetic wave transmission experiments, Heinrich Hertz found that sparks formed more easily when light was incident on the experimental apparatus, indicating something was being emitted[13]. Soon afterward, in the late 1880s and 1890s, Wilhelm Hallwachs found that freshly cleaned zinc samples were more positively charged when exposed to ultraviolet light than in the dark, indicating that the emitted particles must have negative charge[14]. Around the same time, Alexandr Stoletov[15] discovered the emitted photocurrent was directly proportional to the light intensity, and J. J. Thomson

found that the emitted photocurrent radiation carried the same properties of the then-known "cathode rays", which were later understood to be emitted electrons[16].

In the early 1900s, more detailed experiments by Philipp Lenard led to significant, and, at the time, counterintuitive observations[17]. The key observed phenomenon by Lenard was that the photoelectric effect is mainly triggered with application of ultraviolet light, and that the maximum kinetic energy of emitted electrons is determined by the frequency of the incident light, rather than its intensity, indicating that a threshold frequency exists for electron photoemission to occur[17]. This observation of a threshold frequency, as opposed to a threshold intensity, was counter to the established understanding and predictions of James Maxwell's classical electrodynamics. A new understanding of the photoemission phenomenon was developed by Albert Einstein in 1905, when he applied Max Planck's quantum theory to the behavior of light, thus treating the incident light as individual particles (i.e. photons), and, to understand the meaning of a threshold frequency, introduced the concept of a surface energy barrier that is equal to the minimum work needs to be done on an electron in the solid to get it emitted, which is now referred to as the work function[18,19].

$$\Phi = W_{min} \qquad \text{Eq 2.1}$$

This new model of photoemission was experimentally confirmed by Robert Millikan in 1914[20], and both Einstein and Millikan won Nobel Prizes at least in part from their contributions to understanding the photoelectric effect.

Around the same time that Einstein developed the above new understanding of the photoelectric effect, Owen Willans Richardson investigated the phenomenon of thermionic

electron emission in detail, and subsequently derived an equation relating the measured thermionic emission current to the work function. At the time, the term “work function” was not established terminology, and Richardson himself referred to this energy barrier for thermionic emission as “the work done by a corpuscle in passing through the surface layer”. Richardson’s model of thermionic emission was temperature-dependent, and used a free electron gas model to represent electrons in the emitting material and a Maxwell-Boltzmann distribution for the electron velocity[2,21]. Richardson’s model was further modified by Dushman, Laue and others to include a Fermi-Dirac distribution of electron energies and electron spin, and is now widely known as the Richardson-Laue-Dushman (RLD) equation for thermionic emission[22–24].

In 1923, Schottky developed a modified model of thermionic emission to include the presence of electric fields, which can reduce the emission barrier[25]. In practice, Schottky’s original developments, which predict a linear dependence between the natural logarithm of the emission current density J and the square root of applied voltage V, often do not correctly describe the experimentally observed current-voltage relationship. However, the terms Schottky introduced to the thermionic model for electron emission are still critical to include when considering thermionic emission and work function measurement, and the field-induced work function-lowering observed experimentally is now widely known as the Schottky effect.

Shortly following the introduction of these new models of photoemission and thermionic emission, seminal studies were conducted on cold field electron emission by Lilienfeld, Millikan and Gossling[26–28]. Following the discovery of the linear dependence between $\ln J$ and $1/V$ by Lauritsen and Oppenheimer[29,30], the quantitative expression of

field emission was then derived by Fowler and Nordheim (F-N)[31]. The emission mechanisms and equations associated with the modes of electron emission discussed throughout this introduction will be discussed in more detail in Secs 2.2 and 2.3.

Despite this pioneering work, in the early 20th century the physical origin and nature of the work function remained unclear, primarily because the connections between quantum mechanics, solid state physics and electronic band theory were still being actively developed. In 1923, Schottky provided the first semi-quantitative model explaining the work function by thinking of the electrons leaving the metal surface as being attracted by a corresponding positive image charge present in the material[25]. As the development of quantum mechanics and electronic band theory matured, the relationship of the work function dependence with the Fermi level and surface dipoles was clarified, and a more precise definition of work function was therefore developed:

$$\Phi = E_{vac} - E_F \qquad \text{Eq 2.2}$$

With E_{vac} and E_F denoted to vacuum level and Fermi level, respectively.

These developments also resulted in the appreciation that a different work function value is associated with each specific material surface—e.g., surface orientation, such as the (001) vs. (011) crystallographic surface, or surface termination, such as a specific crystallographic surface that is cation or anion terminated—rather than a single work function value being representative of a particular material composition[7,32]. As the understanding of work function grew in the coming decades of the mid and late 20th century, researchers developed a greater understanding of the influence of surface and interface properties on work function, measured the work function with increasing accuracy,

calculated the work function with atomistic quantum mechanical methods like Density Functional Theory (DFT), and developed entire technologies predicated on designing materials with specific tailored work function values.

2.1.2 Current impact of the work function in various applications

Because of its nature of the surface energy barrier of electrons, work functions play a critical role in many technologies involving surfaces and interfaces. One direct applications field is electron emission into vacuum, where the emission current density depends exponentially on work function, technologies with such emission, such as photoelectric and vacuum electronic devices, fundamentally rely on understanding and manipulating the work function of materials. More broadly, since the work function represents the energy barrier for an electron moving through a particular surface, the work function is intimately related to myriad surface and interface properties through different types of energy level alignments, including band alignment and band bending, charge transport between materials, and charge transfer to and from chemical species during adsorption, desorption, and chemical reactions. Therefore, the work function is fundamental to many physical and chemical processes of a materials. It thus plays an important role throughout the technologies of solid-state electronics (e.g., diodes, field-effect transistors, and photonic devices) and electrochemical devices (e.g., solar cells, electrocatalysts, and battery electrodes), among others. It is therefore not an exaggeration to say that work function engineering is a key enabler of our modern technologies and lifestyle. Some of these applications have been illustrated in Fig 2.1.

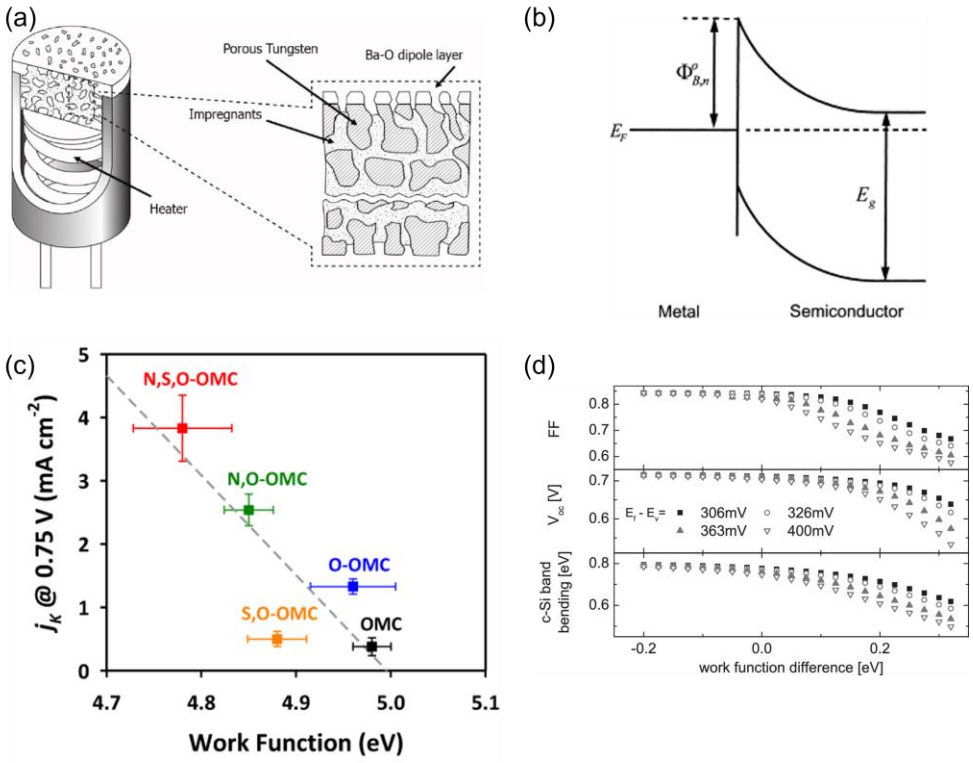

Fig 2.1. Some applications of work function engineering. (a) Schematic structure of dispenser B-type thermionic cathode (2018 IEEE. Reprinted with from Ref. 3), showing the surface BaO dipole layer that decreases the work function. (b) Schematic band diagram of a metal-insulator barrier, showing the work function related Schottky barrier at the interface (Reprinted from Ref. 4, Copyright 2001, with permission from Elsevier). (c) ORR reaction current density as a function of catalyst's work function (Reprinted with permission from Ref. 80. Copyright 2014 American Chemical Society). (d) DFT-Simulated solar cell parameters as a function of the work function difference between the TCO electrode and the (p)a-Si:H layer for different distances of the Fermi-level from the valence band (Reprinted from Ref. 100, with the permission of AIP Publishing).

2.1.2.1 Electron emission

Electron emission is the process of electrons originally in a material moving into the vacuum through its surface. This case could be thought of as the energy level alignment of an electron inside the solid towards its adjacent vacuum, where the work function is directly the energy barrier for such electron migration that governs the emission behavior.

Depending on the type of energy sources for activating the emitted electrons, electron emission could be categorized as several types, including thermionic emission where electrons are activated by thermal energy, field emission where electrons are tunnelling through the surface energy barrier under high electric field, photoemission where electrons are kicked off by incident photons, and mixtures of these flavors including Schottky emission (a mixture of thermionic and field emission mechanisms) and graphene-based hot electron photoemitters[33] (combining thermionic and photo- and possible field emission mechanisms). In all of these types, the work function of the emitting surface plays a central role in determining the emission ability.

Specifically, in the case of thermionic emission, the emission current density (within the temperature-limited regime) is governed by RLD equation[34]:

$$J_T = AT^2 \exp\left(-\frac{\Phi}{kT}\right) \qquad \text{Eq 2.3}$$

where A is called Richardson constant that is related to the emitting surface properties (which will be further discussed in Sec. 2.3.3).

In field emission, the emission current density is governed by F-N equation[34]:

$$J_F = \frac{A}{k_B^2 c_f^2} \exp\left(-\frac{b_f}{F}\right) \qquad \text{Eq 2.4.1}$$

with

$$b_f = \frac{4}{3\hbar}\sqrt{2m\Phi^3}v\left(\frac{\sqrt{e^2F/4\pi\varepsilon_0}}{\Phi}\right) \qquad \text{Eq 2.4.2}$$

$$c_f = \frac{2}{\hbar F}\sqrt{2m\Phi}t\left(\frac{\sqrt{e^2F/4\pi\varepsilon_0}}{\Phi}\right) \quad \text{Eq 2.4.3}$$

where the functions $v(y)$ and $t(y)$ above can be approximated by

$$v(y) \approx 0.936814 - y^2 \quad \text{Eq 2.4.4}$$

$$t(y) \approx 1 + 0.06489y + 0.0458308y^2 \quad \text{Eq 2.4.5}$$

At high field, J_F is approximately proportional to $\exp\left(-\Phi^{3/2}\right)$

For photoemission, the quantum efficiency (QE)[34], which is the ability to liberate electrons for a given incident light intensity with its photon energy larger than the surface work function Φ, is negatively related to Φ:

$$QE \propto (\mathrm{h}\upsilon - \Phi)^2 \quad \text{Eq 2.5}$$

Among all of these emission mechanisms, one common point is that a small reduction in the work function of the emitting surface generally leads to a dramatic boost of emission current density. Developing lower work function emitters is therefore becoming a central research and engineering interest for technologies relying on electron emission, such as photomultipliers and photocathodes based on photoemission, vacuum nanoelectronics using field emission, and devices such as travelling wave tubes, klystrons, and renewable energy thermionic converters which use thermionic emission.

Many different types of cathodes have been developed based on these mechanisms. For photocathodes used for generating electron beams in radiofrequency applications such as linear accelerators, free electron lasers, and related devices[35], people are pursuing improved device performance with low work function coating materials, e.g., alkali metal,

such as Cs, coated on GaAs or GaN photoemitters, which could lead to a work function reduction of 2-3 eV compared to the uncoated material[36–39]. For field emitters used as cold cathodes in vacuum electron tubes, electron beam lithography, and electron microscopes, one common method is geometric and morphological modifying the emitters into "sharp-tip" shapes or arrays to enhance the local electric field, e.g., sharp-tip tungsten cold cathodes, Spindt arrayed emitters as well as carbon nanotubes.[35,40] In addition, the field emission current densities can be further enhanced by applying a low work function material or coating. Zhang et al. [41] and Nakamoto et al.[42] have fabricated field emitters with low work function LaB_6 (2.7 eV, compared to Mo or W based field emitter with a ~5 eV work function). Nakamoto et al.[43] have also employed TiN (3.2 eV work function) coating on Ni field emitter array to pursue higher emission.

Recently, there has been significant research on negative electron affinity (NEA) semiconductors derived from diamond and nitrides[44–46], because of the proposed spontaneous electron emission as the conduction band minimums (CBMs) of them are above the vacuum level (see detailed discussion on work function physics in Sec. 2.2). These materials have been investigated for applications in photo and field emitters by proper energy level pinning to facilitate emission[44,47,48]. Such NEA materials include wide-band-gap nitride and diamond with adsorbed H. Recently, to overcome the electrically insulating issue of the canonical NEA materials, researchers have developed graphene-based heterostructures allowing hot electrons tunneling into graphene layer to effectively emit from NEA states[33,49,50]. The recent progress on NEA materials opens the door to experimenting with various surface, interfacial, and band alignment engineering[45,48–50].

For thermionic emitters widely used as electron sources of electron microscopy, electron beam lithography, and high-frequency vacuum electronic devices, the main research efforts have been devoted to lowering the cathode work function and improving the operational stability and longevity. Besides some early works on less-stable oxide cathodes[51–53], the mostly studied and commercialized materials are hexaborides[54–56] and dispenser cathodes[3,10,57]. Hexaborides have moderately low work functions of ~2.5 eV created by an intrinsically polar surface. Dispenser cathodes, on the other hand, are able to achieve ~2 eV effective work functions (see Sec. 2.3.3) owing to the vaporization of the Ba-containing impregnates and the adsorption of Ba-O monolayer species that creates a large surface dipole. In the past two decades, a subgroup of dispenser cathodes containing Sc_2O_3 nanoparticles in the W matrix or the impregnate, commonly known as scandate cathodes, has drawn great attention, due to their lower effective work function (about 1.5 eV) and higher beam brightness[3,58,59]. However, dispenser cathodes generally suffer from lifetime and contamination issues due to the volatile nature of the Ba-containing impregnate species[3,60–64], and scandate cathodes also specifically have emission uniformity, performance and manufacturing reliability, and unclear emission mechanism issues[58,59,65,66]. Recently, it has been proposed to use stable oxides with polar surfaces to obtain low work function emitters[12,67], and some perovskite candidates have been experimentally studied by me to show their potential for next-generation emitter applications, which will be further discussed in Chapters 3 and 4 in this dissertation.

2.1.2.2 Solid state electronic interfaces

The work function is a crucial property to understand the electrical properties of material interfaces in solid state electronics[68]. When two different materials are brought

into contact, thermodynamic equilibrium will align the Fermi levels of the two materials, as Fermi level is the chemical potential of electrons in the material. Thus, if the two materials have different work functions, electrons will flow from the lower work function material to the higher one, leading to several effects at the interface.

Taking a metal-semiconductor interface as an example, the electron flow will cause each material to become slightly biased, where excess charge would primarily accumulate on the semiconductor side near the interface because of its relatively lower (compared to the metal) electrical conductivity, causing the formation of a space charge region and band bending[68]. Meanwhile, this charge flow will form an energy barrier at the interface due to the contact potential difference (CPD, see Sec 2.2 and 2.3.2). For the contact of a metal and an n-type semiconductor, as shown in Fig 2.1(b), if the work function of the metal is larger than the work function of the semiconductor, the metal-semiconductor junction will be rectifying, and there will be a sharp energy barrier on the interface, known as a Schottky barrier. In the idealized case its height, Φ_{bn}, is determined by the metal work function Φ_M and the semiconductor electron affinity χ, according to the Schottky-Mott rule:

$$\Phi_{bn} = \Phi_M - \chi \qquad \text{Eq 2.6}$$

On the other hand, if the metal work function is smaller than the (n-type) semiconductor work function, the interface region will be non-rectifying, leading to the formation of an Ohmic contact.

The above Schottky-Mott rule (Eq 2.6) and associated rectifying and Ohmic junction models are the simplest, ideal cases. In reality, defects and imperfect bonding at the interface (e.g., dangling bonds) lead to charged interface states which can pin the Fermi

level and cause the true Schottky barrier height to deviate from the ideal case, making the barrier height calculation significantly more complicated. Several theoretical treatments have been developed to deal with the deviation of the Schottky barrier height from the theoretical prediction of Eq 2.6. For example, Freeoff and Woodall have developed an effective work function model, which substitutes the metal work function in Eq. 2.6 with a properly selected, weighted average work function of different interface phases. Schmitz, et al. studied the Schottky barrier between n-type GaN and various metals, suggesting that the barrier height indeed increases monotonically with increasing metal work functions, although the value does not scale proportionally. These studies suggest that despite the additional complexity induced by sometimes sophisticated interfacial chemistry, the relative work functions of the metal and the semiconductor are still relevant to the rectifying nature and the Schottky barrier height[69,70].

The correlation between the work function and the interfacial barrier height directly relates to device properties such as charge transport across the interface. Specifically, despite the possible complex interfacial physics (which may cause very weak dependence between work functions and barrier height), tuning the work functions of both sides of the interface is still an important approach to achieve optimum barrier height or high-quality Ohmic contact. For example, Tongay et al. have used Br intercalation to tune the work function of multilayer graphene in connection with semiconductors, and consequently modified the barrier height and device performance of the Schottky diodes. Tang et al. have reported a uniform method for solution-processed doped films that are able to reach ultrahigh or ultralow work functions, which is essential for good Ohmic contact in device engineering[4,68,71–75].

For more complex electronic devices, the work function also plays a significant role. One example is metal-insulator-semiconductor (MIS) structure, where the work function mismatch between the metal and semiconductor will cause built-in electric field and band bending, and a flat band voltage is needed to correct such bending. For metal-oxide-semiconductor field effect transistor (MOSFET) devices, the threshold voltage and drain-to-source on-current is directly associated with the work function difference between the gate and channel materials, so materials need to be chosen in part based on their work function value and the work function actively engineered for optimal device design[76–78].

Overall, for solid state electronic devices, engineering the work functions of various materials comprising the heterostructures of a device is particularly critical for reaching desirable electrical connection and controlling device performance by tuning barrier heights. To sum up, the work function strongly influences the relative energy level alignment across interfaces in solid state electronic devices, therefore is one of the key properties to understand and to tune for achieving better device performance.

2.1.2.3 (Electro)catalysis

(Prof Dane Morgan significantly contributed to this section.)

Many chemical reactions are accelerated by a solid catalyst that binds species relevant to the overall chemical reaction. Such binding often involves electron transfer between the catalysts and the adsorbed reactants, typically between the Fermi level of the catalyst and the highest occupied molecular orbitals (HOMOs) or lowest unoccupied molecular orbitals (LUMOs) of the reactants. Therefore, the catalytic behavior can strongly correlate with the relative alignment between the reactant orbital levels and catalyst Fermi

level, and therefore with the work function of the catalyst. However, the relationship between work function and catalyst-reactant charge transfer is not straightforward.

First, consider a simple case that a reactant or product species is adsorbed on the catalyst surface with one electron transfer during the process (e.g., F on Cu). Assuming the catalyst has a simple homogeneous surface with unchanged dipole, the adsorbate has a fixed energy level to take the electron, and there are no external fields (as these will affect the interpretation of work function, see Sec 2.2), the electron migration could be thought of as a combination of two steps, i.e., the electron moving between the vacuum level and catalyst Fermi level and it moving between the vacuum level and reactant corresponding molecular orbital. Therefore, the energy to transfer the electron is simply the difference between the catalyst work function and the LUMO or HOMO of the reactant. This simple analysis suggests that for a given reactant, binding energies associated with significant charge transfer should have a strong correlation with the catalyst work function. Such correlation may not be exact since many factors may change between two catalysts (e.g., different surface dipoles from the adsorbate, different modifications of the adsorbate molecular orbitals, etc.), but it is likely to occur unless the catalysts have significantly different fundamental electronic properties (e.g., difference between oxide and metal catalysts). Since absorbate energies largely control the catalytic rates, the work functions and catalytic rates are likely to show strong correlation within a class of similar materials (e.g., simple metals).

On the other hand, when considering an electrocatalyst and an associated redox reaction which involves charge exchange across the catalyst electrode and electrolyte interface, catalyst work function also plays an important role. However, comparing to a

non-electrochemical reaction, the adsorbate in an electrochemical cell arrives at the electrode with a positive charge and an electron is transferred to the adsorbate on the catalyst surface, e.g., an H^+ is reduced to H on the electrode of catalyst. Another two-step treatment is employed in this discussion, where: (i) the charged adsorbate moves to the surface of the catalyst, and (ii) an electron is moved from the material to the adsorbate. The first step involves a number of complex energy terms associated with moving charge through the dipole fields near and at the surface, which consist of contributions from electrode/electrolyte interface, electrochemical double layer, and the diffuse layer. These important contributions are strongly influenced by the applied potential and actually less relevant to the electrode work function. The second step is analogous to the adsorbate binding in the (non-electro)chemical reaction described above and its energetics are expected to be strongly dependent on work function for the same reasons. The energies of both steps together will depend on the applied potential and work function, as well many other factors (e.g., geometry of surface binding sites) which could be assumed similar for same adsorbates and similar other conditions. Additionally, since the energy of the two steps must add up to zero to stabilize the reduced intermediate to drive the reaction, it is expected that the potential needed to drive the reaction will be a function of the catalyst work function, or equivalently, that the overpotential of an electrochemical reaction will depend on work function with a similar manner as the (non-electro)chemical reactions.

Since the relative energy level alignment decides the charge flow direction between the catalyst and the reactant, it is expected that the relationship between the reaction rate and work function of the catalyst will depend on reaction types. As discussed by Vayenas et al. when studying non-Faradaic electrochemical modification of catalytic activity[5,79],

the catalytic reaction rate r exponentially depends on the catalyst work function Φ through:

$$\ln\frac{r}{r_0} = \alpha\frac{\Phi - \Phi^*}{kT}, \qquad \text{Eq 2.7}$$

where α and Φ^* are reaction- and material-specific constants. α is positive for an "electrophobic" (oxidation) reaction (i.e., the catalyst takes electrons from the reactant), where a higher work function catalyst serves as the electron sink and tends to aid in stabilizing the oxidation reaction products. For an "electrophilic" reduction reaction (where the catalyst gives electrons to the reactant), a negative α means that a lower work function catalyst serves as an electron source which may aid in stabilizing reduction reaction products. This is proposed as a general trend that applies to catalysts for any reactions where rate controlling intermediates are gaining (reducing) or losing (oxidizing) electrons to the catalyst, even if the reaction is not electrochemical in nature, because of the same work function dependence mechanism for both non-electrochemical and electrochemical catalytic reactions described above. This correlation between the rate trending positively (negatively) with work function for oxidative (reductive) catalyst behavior simply follows from the fact that higher work functions make it harder (easier) to oxidize (reduce) the catalyst, assuming all other factors being equal.

The trend discussed above has been proved by numerous computational and experimental efforts. Generally, a negative dependence between the catalyst work function and catalytic reaction rate has been frequently observed for many "electrophilic" reactions. For example, Cheon et al. found a linear decrease in electrochemical oxygen reduction reaction (ORR) current density as the work function of a doped nanocarbon catalyst

increases.[80]. Stoerzinger et al. and Hong et al. have studied $LaMnO_3$-type perovskites, and showed that the work function correlates to the ORR rates by indicating the interfacial band bending related to electron transfer during such reactions[81,82]. The work from Trasati[83], Calle-Vallejo et al.[84], and Losiewicz et al.[85] on hydrogen evolution reaction (HER) all show that the HER exchange current increases exponentially as electrode work function decreases, where the negative correlation is consistent with the reaction being fundamentally reductive. On the other hand, abundant examples also indicate the opposite trend for "electrophobic" oxidation reactions. Kumar et al. showed that the methane oxidation activation energy decreases linearly (i.e., reaction rate increases exponentially) with the increase of a series of catalyst work functions[86], consistent with the reaction being oxidative. Vayenas et al. reported the non-Faradaic electrochemical modification of catalytic activity in oxidation reactions with β"-Al_2O_3 is exponentially increasing with the catalyst average work function.

The trend predicted by Eq 2.7 is also proved to be true in oxygen evolution reaction (OER) reactions, where Grimaud et al. first demonstrated current density of perovskite catalysts positively correlates with the oxygen *p*-band, with many studies revealed a positive correlation between the oxygen surface coefficient k^* and oxygen *p*-band [87–90], which in turn correlates positively with work function[12,67]. For all the studied systems deriving these positive correlations, the mediating species for the oxygen exchange process that sets k^* are oxygen vacancies that reduce the catalysts (i.e., "electrophobic" reactions). On the other hand, Lee, et al. [91] showed that for a set of interstitial oxygen transport materials k^* was negatively correlated with work function, where the oxygen exchange process that sets k^* are oxygen interstitials that oxidize the catalyst when they are formed

(i.e., “electrophilic” reaction). Therefore, all the above correlations between catalyst or electrode work functions and OER reaction characteristics are consistent with the qualitative and in some cases even quantitative implications of Eq 2.7.

In general, a significant correlation is expected between work function and the energetics of any process involving exchange of electrons at the material surface, such as surface adsorption, charge transfer, and redox. Thus, it is possible to tune catalytic properties of specific electrochemical reactions by tuning the work function of the catalyst surface[92,93]. These results, and many others, suggests work function engineering is a critical tool when designing high-performing catalysts.

2.1.2.4 Other applications involving work function engineering

By providing a benchmark for energy level alignment, work function serves as a useful guide for a number of related applications. Tuning work function therefore generally turns into tuning relative energy level alignment, which is a powerful way to achieve better performance in these applications.

Work function has been involved as a key factor in many energy harvesting applications, i.e., transforming other forms of energy to electricity. Thermal energy can be harvested directly from thermionic emission through so-called thermionic converters, in which alkaline metal adsorption from the vapor is the primary approach to lower the cathode work function[94,95]. In solar photovoltaics used to harvest photon energy, similar to solid state electronics, work function serves as an important factor for controlling charge transfer. For example, as pointed out by Qi and Wang[96], when the electrode-active layer contact in the organic solar cell is non-Ohmic, the open-circuit voltage will largely depend on the work function difference of the electrodes. It has also been suggested that the built-

in electric field, open-circuit voltage and efficiency of Si-based and organic photovoltaic cells strongly correlates with work functions of the transparent conductive oxide (TCO), and a higher work function is generally preferred[97–100]. Recently, tuning the band alignment (thus work function) of the electron and hole transport layer materials has been one of the key factors contributing to the recent boost of the halide perovskite (e.g., using methylammonium lead iodide ($MAPbI_3$)) solar cell efficiency to nearly 25%[101–103]. Additionally, Varpula et al. reported an approach to harvest mechanical energy from two electrodes with different work functions by vibrating one electrode relative to the other[104]. Because the work function difference between electrodes introduces a built-in electric field, such electrode motion will do work in the field, transforming kinetic energy of the electrode to electrostatic energy.

In a photocatalytic water splitting reaction, the water molecules decompose into H^+ ions and O_2 after absorbing photons and holes, and H^+ ions combine with electrons to form H_2. Thus, a key process is separating electrons and holes before recombination, in which case proper band alignment plays a significant role. Beasley et al. have studied a series of metals in the metal-TiO_2 heterostructure for photocatalytic water splitting and discovered a linear increase of hydrogen production with the increase of metal work function in the heterostructure[105]. This is because a higher metal work function makes it energetically more difficult for electrons to transfer back to TiO_2 to initiate electron-hole recombination, resulting in a higher hydrogen yield. Similarly, for water splitting photoelectrochemical cells, Ye et al. have also tuned the C_3N_4 electrode work function by boron doping to enhance the charge separation[106]. Meanwhile, they have also managed to reduce the interfacial energy loss and increase the open-circuit voltage of $BiVO_4$

photoelectrochemical cells by tuning the work function via Mo doping, which is also beneficial for water splitting.

Band alignment is also involved in many studies of solid-state batteries. Recently, Gao et al. [107] have studied the gassing issue of the spinel $Li_4Ti_5O_{12}$ anode of the lithium-ion battery, pointing out that the Li-rich surface and oxygen vacancies lower the anode work function, which translates into an increasing chemical potential that greatly promotes the interfacial reaction of electrolyte decomposition. Warburton et al. have investigated the interfacial thermochemistry and band alignment of a solid-state Li-ion battery with lithium lanthanum titanate electrolyte (LLTO) using DFT calculations[108]. The study points out the TiO_2-terminated surface is more likely to be involved in redox reactions because the conduction band minimum of LLTO is lower than the Fermi level of metallic Li anode, when aligning the vacuum level together, which makes electron transfer to LLTO more favorable, leading to the decomposition of the electrolyte by reducing Ti^{4+} cations to more reducing states. This could explain the tendency for decomposition of TiO_2 terminated LLTO. Such band alignment also shows the difficulty of charge transfer in the presence of a La_2O_3 buffer layer, suggesting its potential application as an interface coating material.

There are also numerous examples related to other application aspects. For example, Li et al. have investigated using TiO_2-SnO_2 core-shell heterostructure nanofibers for gas sensing[109]. In such a heterostructure, TiO_2 has a lower work function (4.2 eV) compared to SnO_2 (4.9 eV), meaning that extra electrons will flow from TiO_2 to SnO_2, significantly increasing the detection response towards acetone and ammonium.

2.2 Physics of work function and its engineering

Despite the seemingly simple physics picture of surface barrier (Eqs 2.1 and 2.2) and wide applications, the concept and interpretations of work function remain much confusion. Because of the importance of work function in numerous applications discussed in the previous section, clarifying such confusion is crucial for both fundamental science understanding and cutting-edge applications.

2.2.1 Work function definition, under influence of electric field and surface heterogeneity

As discussed in Sec 2.1, the work function is generally described as *the minimum energy required (or minimum work required) to remove an electron from the material to vacuum*. With the development of quantum mechanics and solid state physics, the most common definition is provided in Eq 2.2, which is the energy difference between the vacuum level E_{vac} and Fermi level E_F for a metallic solid (the case of semiconductor will be briefly discussed in Sec 2.2.1.4). However, this definition remains ambiguous, mainly due to the unclear interpretation of the term *vacuum level*, which is rigorously defined as the rest energy of a free stationary electron in vacuum outside any materials. This definition implies that E_{vac} is essentially equal to electrostatic potential energy, therefore actually a function of location ($E_{vac}(\boldsymbol{d})$), influenced by the widely existing electric field within the vacuum. Therefore, from Eq 2.2 it could be seen that different selections of position $\boldsymbol{d}$ could lead to different values of $E_{vac}(\boldsymbol{d})$, resulting in different values of "work function" if directly using Eq 2.2. Given this, it is important to clarify the definition of work function under vacuum level profiles in different conditions. In the following Secs 2.2.1.1 through 2.2.1.3, a series of electrostatic potential energy profiles as a function of distance to the

surfaces will be provided, to clarify the work function and related quantities under several different electric field and surface heterogeneity conditions. In these simple but representative cases, the position vector $\boldsymbol{d}$ could be simplified as the distance of a point towards the surface, d. Meanwhile, the Fermi level E_F could be treated as an unchanged reference energy level, the vacuum level behavior will therefore be directly connected to work function behavior (although such connection is not simply Eq 2.2 in many cases).

2.2.1.1 Homogeneous surface, with zero electric field

The first, simplest case is a metal surface with one single work function and zero external electric field above the surface. As shown in Fig 2.2, when an electron moves out of the surface, the potential energy of the electron is initially quite complex due to still being coupled to the electronic structure of the material, but the electron then becomes a free electron after moving a few Angstroms from the surface, with the image charge potential energy $E_{img}(d)$ a good approximation for its $E_{vac}(d)$:

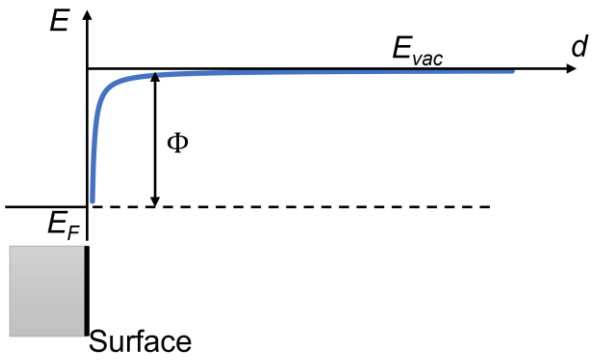

Fig 2.2. The electron energy diagram above a surface with Fermi level, vacuum level, and the definition of local work function for a homogeneous surface without external electric field. In this case, the vacuum level is flat after the image charge potential stabilizes when the distance to the surface increases.

$$E_{vac}(d) = E_{img}(d) = -\frac{e^2}{16\pi\varepsilon_0 d} \quad \text{Eq 2.8}$$

This image charge potential energy rapidly increases within the first 1 to 2 nm, and then becomes approximately constant beyond a distance of a few nanometers from the surface. Strictly speaking, the image charge interaction extends rigorously to infinity, but the energy difference between $E_{img}(5\text{ nm})$ and $E_{img}(\infty)$ is only 0.072 eV, which is negligible for most purposes; therefore, $E_{img}(d)$ could be treated as a constant energy when $d \gtrsim 5$ nm. As shown in Fig 2.2, since there is no external electric field to further influence 0this electrostatic potential, this constant energy level will extend to infinity, providing a uniquely defined work function Φ directly through Eq 2.2.

2.2.1.2 Homogeneous surface, with external electric field; the observed work function

The next case is a homogeneous metal surface with an external electric field presents in the vacuum besides that due to the image charge. Such field may be applied intentionally to pull off electrons, e.g., the field applied between the cathode and anode in electron emission, or sometimes created inadvertently, e.g., the fields that occur in vacuum experiments due to local work function difference between an electrically connected sample and a vacuum chamber (also known as Volta potential). In the presence of an external electric field, the vacuum level $E_{vac}(d)$ usually do not converge to a constant at infinity (cf. Fig 2.3), and the simple definition of work function discussed in Sec 2.2.1.1 needs to be carefully revisited[110].

In this situation, it is generally desirable to give a definition of work function with the vacuum level that is far away enough from the surface that the image charge potential has (nearly) converged, but the influence of the potential induced by the external field is

still too small to significantly alter the potential energy of the emitted electron. This condition is typically fulfilled within a distance of 5 nm $\lesssim d \lesssim$ 10 nm when the external electric field is weak (e.g., no larger than several 10^6 V/m, then the potential energy modification by this field within the first 10 nm from the surface is several times 0.01 eV, again negligible for most purposes). Therefore, since this 5 to 10 nm distance provides a vacuum energy level that is intrinsic for a specific surface of a material without depending on external electric field conditions, the work function defined with this vacuum level is the mostly employed definition within surface science research. Meanwhile, the selection of vacuum level, which is at a small distance of 5 to 10 nm towards the surface, also gives this work function definition a fundamentally *local* nature. Thus, the point corresponding to a distance of 5 nm $\lesssim d \lesssim$ 10 nm is called *local point* d_l, and it is accurate and proper to call the work function definition corresponding to the *local vacuum level* $E_{vac}(d_l)$ the l*ocal work function* Φ_l:

$$\Phi_l = E_{vac}(d_l) - E_F \qquad \text{Eq 2.9}$$

Since Φ_l is independent to external electric field, it has approximately the same value with the zero-field work function Φ discussed in Sec 2.2.1.1. However, to make this argument valid, it is necessary that the external field is not strong enough to significantly alter the image charge potential within the first few nanometers from the surface. The strong field (especially the strong negative) case will be further discussed in this section.

Eq 2.9 provides a unique definition of work function as an intrinsic material surface property. However, practically it is often more convenient or even necessary to effectively measure the energy of the electron much farther from the surface than the local point,

instead of directly measuring the local work function with the local vacuum level. When measuring the electron energy at an observation point O with a position vector $\boldsymbol{d_O}$, the non-flat vacuum level profile may make the quantity $E_{vac}(\boldsymbol{d_O}) - E_F$ no longer equal to the local work function, or even not reflect the nature of electron energy barrier (see Fig 2.3).

To clarify this issue in work function measurement and interpretation, a quantity named *observed work function at a point O*, $\Phi_O(\boldsymbol{d_O})$, is introduced, which is equal to the minimum electrostatic potential energy barrier an electron needs to overcome to reach the point O. As discussed above, in these simple discussions only a one-dimensional vacuum level profile is considered, and the vacuum level and observed work function could be written as a function of d_O, i.e., $E_{vac}(d_O)$ and $\Phi_O(d_O)$. Under such one-dimension simplification, the potential energy barrier for $\Phi_O(d_O)$ definition corresponds to the maximum $E_{vac}(d)$ in the range of $0 < d \leq d_O$.

$$\begin{aligned}\Phi_O(\boldsymbol{d_O}) &\equiv \min_{\text{From surface to O}}(\text{Barrier height}) - E_F \\ &= \max_{0<d\leq d_O}\left(E_{vac}(d)\right) - E_F \end{aligned} \qquad \text{Eq 2.10}$$

The co-existing minimum and maximum in Eq 2.10 seems contradictory, but it correctly reflects the energetics of electron migration. *Minimum* refers to the directions parallel to the surface, indicating the smallest barrier for an electron to overcome along all the possible paths to reach O, whereas *maximum* refers to the energy profile perpendicular to the surface, reflecting the nature of an energy barrier which is the maximum potential energy along each path. In more complex cases (e.g., a heterogeneous surface discussed in Sec 2.2.1.3), the point corresponding to this energy barrier is actually the *saddle point* of

the multi-dimensional potential energy landscape, i.e., minimum along the directions parallel to the surface but maximum along the perpendicular direction.

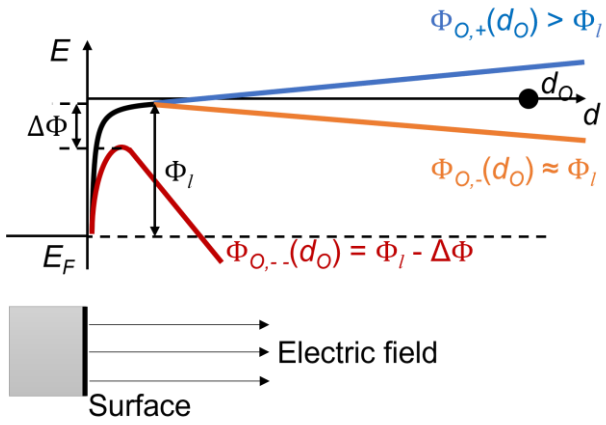

Fig 2.3. The electron energy diagram above a surface with Fermi level, vacuum level, and the definition of local work function for a homogeneous surface with an external electric field. The three curves correspond to an applied field that is normal to the surface and positive (pointing away from the surface, subscript "+", blue), weak negative (pointing towards the surface, subscript "-", orange), and strong negative (subscript "- -", red).

Fig 2.3 helps illustrate the potential barrier maximum described in Eq 2.10 and the relationship between the observed work function $\Phi_O(d_O)$ at a remote observation point O (typically more than millimeters away from the surface) and the surface (local) work function Φ_l under different electric field conditions. In the discussion here, the electric field pointing out from the surface, i.e., preventing the electrons from leaving the surface, has been assigned as the positive field. The field conditions and corresponding $\Phi_O(d_O)$ are summarized below:

(1) When the external field is positive, the field will create an additional barrier to prevent the electrons from further leaving the surface. This makes $\max_{0<d\leq d_O}\left(E_{vac}(d)\right) = E_{vac}(d_O) > E_{vac}(d_l)$, and $\Phi_O(d_O) > \Phi_l$.

(2) When the external field is negative but not too strong (no larger than several 10^6 V/m), the field will lower the electrostatic potential energy of an electron when it leaves farther away from the surface, and $\max_{0<d\leq d_O}\left(E_{vac}(d)\right)$ will occur at the local point where the influence of the surface image charge stops being felt. In this case, $\max_{0<d\leq d_O}\left(E_{vac}(d)\right) \approx E_{vac}(d_l)$, meaning that $\Phi_O(d_O) \approx \Phi_l$. Note that this will not hold if the applied field is comparable to the image charge field at a few nm away from the surface (~10^8 V/m, see appendix for calculation details), since this will change the values of $E_{vac}(d_l)$, see case (3) below.

(3) If the negative field has a strength comparable to the image charge potential at the near-surface region (greater than 10^8 V/m), the potential curve and its maximum will be significantly bent to lower energy, leading to a decrease of $\Phi_O(d_O)$ by the amount of:

$$\Delta\Phi = \sqrt{\frac{e^3 F}{4\pi\varepsilon_0}} \qquad \text{Eq 2.11}$$

where e is elemental charge and F is the electric field. This reduction is called Schottky effect, as it is associated with a model Schottky[25,111] applied in 1923 that failed to quantitatively explain field emission, but it is still a very important factor in electron emission. This effect will be further discussed in Sec. 2.3.3. In this strong field limit, it is common to refer to the observed work function $\Phi_O(d_O)$ defined in Eq 2.10 (with a decrease of $\Delta\Phi$ following Eq 2.11) as a work function, which is reasonable as it is still the minimum energy to remove an electron from the material, and this potential barrier still corresponds to the local point ($\Phi_O(d_O)$=$E_{vac}\left(d_l(\text{strong field})\right) - E_F$). However, $\Phi_O(d_O)$ with a

strong field is no longer equal to the weak field Φ_l nor any intrinsic materials property, but instead a function of the applied field.

2.2.1.3 Heterogeneous surface, without and with negative applied electric field; the patch field effect.

The discussion above focused on the case of a homogeneous surface with one single local work function over the entire surface. However, in many materials, obtaining a homogeneous work function surface is extremely difficult because of the difficulty in producing and maintaining a large homogeneous single-crystal surface with only one orientation and termination. Most materials will consist of multiple grains with different surface orientations and terminations, and thus contain different local work functions. Some may also have heterogeneous surface dipole coatings that modify the local work function in a patchy manner. The presence of multiple different local work functions on a material surface will introduce further complexity into the vacuum level profile and the work function interpretation through the patch field effect, as described below.

Fig 2.4(a) shows the electric field above a surface containing two surface components with different local work function values Φ_L and Φ_H ($\Phi_L < \Phi_H$), resulting from, for example, partial coverage by a surface dipole layer, a situation discussed below. It is assumed patches are large enough that each can have a well-defined local work function following the definition given in Secs 2.2.1.1 and 2.2.1.2, and there are no applied fields. Since the two regions are in electrical contact and in equilibrium, the Fermi levels of the two regions are equal, and the difference in local work functions translates to a difference in the local vacuum levels, which equates to an electrostatic potential energy difference between points just above the two surface patches. Such lateral electrostatic

potential energy difference will naturally create a non-zero electric field above the surface to modify the electrostatic potential energy even if the externally applied field is zero. This modification of the electrostatic energies by electric fields induced by heterogeneous local work functions is often called the patch field effect, first discussed in the 1930s[7].

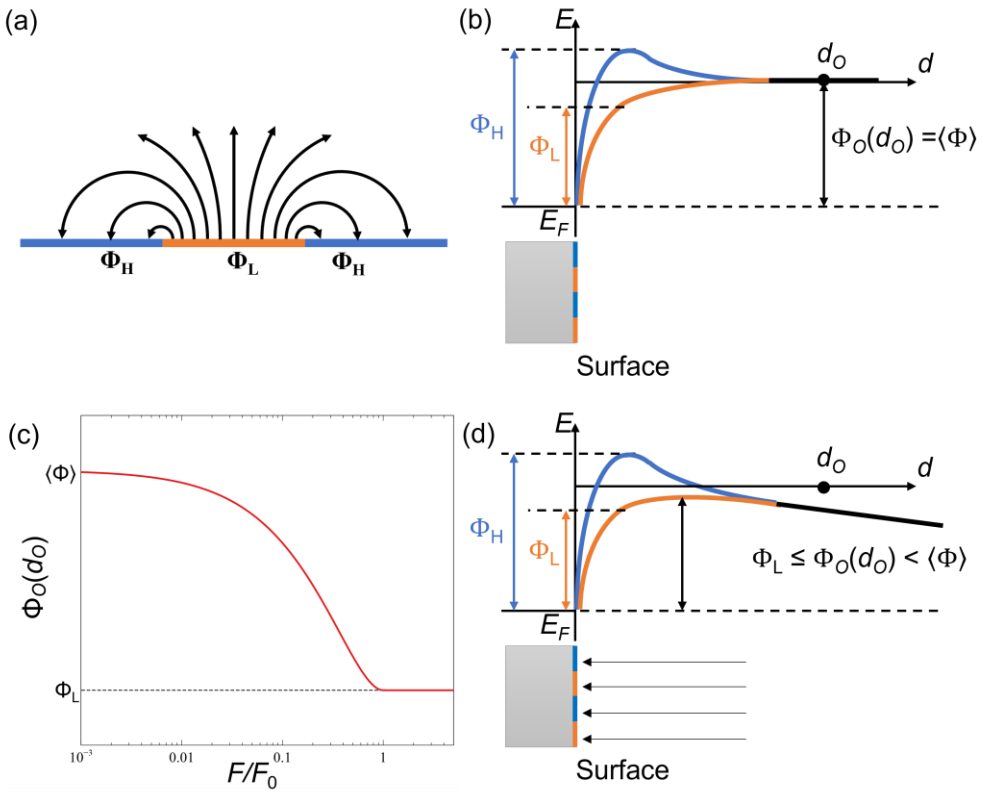

Fig 2.4. (a) Schematic of the patch electric field distribution (in absence of an external field) above a lower local work function (Φ_L) patch bordered by higher local work function (Φ_H) areas. The induced lateral surface dipole field draws electrons emitted from the Φ_L patch back towards the surface. (b) The energy diagram without an applied field above a patchy surface, with the observed work function at point O, $\Phi_O(d_O)$, equal to the average work function on the surface. (c) Observed work function versus applied electric field plot derived from Eq. 5.1, showing $\Phi_O(d_O)$ decreases as external field increases, until Φ_L when the field reaches F_0. (d) The energy diagram with a negative external field above a patchy surface, suggesting $\Phi_O(d_O)$ becomes lower.

Figs 2.4(a) and 2.4(b) illustrate how the surface patch electric fields transform the local electrostatic energy with this simple two-component scenario. The electrostatic

potential energy of an electron above each patch and far away from patch edges will look similar to that of a homogeneous surface. As the electron moves farther away from the surface, the difference in electrostatic potential energy decreases until the electrostatic energy above both patches merges into a single value, because the local field effects must diminish at infinity. This single value is the area-weighted average value of the two local work functions across the surface: $\langle\Phi\rangle = \eta\Phi_{\mathrm{L}} + (1-\eta)\Phi_{\mathrm{H}}$, where η is the coverage fraction of Φ_{L}. Therefore, moving away from the surface, the electrostatic potential energies (vacuum levels) above the Φ_{L} and Φ_{H} patches will increase and decrease, respectively, until converging to $\langle\Phi\rangle$ at infinity. The observed work function at a remote point O will also be equal to this average work function: $\Phi_O(d_O) = \langle\Phi\rangle$.

If there is a negative external electric field, the electrostatic potential energy component induced by this field decreases with distance from the surface. This term will generally lower the barrier energy, reducing the observed work function $\Phi_O(d_O)$ from $\langle\Phi\rangle$ towards a lower value (as shown in Figs 2.4(c) and 2.4(d)). The exact value of $\Phi_O(d_O)$ depends on the field strength, the patch sizes and the local work function differences. Bundaleski et al. computationally determined the quantitative effect of this patch field by showing the expression of $\Phi_O(d_O)$ for a surface consisting of patches with two work function values Φ_{H} and Φ_{L}[8,112] can be written as:

$$\Phi_O(d_O) = \langle\Phi\rangle - (\langle\Phi\rangle - \Phi_{\mathrm{L}})\frac{F}{F_0}\left(1 + ln\frac{F_0}{F}\right) \qquad \text{Eq 2.12.1}$$

with

$$F_0 = \frac{\Phi_H - \Phi_L}{ek\sqrt{S}} \qquad \text{Eq 2.12.2}$$

where $\langle\Phi\rangle$ is the area-weighted average work function, e is the elementary charge, k is a material-dependent constant that is typically close to 0.5 when the patch shapes are not very elongated (for example, close to a circular or square shape), S is the area of a single patch (assumed to be the same for each type of patch), and F is the applied field. Eq. 2.12.1 predicts that $\Phi_O(d_O)$ decreases as the applied field increases, ultimately reaching Φ_L when F reaches F_0. F_0 can therefore be understood as the critical field needed to reveal the lowest work function by negating the patch field effect. By neglecting pre-factors on the order of magnitude of 1, the value of F_0 can be roughly estimated by dividing the surface work function difference (in volts) by the patch lateral size dimension. It is noted here that typically F_0 is still too weak to trigger significant Schottky effect discussed in Sec. 2.2.1.2. It should be noted that to have physical meaning, Eq. 2.12.1 is only valid for the case when $F \leq F_0$. In the case of $F > F_0$, $\Phi_O(d_O)$ will always approximately equal Φ_L until Schottky effect is large enough to significantly lower $\Phi_O(d_O)$. When $F > F_0$, the applied external electric field is strong enough to overwhelm the patch fields arising from local work function heterogeneity, and electrons collected at remote location O are observed to arrive consistent with having escaped an energy barrier of the lowest local work function, Φ_L. *An important implication of this result is that $\Phi_O(d_O)$ on patchy surfaces are not necessarily equal to any local work function of any surface and must be interpreted with great care.* Further discussion on the impact of patch field effects on experimental work function measurement is included in Secs 2.3.1.2 and 2.3.3.

The discussions in Secs 2.2.1.2 and 2.2.1.3 illustrate that there are at least two common work function definitions. The first is the local work function, which is an intrinsic property of the material and the considered surface. The second is the observed work function, which is controlled by the barrier energy to remove the electron and may or may not be equal to any local work function of a specific surface, depending on patch and external field conditions. When discussing the properties of a specific material surface, the term work function should always be referred to the local work function. On the other hand, the observed work function is an important quantity directly available through work function measurement, which will be further discussed in Sec. 2.3.

2.2.1.4 Work function and related concepts in semiconductors

The above concept of work function and the associated discussions based on metallic systems can be applied to non-metallic systems (semiconductors and insulators with electronic band gaps) with some modifications. For a non-metallic solid, the Fermi level typically lies within the band gap, where the density of states is zero. In this case it is often useful to define the ionization energy (IE), which is the energy required to remove an electron from the valence band maximum (VBM) to the local vacuum level, and the electron affinity (EA), which is the energy gained by adding an electron from the local vacuum level to the conduction band minimum (CBM), shown in Fig 2.5. Compared to metallic systems, semiconductors have much lower free carrier density and thus much longer screening lengths. Consequently, the influences of ambient electric fields and surface states result in near-surface band bending, making IE, EA and work function physics more complex. Nevertheless, each of these quantities exhibits similar behavior

with respect to local and non-local vacuum levels as well as patch and applied fields as the metal work function[113,114].

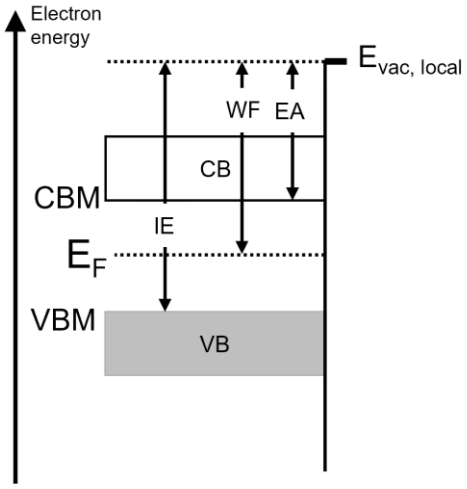

Fig 2.5. Schematic band diagram and work function for a (non-degenerate) semiconductor together with its ionization energy (IE) and electron affinity (EA).

The Fermi level in a semiconductor can have a range of values from just below the VBM (in the limit of degenerate p-type doping) to just above the CBM (in the limit of degenerate n-type doping). For example, for an intrinsic semiconductor at a temperature just above absolute zero, the Fermi level resides in the band gap where the density of states is zero. In the limit of the semiconductor being p-type, the Fermi level resides near the VBM; while in the limit of the semiconductor being n-type, the Fermi level resides near the CBM. The IE, EA, and work function are all direct measurements of the surface electronic properties of a material, as shown in Fig 2.5[113,115]. For the case of a degenerately-doped semiconductor, the Fermi level may be sufficiently n-type (p-type) such that the work function has a lower (higher) energy than the EA (IE). In the non-degenerate doping case, direct knowledge of the work function and band gap provide values of the resulting IE and EA. As discussed in Sec 2.1.2, such modifications on Fermi

level (a.k.a. electrochemical potential) is critical in a number of applications involving relative energy level alignment[113,116,117].

2.2.2 Factors controlling the work function, work function engineering mechanism

The energy of an electron being removed from a material to vacuum at a point in space outside the material has contributions from the starting energy (which is determined by the band structure of the material), image charge potential, electric fields from the presence of different surface patches, and effects of any externally applied electric fields. In the case with no externally applied electric field or patch fields, the work done on the electron by the surface is determined by many multipoles, but it is generally assumed that the dipole dominates the energetics, because of the rapid decay of multipole fields ($\sim 1/x^3$ for dipoles versus $\sim 1/x^5$ for quadrupoles and even faster for higher order multipoles) and the natural tendency for charged atoms and their compensating charge to be close together in dipole type structures. Furthermore, the image charge potential is similar among different materials, as long as the material has a relatively large dielectric constant ε (e.g., the dielectric constant is larger than ~2), as the image charge potential energy for an electron above a dielectric is:

$$E_{img}(\varepsilon) = \frac{\varepsilon - 1}{\varepsilon + 1} E_{img}(\text{metal}) \qquad \text{Eq 2.13}$$

Under these conditions and approximations, the values of material work functions are determined by the material-specific electronic band structure and surface-specific surface dipole. Given this, understanding and controlling the work function in a material is typically generally accomplished by modifying the bulk electronic structure, which governs the Fermi level location relative to the *intrinsic vacuum level* (the hypothetic

vacuum level in the zero-surface-dipole scenario), and the surface dipole, which modifies the local vacuum level energy and makes the work function a surface-sensitive quantity.

Although the work function modification is deconvoluted into two categories, in practice it is possible (or even common) that one work function engineering method has mixed effects of two. As an example of bulk electronic structure altering surface dipoles, an increasing Fermi level with bulk doping might fill surface states and thereby change the surface dipole. Surface changes can also effectively alter electronic structure far into the bulk of the material when the electrical screening of the materials is low due to their being few mobile charges available for screening. For example, surface adsorbates may dope electrons (holes) into the system, creating a positively (negatively) charged surface adsorbate which acts to increase (decrease) the surface dipole, and also simultaneously raise (lower) the Fermi level of the near-surface material. Thus, for materials with low electrical conductivity (e.g., semiconductors or non-transition metal oxides), the effects of surface dipoles and bulk electronic structure modification may become coupled in the near-surface region, complicating understanding and analysis of the work function.

2.2.2.1 Tuning bulk electronic structure

The bulk electronic structure, determined by composition, structure, dopants, defects, pressure, and many other factors, sets the Fermi level with respect to the intrinsic vacuum level, and consequently also affects the work function: a higher (lower) Fermi level results in a lower (higher) work function, given the surface dipole remains unchanged. The Fermi level can be directly modified by doping free carriers into the material. Meanwhile, it is also possible to tune the Fermi level by altering the shape of the band structure by composition changes, oxidation state variation, and defects.

When a materials is doped, the dopant atoms will not only provide excess free carriers, but also add dopant energy levels that modify the original band structure, and both of these effects will change the electron filling level[99,118]. This doping strategy is typically employed in semiconductors or transition metal oxides. Klein et al. have studied

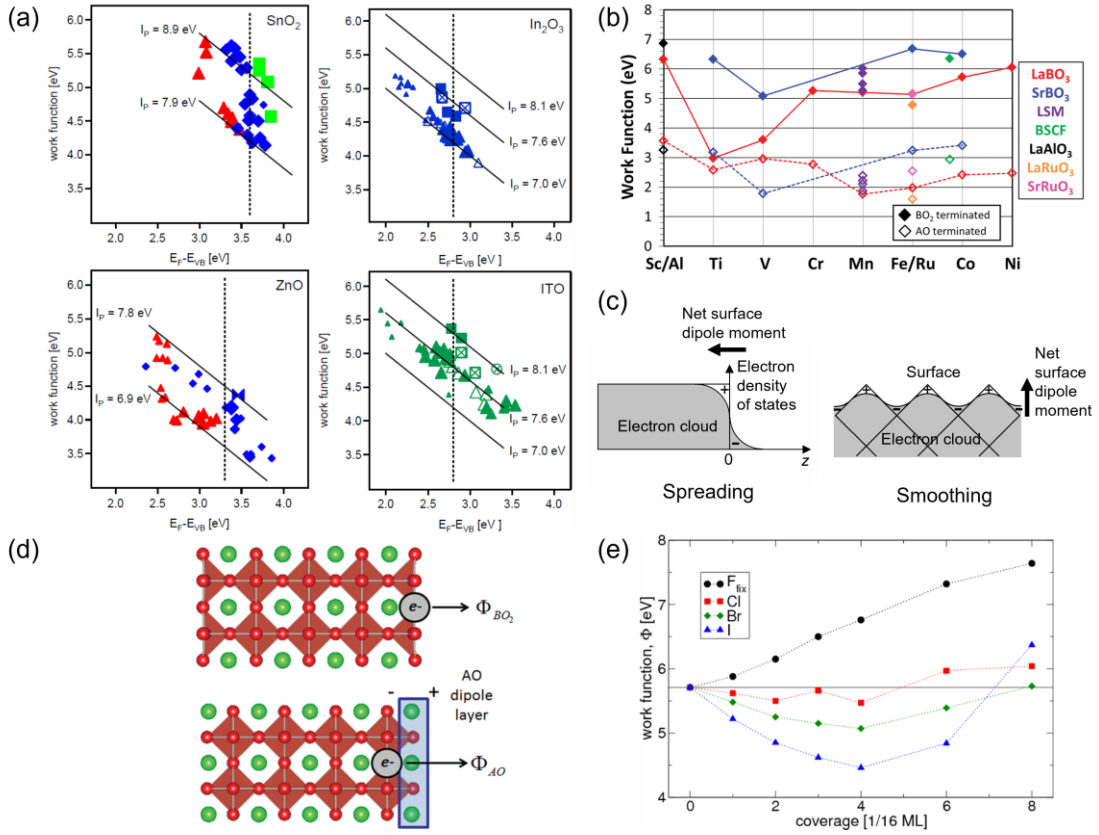

Fig 2.6. Different work function tuning mechanisms. (a) The work function dependence of Fermi level for different TCOs (from Ref. 99. Copyright: open access, credit to the original authors). (b) Computational results for a series of perovskite (001) work functions with different terminations (typically AO and BO_2 terminations have opposite dipole moments) (from Ref. 67 ©2016 John Wiley & Sons, Inc). (c) The spreading and smoothing effect of electron clouds [32], creating dipole moments on a simple metal. (d) The atomic structure of a perovskite, an example of polar materials where the AO- and BO2-terminated surfaces have opposite surface atomic arrangements and therefore opposite dipoles (From Ref. 67 ©2016 John Wiley & Sons, Inc.). (e) DFT-calculated platinum electrode's work function dependence on different adsorbed halide functional groups (from Ref. 143. Copyright: open access, credit to the original authors).

transparent conductive oxides (TCOs) such as Al-doped ZnO, SnO_2 and indium tin oxide (ITO)[99], and quantified the Fermi level shift and work function change in terms of dopant and material processing methods. As shown in Fig 2.6(a), the work function is negatively related to the Fermi level. That is, the work function decreases as the Fermi level is increased above the VBM.

In the limit of very high doping levels (e.g., a few percent or more), the material is effectively alloyed, and the composition is tuned significantly, leading to significant changes to the band structure. This is typically the case of work function engineering via Fermi level modification in transition metal oxides, in which case not only the electron filling level has been changed, but also the band structure. It could be imagined that with high composition flexibility, composition tuning can be used for more precisely altering the band structure. For example, Jacobs et al. investigated a series of perovskite oxides with different compositions (see in Fig 2.6(b)), showing that compositional change could alter the band structure, primarily the O 2p band center, which essentially correlates to Fermi level and therefore the work function[67]. Meanwhile, the electronic band structure might also vary with the cation chemical states or defect concentrations, especially for transition metal oxides, in which the cations may adopt different d-band filling levels associated with stoichiometry and oxygen vacancy concentration. Greiner et al. measured the work function for a set of transition metal oxides. Their work suggests that the work function decreases with decreasing cation oxidation states and increasing oxygen vacancy concentration[119], which could be attributed to increasing donor doping states associated with oxygen defects, and higher concentration of low electronegativity cations.

Another possible way to tune the bulk electronic structure is to introduce strain into the original material. Peng et al. have studied the work function of armchair graphene nanoribbons (AGNRs) under different strain states with DFT calculations[120], and saw an increase in work function under tensile strain. This change could mainly be attributed to the changes in Fermi level associated with bulk electronic structures evolution under different strain states, since the local vacuum level barely changes during this evolution.

The work function modification magnitudes realized from doping, significant composition changes, and strain, are varied. By altering the material composition and cation valence states, the work function could change by a few tenths of an eV to up to a few eV when the band filling levels become significantly altered. Strain, on the contrary, generally has a minor effect on the band structure compared to the changes resulting from compositional and valence state effects, making the modification of work function smaller, typically on the order of 0.1 eV[67,119–121].

2.2.2.2 Tuning surface dipole

Besides the bulk electronic structure, surface properties also significantly influence the work function. This modification manifests as an effective surface dipole effect, although the detailed surface physics might be very complex.

Back to 1941, Smoluchowski[32] showed that for a simple elemental metal, a surface dipole originates from the electron cloud on the surface seeking the lowest energy configuration, accomplished through spreading and smoothing of the electron cloud (see Fig 2.6(c)). The electron cloud spreading creates a negative dipole and increases the work function, while the smoothing of this electron cloud has the opposite effect. The magnitudes of these two effects are typically similar in absolute value, approximately a

few tenths of eV, but do not completely cancel, thus resulting in a net dipole for every surface. For a more complex material system such as an oxide or other multicomponent system, the dipole could come from the polarity introduced by the top-most atomic layer and the layer immediately beneath it. Such dipoles can be quite large, where the energy modification could be on the scale of a few eV[67,122]. Furthermore, any changes in the surface atomic configuration, such as differences in surface orientation (e.g. (001) versus (111) surfaces of W) or termination (e.g. (001) SrO terminated $SrTiO_3$ versus (001) TiO_2 terminated $SrTiO_3$ as illustrated in Figs 2.6(b) and(d)[67]), surface reconstructions, or adsorbed molecules or atoms, can lead to significant changes in the charge distribution at the surface, translating into significant changes in the work function.

The scale of surface dipole effects can be understood in terms of the Helmholtz equation, which gives the relationship between work function change $\Delta\Phi$ and surface dipole density from an electrostatic potential perspective:

$$\Delta\Phi = -\frac{e}{\varepsilon_0}\mu_z(N)N \qquad \text{Eq 2.14}$$

Here, e is the elemental charge, N is the density of surface molecules, and $\mu_z(N)$ is the dipole moment per molecule that is perpendicular to the surface[123,124]. This equation can be understood by considering the surface dipole as a charged parallel capacitor, and the resulting work function change equals the potential energy change when an electron passes through the capacitor. Such model is well supported by numerous computational works, showing that after applying reasonable estimates of dipole density and moments, the Helmholtz equation gives good estimations for the work function modifications[5,125,126].

In general, work function engineering through surface dipole modification could be categorized into tuning intrinsic dipoles of the materials and introducing external dipoles through surface treatments. Intrinsic surface dipoles typically have small magnitudes, especially for metals and metal alloys, and therefore a small effect on work function (typically on the order of a few tenths of an eV). For example, conduction electrons in metals and alloys are well-modeled as an ideal Fermi gas, and their surface dipoles are mainly from smoothing or spreading, where the actual elemental composition near the surface and associated charge plays a small role[32]. Thus, the work functions of most metals are 4 to 5 eV, except for alkali and alkaline earth metals which generally have work functions around 2 to 3 eV. Furthermore, the work function differences between different orientations and surface terminations for metal systems are small, around 0.3 to 0.5 eV[127,128]. However, in more chemically complex material systems such as oxides, the simple Fermi gas model is no longer applicable since the electrons are mostly ionically or covalently bonded or localized near the ions. The distinct charge states among different elements cause large variations in both the Fermi and vacuum levels for different materials and different surface terminations, resulting in a large spread of work functions from ~0.85 eV for Cs_2O[129] to 7 eV for V_2O_5[130]. For chemically complex materials like oxides, due to the electronegativity differences among different compositional elements, the top-most atomic layer and the layer beneath may lie in different charge states, forming a polar surface with a dipole moment as large as several eV estimated by Eq 2.14. In these cases, tuning the intrinsic dipole moment may be an appealing approach for work function engineering[67,121,122,131,132]. In first principles calculation works by Jacobs et al.[67] and Zhong and Hansmann[121], the (001) AO-terminated and BO_2-terminated work functions in

perovskite ABO_3 compounds are predicted to differ by over 4 eV. For example, according to Jacobs et al., SrO-terminated $SrVO_3$ is predicted to have a 1.86 eV work function, whereas the VO_2-terminated counterpart is predicted to be 5.89 eV. This large work function range of oxides is also evident from experiments, which will be further discussed in Chapter 3. Chambers et al. has measured the work functions of (001) SrO- and TiO_2-terminated Nb-doped $SrTiO_3$[132], showing a 1.5 eV difference between these two terminations. Similarly, the origin of low work function surfaces in some commercial thermionic emitter materials such as LaB_6 and CeB_6, can also be at least partially attributed to an intrinsic dipole moment between the cation layer and boron framework[63,64]. This suggests that by exploring material systems, tuning compositions, and selecting surface orientations and terminations, it may be possible to access a wide range of work function values by altering intrinsic dipole moments.

To stabilize the intrinsically highly polar surfaces, it is likely that materials with high electrical conductivity needed. Typically, strongly polar surfaces are not stable due to the additional electrostatic energy introduced by dipoles[133]. Insulators compensate such a dipole with surface adsorption or reconstruction, diminishing the intrinsic dipole moment[134,135]. On the other hand, with enough free electrons, metallic systems can simply screen such a dipole moment by moving electrons[136,137]. In order to achieve metallic behavior in oxides, transition metal elements should be included to provide additional electrons for the formation of a partially filled conduction band. This explains why perovskites have been investigated for work function engineering with an intrinsic dipole moment. Other conductive oxides such as spinels[138] or Ruddlesden-Popper phases might

also be amenable to significant, stable intrinsic surface dipoles, which could be an open research opportunity to explore material systems for work function engineering.

Although the surface dipole could be in principle tuned by exploring composition and structure of different materials, in practice it is often challenging to find a material that has both a significant surface dipole and good properties in other application aspects, such as melting point, electrical conductivity, mechanical strength. Therefore, modifying the surface dipole by surface treatments of the base material for the proposed application, may offer more practical appeal. A good example of this surface treatment approach is the dispenser cathode discussed in Sec 2.1.2.1[3], in which Ba evaporates from impregnates during operation and form a BaO monolayer on top of the tungsten body, creating a large surface dipole that reduces the W intrinsic work function by over 2.5 eV[3,124]. Similarly, GaAs and AlGaAs photoemitter work functions are modified by cesiation of their surfaces. Additionally, other functional groups, such as halides, -OH or -H, -O (or O_2), have also been used for modifying the work function of graphene, MXene, bare metals, etc.[120,139–143] The work function modification is typically associated with charge transfer between the base material and the functional group. Generally, the surface species with higher electronegativity, such as -O, tends to attract electrons from the material, creating a dipole that increases the work function. Other adsorbates such as -H tend to donate electrons and create dipoles that decrease the work function[120]. However, according to the Leung et al.[141], this is not always the case as the charge transfer and the electron cloud behavior could be complex on the surface. In some cases, for example O on W, the work function may decrease for certain arrangements of O on W when the spreading of the electron cloud tail creates a positive effective dipole relative to its clean surface counterpart.

Surface dipoles are also modified by other surface treatment methods, such as sputtering and chemical etching [144–146], which are effective approaches for work function engineering for specific applications. For example, Joo et al. explored BCl_3/Ar plasma etching of Al-doped ZnO thin films, reporting a 200 meV work function increase resulting from this treatment. Bruening et al. studied the effect of chemical etching of CdSe, reporting significant modifications of the work function, including increases of 0.5 to 0.7 eV with oxidizing etching, and decreases of 0.3 eV with a following reducing etching[146].

2.3 Work function measurement and computation methods

The importance of the work function for many materials science and engineering applications (see Sec 2.1.2) makes accurate measurement and prediction crucial to both understanding material properties and designing new materials. Over the last century a number of techniques have been developed to measure work functions. The most commonly used measurement methods are based on electron emission (with photo, thermionic or field emission) and contact potential difference (CPD)[110,113,115,116]. In this section, these methods are specifically discussed in the context of the electrostatic energy profile (Sec 2.2.1). It is emphasized that regardless of the method employed, the measured quantity is always the *observed work function* Φ_o at the detection probe, such as a photoelectron spectrometer, an adsorbed Xe atom, a KPFM tip, or an emission-testing anode. Thus, the measured quantity is always influenced by the previously discussed effects of surface patch and externally applied fields so that the measured value, Φ_o, may not equal a local surface work function Φ_l.

Besides direct experimental measurements of work function, it is also important to develop mature approaches to calculate the work function via computational tools.

Computational predictive models not only enable relatively fast exploration of the work function values of different materials, but also deepens understanding of the relationship between work function and other physical properties such as atomic number, valence state and surface chemistry. Historically, physics-model based methods such as the free electron gas model and jellium model were used to calculate the work function of simple metal systems. More recently, with the rise of computational science and technology, DFT-based work function calculation has become the primary method to predict work functions and has enabled expansion of theoretical predictions to more complex systems, such as oxides, borides and nitrides, organic compounds, and lower-dimensional materials.

2.3.1 Photoemission-based measurements

Photoemission-based measurement, typically ultraviolet photoelectron spectroscopy (UPS), is the most widely employed method for reliably measuring the absolute work function due to its standardized experimental setup, good electron energy resolution, and the availability of high-brightness photon sources[147]. UPS directly employs the photoelectric effect by measuring the kinetic energy of a photoelectron emitted by the absorption of an incident photon. However, one should take extra caution when processing UPS data with regard to applying a suitable bias, setting up the correct sample-detector geometric configuration, and interpreting data properly to understand how the observed work function relates to the local work function(s).

Due to conservation of the photoelectron energy when traveling in the non-uniform vacuum level (i.e., electrostatic potential energy) towards the electron detector, the work function could not be directly derived by subtracting the photoelectron kinetic energy from the incident photon energy[110]. Consequently, as pointed out by Cahen and Kahn, the

standard approach to calculate the work function from UPS data is to subtract the photoelectron spectrum bandwidth W between the Fermi edge E_F and the secondary electron cutoff $E_{vac,barrier} - \mathrm{h}\upsilon$ (i.e., $W = E_F - \left(E_{vac,barrier} - \mathrm{h}\upsilon\right)$), from the photon energy $\mathrm{h}\upsilon$[110,148] (an example is shown in Fig 2.7(a)[148]).

$$\begin{aligned} \Phi_O(\mathrm{UPS}) &= E_{vac,barrier} - E_F \\ &= \mathrm{h}\upsilon + E_{vac} - \mathrm{h}\upsilon - E_F \\ &= \mathrm{h}\upsilon - W \end{aligned} \qquad \text{Eq 2.16}$$

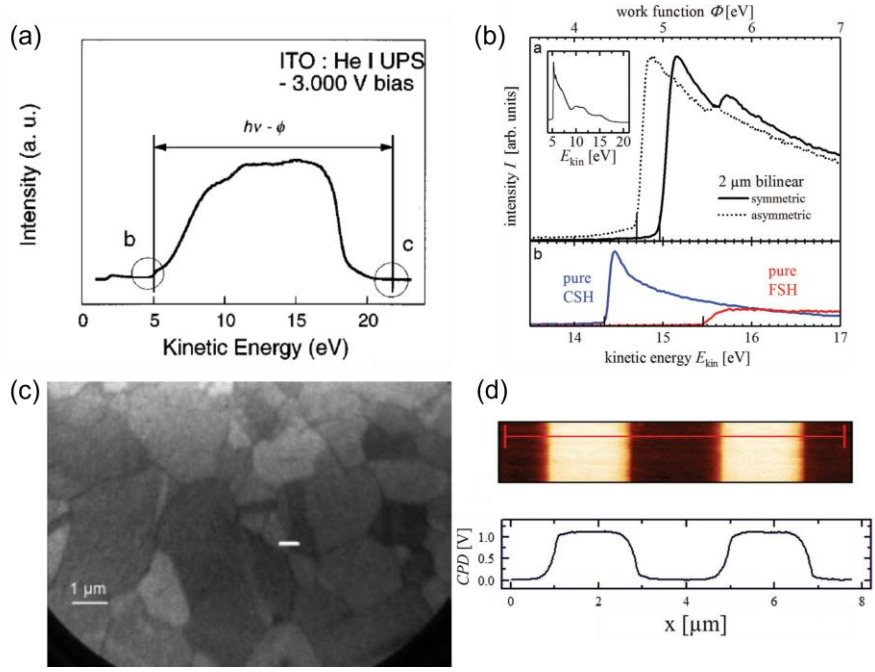

Fig 2.7. (a) A set of real data for UPS-measured ITO work function (reprinted from Ref. 148 with the permission of AIP Publishing). (b) Measured work function with UPS on a heterogeneous surface with weak field, resulting in an average value across the surface (from Ref. 149 ©2017 John Wiley & Sons, Inc). (c) An example of PEEM image on polycrystalline copper (from Ref. 162 ©2006 John Wiley & Sons, Inc.), with different work functions indicated by brightness differences. This suggests the local work functions for microscopic grains are resolvable under high applied field. (d) An example of KPFM work function mapping for a heterogeneous surface (from Ref. 149 ©2017 John Wiley & Sons, Inc). The zebra-crossing pattern deposited with two different organic molecules, namely FSH and CSH, have a local work function difference of 1 eV, which is directly detectable via KPFM.

During a UPS work function measurement, typically a small negative sample bias (5 to 10 V) will be applied to guarantee an overall negative electric field (one that accelerates the photoelectrons away from the sample and towards the detector)[110,149,150]. As discussed in Sec. 2.2.1.2, when measuring a homogeneous metal surface, this field will make the observed work function Φ_O(UPS) equal to the surface local work function Φ_l. Meanwhile, as pointed out by Helander et al., the sample surface needs to be perpendicular to the spectrometer, in order to avoid measurement artifacts caused by geometric configuration[150]. Additionally, surface charge can significantly perturb the measured binding energies and work function, so the sample must have good electrical conductivity and contact with the sample holder. If the sample is a semiconductor with poor electrical conductivity, the measurement is typically conducted with a thin film sample[151,152], and one must carefully calibrate the Fermi edge location, commonly towards a noble metal electrode that is electrically connected to the sample surface.

For a heterogeneous surface, the work function interpretation will possibly be significantly affected by the patch field, as discussed in Sec 2.2.1.3. Therefore, the observed work function measured by the spectrometer depends on the intensity of the applied negative electric field compared to the critical field in Eq. 2.12.2. In the absence of a strong applied electric field comparable to or greater than the critical field, the work function value measured for a heterogenous surface with multiple work functions will be *a patch-area-weighted average*. As the negative applied field becomes stronger, the measured work function will decrease, asymptotically converging to *the lowest local work function* across the surface when the external field exceeds the critical field[111]. An approximate solution of Eq. 2.12.2 for the typical applied bias (~10 V) and sample-to-

detector distance (~1 mm) within UPS measurement shows that one would not be able to get the lowest work function if the patch size is smaller than ~100 μm, assuming the work function heterogeneity is on the order of 1 eV among different patches. Therefore, patch field theory implies that nearly all cases of work function measurement by UPS are in fact the area-weighted average of the individual patch local work functions.

Several recent experimental investigations confirm the conclusion that UPS-measured work functions are typically the area-weighted average of individual (patch) local work functions. Bundaleski et al.[8], and Schultz et al.[9,149] have studied the photoemission-observed work function of several example surfaces with heterogeneous work function distributions, providing excellent agreements with patch field theory by observing a surface-averaged work function value for a weak applied field, and the lowest local work function value for a strong applied field compared to the critical field (see in Fig 2.7(b)). It should be noted that it is the electrostatic potential spatial distribution—including the patch field—that causes this averaging effect, rather than the limited spatial resolution or large incident photon spot size. Therefore, even if one were to illuminate a single, micron-sized, low-local-work-function grain with a highly focused light source, the UPS measured work function would still be the area-weighted average value across a large area (e.g., millimeters in size), as long as the applied electric field is much weaker than the critical field. On the other hand, UPS would be able to capture the lowest local work function on a micron-sized patch with a centimeter-sized photon spot, if the applied field is strong enough compared to the critical field.

The discussion above excludes the influence of surface morphology on the effective work function values. According to some studies, surface roughness may significantly

modify the work function. However, different studies provide different conclusions on how the work function is modified. Some argue that the work function decreases with increased surface roughness[153–155], while others suggest an opposite trend[156]. Overall, there does not appear to be a consistent understanding of the physical mechanism behind morphological influences on the work function currently[40,157–160], and further work is still needed to reveal the relationship between the observed work function, surface morphological features such as roughness, and the impact of patch fields. Nonetheless, as discussed in Sec 2.1.2.1, tuning surface morphology to include extremely high-aspect-ratio features (e.g., sharp tips) has been widely used in field emission to reach a high local field.

To measure the lowest local work function on a heterogeneous surface from a remote point, a sufficiently large field is required in order to overcome the patch field effect. Such fields are present in the case of photoemission electron microscopy (PEEM)[93,161–164], with a ~1 V/μm typical applied field that is capable of cancelling out the patch field effect on a surface with >~1 μm patches and <1 eV work function differences. As a result, the work function distribution across the sample surface is expected to be resolvable, and it is possible to map out the lateral work function distribution. An example of such a result is given in Fig 2.7(c), where the brightness of different areas represents different relative work functions, with brighter regions indicating a lower work function. In order to obtain the absolute work function values, a spectroscopic measurement is also needed during PEEM experiments[162]. Alternative approaches to obtaining the local work function value include photoelectron spectroscopy of adsorbed xenon (PAX) and two-photon photoelectron spectroscopy (2PPES) proposed by Wandelt[165]. PAX uses the 5p core level energy shift of adsorbed xenon atoms to monitor the surface local electrostatic potential,

while 2PPES measures the energy levels of hydrogen-like surface states that transiently trap photoelectrons[165]. In both cases, the local vacuum levels on the surfaces have been directly measured, which will yield surface local work function values.

2.3.2 Measurement based on contact potential difference (Kelvin probe)

The work function can also be obtained by measuring the contact potential difference (CPD) with a well-characterized reference material surface. This method is known as Kelvin probe (KP). Modern KP experiments are frequently performed with an atomic force microscope (AFM) using a non-contact operation mode setup, called Kelvin probe force microscopy (KPFM)[166–168]. The probe (cantilever and tip for the case of KPFM) is usually made of a conductive material with a well-known local work function value and high chemical stability, e.g., tungsten, gold, platinum, or silicon coated with such metals.

In a typical KP/KPFM experiment, the sample and the tip are in electrical contact through an external circuit, and an AC voltage is superimposed onto a DC bias applied between the sample and the probe. The external electrical circuit connection ensures that the sample and probe tip share a common Fermi level. The total voltage between the tip and the sample is:

$$V = (V_{DC} - V_{CPD}) + V_{AC} \sin \omega t \qquad \text{Eq 2.17.1}$$

where V_{CPD} is the CPD and ω is the frequency of the AC voltage. The force between the sample and the tip can be derived as:

$$F = \frac{1}{2}\frac{dC}{dz}V^2 \qquad \text{Eq 2.17.2}$$

where C is the capacitance between the sample surface and probe. This force has three frequency components, corresponding to 0, ω and 2ω, and the ω component is proportional to $(V_{DC} - V_{CPD})$. Therefore, when tuning the DC voltage bias to make the ω force component zero (or in a real experiment, a value very close to zero) the applied V_{DC} will be equal to V_{CPD}, which is also equal to the work function difference between the sample and the probe[166]:

$$\Delta\Phi = eV_{CPD} = eV_{DC} \qquad \text{Eq 2.17.3}$$

Kelvin probing directly measures the force derived from the electrostatic potential gradient influence on the probe. Therefore, $\Delta\Phi$ in Eq. 2.17.3 is the difference between the sample's observed work function at the probe Φ_O(probe), and the probe tip (local) work function. In a macroscopic (large-area tip) KP experiment, Φ_O(probe) might be equal to the average work function on the sample surface. In contrast, the small distance between the tip and sample (~10 nm) in a typical KPFM experiment means that *the observation point* is *the local point*, enabling the direct measurement of the sample's local work function, un-perturbed by patch field averaging. Moreover, since KPFM is a microscopic technique, it is also possible to map out the lateral distribution of the surface local work function and simultaneously provide a lateral spatial measurement resolution on the order of the probe tip size. As a result, KPFM measurements can provide local, rather than the average, work function values across the surface (see Fig 2.7(d))[149].

Many KP/KPFM instruments are operated in an atmospheric ambient environment, so the surface may experience contamination (e.g., adsorption of O_2, H_2O, CO_2) that will influence the observed work function. For example, Kim et al. have reported that KPFM

measured work functions of ITO in air or Ar disagree with UPS measured work functions measured under ultrahigh vacuum (UHV) conditions[169]. However, this is a consequence of the surface contamination, and not because the KP/KPFM work function measurement is fundamentally unreliable. As Beerbom et al. pointed out, UHV-based KP provides highly reliable work function measurements[170]. Another advantage of KP/KPFM is its non-perturbative nature due to its non-contact measurement mode, avoiding irreversible damage on the surface, which can potentially be an issue with high-energy photons in photoemission-based methods[170]. Consequently, the KPFM work function would be expected to offer greater validity and reliability in this particular use case[170].

2.3.3 Other experimental methods – thermionic and field emission

(This section was originally written by Dr Dongzheng Chen and Lin Lin. Prof John Booske also made significant contributions. Issues related to thermionic emission were also discussed with more details and physical models in Dr Chen's dissertation.)

There are additional approaches to measure the work function by exploiting other mechanisms for electron emission from the surface. These include thermionic emission, where the electron gains enough thermal energy to leave the surface at high temperature, and field emission, where the electron tunnels through a narrow energy barrier resulting from a strong external electric field.

The RLD Eq 2.3[22,171] with Schottky barrier lowering[25,111] (Eq 2.11) describes the behavior of thermionic emission current density J_T at temperature T from a cathode with a single work function Φ (i.e., no patch field). In order to make it convenient to read the following content, Eq 2.3 is written one more time here:

$$J_T = AT^2 \exp\left(-\frac{\Phi}{kT}\right) \qquad \text{Eq 2.3}$$

The temperature variation method, also called as the "total current" method, is frequently used to measure Φ by fitting the RLD Eq 2.3 to experimental data[172–174]. In particular, the standard practice is to fit a straight line to a graph of ln (J_T/T^2) versus $1/T$, extracting an *apparent* work function from the slope. However, it is important to recognize that this apparent work function value is also associated with an apparent value for the pre-exponential Richardson constant A, especially for heterogeneous emitting surfaces.

The theoretical value of A is traditionally predicted by treating the electrons as a non-interacting electron gas, and determining the classical rate of overcoming a potential step of Φ from thermal excitations given by Fermi-Dirac distribution for the conduction electrons. This approach gives a value of $A_0 = 4\pi mek^2/h^3 \approx 120\ \mathrm{A/cm^2/K^2}$ [35]. However, this approach ignores a number of factors, including (i) real materials have very different densities of states than non-interacting electron gas, (ii) electrons will reflect due to quantum mechanical scattering at the surface (or, more precisely, the rates of tunneling from surface to vacuum states may be quite different from the simple assumptions of the traditional derivation[175]), (iii) electron depletion during emission[35,176,177], and so on. All these effects generally tend to lower the actual value of A below A_0, consistent with what is typically found experimentally and the requirement of detailed balance between metal and electron vapor[23]. For example, a fully quantum mechanical treatment of A was performed by Voss et al.[175], resulting in predicted values of A for W (110) coated with Cs in reasonable agreement with experiments that range from ~ 40 to 200 times smaller than A_0.

Meanwhile, examination of a number of published thermionic emission articles reveals that the current-versus-temperature data in many cases deviate, sometimes significantly, from the RLD Eq 2.3. This is an incentive for additional research producing more physically complex emission models. An example of a start in that direction is the emission model by Chen et al.[111] which shows how current emitted from a heterogeneous cathode surface can deviate significantly from the simplified RLD equation, but can be accurately predicted by a more complex model incorporating patch fields, Schottky effect, and space charge physics. Recent additional studies[178] suggest that for a heterogeneous cathode surface with multiple local work function values, when simultaneously fitting both A and Φ, patch-field-caused distortions on $J_T - T$ curves from Eq 2.3 can result in the fitted work function value being artificially lower than any local work function values actually physically present on the surface, coincident with an artificially reduced value for the fitted Richardson constant A[178]. Fig 2.8 shows the results of fitting simulated data from a model surface comparable with typical dispenser cathodes – a checkerboard consisting of only 2 eV and 4 eV local work functions. The fitted Φ = 1.57 eV is smaller than either of them, with a fitted A much smaller than its conventional theoretical value.

Given the uncertainty in A and in the applicability of the RLD form (Eq. 2.3) there is significant uncertainty in the meaning of apparent work function values extracted from fitting $\ln(J_T/T^2)$ versus $1/T$ data. This uncertainty is particularly significant when the emission behavior deviates from RLD Eq 2.3 (i.e., $\ln(J_T/T^2)$ versus $1/T$ is not linear) and especially when the fitting leads to A values differing from the conventional theoretical value by many orders of magnitude. The most objective conclusion to draw when RLD-data-fits imply a radically different A value from the conventional theoretical one is that

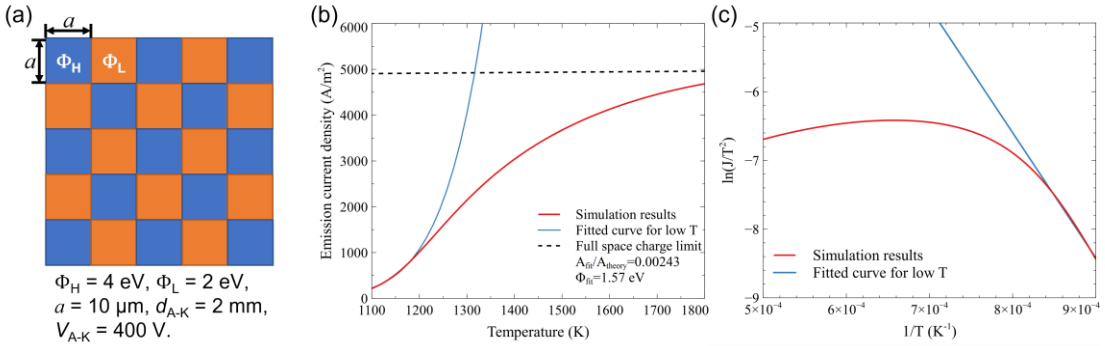

Fig 2.8. Simulation and fitting of the thermionic emission from a heterogeneous cathode with a checkerboard work function distribution, inspired by Dr Dongzheng Chen's Ph.D. dissertation[178] with different numerical values inserted. (a) The surface work function distribution and anode setup. The surface consists of 10 μm patches with 4 eV and 2 eV local work functions. (b) The simulated current density, full space charge limited current density and fitted curve for low temperature region, clearly showing a fitted work function (1.6 eV) much lower than any surface local work function, and a very small A (10^{-3} of the theoretical value). (c) The classical fitting procedure for the simulated emission current density by plotting $\ln(J/T^2)$ versus $1/T$ and linearly fitting the low temperature part.

the physics of the emission is not well-modeled by the simplified RLD equation and that the apparent work function therefore cannot be reliably identified as any particular local work function of an actual surface of the material under study. There is clearly a need to develop more advanced models of emission physics to capture non-RLD behavior and to understand the relationship between the measured emission current and the local work function(s) from heterogeneous thermionic cathode surfaces.

The above observations suggests that it is often insufficient to report an apparent work function fit to emission data to evaluate the thermionic emission performance of a cathode. Specifically, when emitted current density data yield an anomalously low value for the extracted pre-exponential constant A, it generally means that the emission is limited by complex physics mentioned above, and the apparent work function is not a true work

function of the surface and does not really capture the emission tendencies. Consequently, the emission performance may not be very promising even if it shows an extremely low fitted Φ (e.g., <1 eV). Thus, when discussing the thermionic emission behavior of a cathode by fitting the RLD equation, the fitted values of both A and Φ need to be reported. Alternatively, the anomalous value of the fitted A can be avoided by only fitting the work function value with A equal to its theoretical value A_0 [179,180], especially at the temperature(s) of interest to the application, which is known as the *effective work function* method. This provides a uniform scale to evaluate and compare the thermionic emission behavior of different cathodes, with the fitted *effective work functions* directly provide the benchmark for such uniform scale. More precisely, the effective work function method suggested by Hensley also includes a procedure of extrapolating emission current density to zero applied voltage along Schottky lines (combination of Eq 2.3 and 2.11, see Sec 3.3 for some detailed discussion), to avoid the Schottky barrier lowering effect.

Other thermionic emission measurement methods include the calorimetric method[172,173] and thermionic emission electron microscopy (ThEEM)[181,182] to measure the thermionic work function. Similar to PEEM, ThEEM is usually measured by applying a large electric field, so the patch field effect may become negligible. In those cases, ThEEM is able to provide information on the spatial distribution of the work function on a cathode surface. However, typical ThEEM microscopes require the emission current to remain low enough to avoid space charge distortion of the electron optics. Therefore, ThEEM measurements of work functions may need to be conducted at temperatures much lower than temperatures of practical application interest. If these practical applications rely on phenomena that change the emitting material surface conditions at high temperatures,

then the ThEEM-inferred values, while being correct for the temperatures at which they were measured, may not be the values associated with the higher temperature (higher emission current density) conditions of practical importance.

Similar to the case of thermionic emission, the work function can also be estimated from field emission experiments[116]. In this scenario, the F-N Eq 2.4 is the governing equation, and describes the emission current density from electrons tunneling through the potential barrier on the surface[31,35]. Field emission experiments are typically conducted with extremely high electric fields comparable to the image charge potential (on the order of 10^9 V/m). Hence, the observed work function is the strong field local work function discussed in Sec 2.2.1.2, where Schottky barrier lowering effect (Eq. 2.11) is significant. Furthermore, this field is strong enough to overwhelm the patch field created by patches larger than a few nanometers and the work function averaging effect will likely not be observed in these experiments.

As an analog of empirically extracting the work function in thermionic emission experiments by fitting to RLD Eq 2.3 with Φ (and perhaps A) as fitting parameter(s), the work function can again be inferred by empirically fitting the F-N Eq 2.4 to the field emission data. However, in practice, there are often significant challenges with this approach. First, all the issues discussed above for fitting the RLD Eq 2.3, except those due to patch fields, exist in fitting the F-N Eq 2.4, including the uncertainty in the appropriate value of A. In addition, field emitters are likely to have extremely sharp tips to enhance the local electric field, which could significantly complicate the relationship between the emission current density, the effective emission area and the applied electric field. For example, the current density is obtained by dividing the measured emission current by the

assumed emission area. However, the strong electric fields required for field emission typically result from field-enhancing sharp tips, including often unknown microscopically-sharp morphological surface features with high geometric aspect ratios. This makes it difficult to accurately know the emission area, which in turn makes it difficult to accurately infer the work function from the measured emission current versus externally-applied voltage data[183]. Furthermore, when measuring sufficiently high current densities, space charge will also play a role of distorting the F-N type emission current[184–187].

The work function could be measured through other approaches if it is involved in the related physics. For example, in a low energy electron microscopy (LEEM) experiment, the sample's work function could be measured by acquiring the transition voltage between the mirror mode and scattering mode with proper correction from the electron gun's work function, because such voltage suggests the minimum energy for an incident electron starting to interact with the material's electrons, exactly matching the work function definition. Again, since the technique is based on microscopic method with high extraction field, it is able to directly resolve the local work function as the patch field effect has been overcome.

2.3.4 A brief introduction to computational work function prediction

(This section was mainly written by Dr Tianyu Ma and Dr Ryan Jacobs in the original work, and was revised and summarized by Lin Lin for this dissertation).

Starting from mid-20th century, researchers started using simplified analytic theoretical models to calculated work functions for different materials. These include simple free electron gas model and jellium model, plus modifications from dipole layer,

pseudopotential and energy band hybridization, effectively predicted the work function of several metal systems[117,188–190]. However, at that time the computational capabilities were limited in the ability to numerically evaluate the resulting expressions, hindering any extensive systematic exploration. More significantly, these models were only reasonably accurate for simple material systems such as metals. For more chemically complex material systems such as oxides, organic compounds, materials with surface adsorbates, or low-dimensional materials, these traditional methods were not able to capture the actual charge distribution and therefore the work function. The advent of quantum mechanical computational methods like DFT have enabled researchers to circumvent these limitations.

The vast increase in computational power since the 1990s has made it possible to directly calculate the predicted work function of a material surface via quantum mechanics-based atomistic calculations. In solid state materials science, the most widely used quantum mechanical modeling method is DFT, which is based on the Nobel prize-winning development by Pierre Hohenberg, Walter Kohn and John Pople that the ground-state energy is a functional of the electron density[191]. DFT calculations of work functions of bulk material surfaces typically use periodic boundary conditions and a slab geometry, consisting of a section of the bulk material cleaved along a specific crystal plane. The termination of interest is thus exposed, and a vacuum region is introduced into the simulation cell. Similar to other calculations, DFT work function calculations are also subject to parametric convergence tests, including convergence of the cutoff energy of the plane wave basis set and *k*-point mesh, slab thickness, number of surface layers relaxed, and vacuum region thickness[137,192].

DFT has been used to calculate the work functions of many kinds of materials, including pure elements[193,194], metal hexaborides[195,196], transition metal carbides and oxides[67,121,132,197], and 2D materials like graphene and MXenes[198–201], among others, which generally indicate that modern DFT-based methods provide reliable work function predictions compared to experimental values, typically with an error of within 0.2-0.3 eV for most cases. Meanwhile, DFT allows for controlling the position of every atom being studied, such as introducing defects, modifying composition, placing adsorbates on the surface, changing surface orientation and termination, and adding strain[121,122,197], which opens the door to understanding trends and factors influencing the work function in ways that are not possible with experiment. Moreover, other materials properties, e.g., O 2p band center[12,201], and application aspects, e.g., dispenser cathode surfaces enabling high emission[65,202] and intermediate species in catalytic reactions[203], can also be correlated to work function through DFT, enabling deeper physical understandings as well as engineering optimization.

It should be noted that there are several disadvantages of predicting work function with DFT. First, the size of the surface slab usable in DFT calculations is still relatively small, usually no more than a few hundred atoms with a slab surface area smaller than a few nm^2, due to the limitation of computational power. This means DFT cannot directly accommodate defects at low coverage or concentration, surface features with long periodicity, or disordered, extended structural domains (in some cases it may be possible to extrapolate to the dilute limit the concentration dependence of the work function based on smaller simulation cells where the coverage or defect density is high). Also, introducing strong electron donors or acceptors such as O adsorbates into the small DFT simulation

cell may significantly alter the overall electronic structure[137], and associated corrections are needed to avoid misinterpretation of the outputs[204]. Additionally, slab calculations, especially with Heyd-Scuseria-Ernzerhof hybrid functionals[205], may be extremely time consuming (months on supercomputers), which also limits more efficient explorations.

Recently, a number of studies have employed data-centric machine learning methods to predict the work functions of various material systems, including elemental metals[206], complex oxides[207,208], binary and ternary materials[209]. The use of machine learning approaches for predicting work functions still remains in the nascent stage, which opens up great opportunities for materials scientists and data scientists to develop more powerful models for work function prediction.

2.4 Chapter summary and outlook

To sum up, the history, current impact, basic physics, tuning mechanisms measurements and calculations of work function have been discussed. The importance of work function in a vast array of applications in modern science and technology, such as vacuum and solid-state electronics, catalysis, and energy harvesting, emphasizes the necessity of solving the remaining confusion on work function, which is carefully discussed with an electrostatic energy treatment. The physics of work function is further discussed with the introduction of *observed work function* and evaluation of *patch field effect*, which also clarifies many work function measurement methods. The recent development of computational work function predictions, as well as a systematic summary of work function engineering methods, suggested interesting research areas of work function engineering.

There are many current and future research opportunities related to work function and its engineering. Across different application areas, there is an increasing demand for optimizing device performance by tuning the work function of a material to realize desirable band alignments, as well as other properties. For example, for thermionic emission applications, a low work function material with high electrical conductivity and stability would make a promising candidate of next-generation thermionic cathodes. By precisely controlling the work function difference in metal-semiconductor heterostructures, one could achieve desirable electronic conduction across interfaces. By carefully controlling the energy level alignment, it is possible to dramatically increase the performance of a material in important applications such as electrocatalysis, water splitting, and solid-state batteries.

Another opportunity involves systematic investigation of bulk materials or surface species that are suitable for work function engineering, including polar oxides such as perovskites and spinels, or different functional groups (fluorine, hydroxide, alkaline or alkaline-earth metal species, etc.).

Finally, there are fundamental aspects of work function physics that remain unresolved. For example, although having been studied for decades, thermionic emission from heterogeneous, non-ideal surfaces still lacks a thorough physical understanding, including a definitive explanation for low fitted Richardson constants that are typically correlated with low fitted work functions. Therefore, further investigation through advanced theoretical models of emission physics validated by careful experimental measurements will greatly benefit the scientific community.

Chapter 3 – Demonstration of low work function behavior on perovskite $SrVO_3$

This chapter is based on the journal article I first authored: **L. Lin**, R. Jacobs, D. Chen, V. Vlahos, O. Lu-Steffes, J. A. Alonso, D. Morgan and J. Booske, "Demonstration of low work function perovskite $SrVO_3$ using thermionic electron emission", *Advanced Functional Materials* (2022)[11]. The chapter contains the first experimental demonstration of low work function perovskite $SrVO_3$. In this work, the surface energy calculations of different $SrVO_3$ surfaces were processed by Dr Ryan Jacobs, with all the other experimental investigations led and mainly conducted by me.

3.1 Introduction

As discussed in Chapter 2, the work function is a fundamental surface electronic property of a material that is crucial in numerous applications involving electron migration across or towards surfaces and interfaces[1,5,117,210–214]. There is a strong interest in developing new materials and methods of tuning the work function to fulfill specific requirements in myriad technological applications.

Many applications require low work function materials, with one particular example of thermionic electron emission. As shown in Sec 2.1.2.1 and RLD Eq 2.3, lowering the work function of a cathode enables facile electron emission into vacuum to generate high-brightness electron beams at lower temperatures which is essential for vacuum electronic devices[3,215]. Given that the current W-based dispenser cathodes (with or without Sc) with Ba-containing impregnates has Ba contamination, lifetime and emission uniformity issues[3,58,59,65,216], realization of a stable material that exhibits a low

work function comparable to dispenser cathodes, as well as high electrical conductivity and robust stability under operating conditions, would be a major advance in thermionic emission cathode development.

One approach to achieve stability and low work function without volatile elements is to use monolithic materials with large intrinsic surface dipoles that exist in many oxide materials, with perovskite oxides (ABO_3 chemical formula) being an attractive example. The broad tunability of their A-site and B-site elements enables a large range of applications including catalysts[217], superconductors[218], oxide electronics[219], magnetic[220] and random access memory data storage devices[221], and piezoelectrics[222]. Perovskites consist of alternating layers of polar AO and BO_2 units along the ⟨001⟩ direction, leading to surface dipoles and presenting an exciting opportunity for realizing low work function surfaces in a bulk, monolithic material by virtue of the intrinsically polar {001}-oriented surfaces present in the crystal structure[223]. According to recent density functional theory (DFT) studies, many perovskite oxides, such as $SrVO_3$, $BaMoO_3$, $La_xSr_{1-x}MnO_3$, Nb-doped $SrTiO_3$, and $LaFeO_3$ might offer low work function values on their {001} oriented, AO-terminated surfaces[12,67,121,122]. Among these perovskites, previous DFT calculations predicted that $SrVO_3$ should exhibit a 1.9 eV work function for the {001} SrO-terminated surface[67]. Furthermore, $SrVO_3$ has other attractive properties motivating its use as a thermionic cathode. Specifically, $SrVO_3$ has been reported to be metallic with a high electrical conductivity[224,225], as demonstrated by its use as an electrode in oxide electronics[226]. It has also shown promise as an anode material for solid oxide fuel cells [227], demonstrating its high electrical conductivity as well as good stability in reducing environments[228,229]. The predicted low work function and experimentally demonstrated

high electrical conductivity and bulk stability under thermionic cathode operating conditions of high temperature and reducing conditions (due to ultrahigh vacuum) make $SrVO_3$ a promising new cathode for thermionic emission applications.

However, such low work function behavior (i.e., work function of ~2 eV or less) on perovskite oxides had not yet been experimentally observed previously. On the contrary, numerous experimental studies report much higher work functions. For example, the measured work functions on sintered polycrystalline samples on a number of perovskite systems showed quite high values: 4.3 eV, 4.5 to 5.1 eV, 4.6 eV, 5.0 eV, 5.5 eV, 4.5 eV, and 4.6 to 5.7 eV for $LaCrO_3$, $LaMnO_3$, $LaFeO_3$, $LaCoO_3$, $LaNiO_3$, Nb-doped $SrTiO_3$, and $La_xSr_{1-x}MnO_3$, respectively[71,81,82,230–232]. These values are all much higher than their corresponding {001} AO-terminated, DFT-predicted values of 2.77 eV, 1.76 eV, 1.98 eV, 2.42 eV, 2.47 eV, 1.2 eV, and 1.9 to 2.4 eV, respectively[67]. Even highly controlled measurements based on single crystalline or thin film surfaces have not yielded low work functions consistent with the predictions of DFT. For example, studies of Nb-doped $SrTiO_3$ have reported work function values ranging from 2.7 to 3.6 eV[71,131,132], again much higher than the 1.2 eV DFT prediction[122]. This fact does not mean these measurements or the DFT predictions of perovskite oxides are wrong (e.g., see a number of validations by Ma et al.[122] and Chambers and Sushko[132]), but there may be important differences between the experimental and somewhat idealized DFT systems. More precisely, the large discrepancies between DFT prediction and experimental measurement suggest the following open questions: Do the predicted very low work function surfaces on polar perovskite oxides really occur in nature? If so, can these low work function values be directly realized and used experimentally?

This work provides strong evidence that the answer is yes to both these questions based on experimental investigations of the work function of polycrystalline $SrVO_3$. It has been demonstrated that there are two main challenges to realizing low work function behavior on a complex oxide such as a perovskite. The first challenge is related to the complex surface chemistry, which can significantly affect the surface dipole and work function. The second challenge involves the physics of electron emission from a heterogeneous surface consisting of regions with widely varying work functions, where the patch field effect can significantly alter the observed work function from different experimental methods (see Secs 2.2.1.3 and 2.3)[1,8,149]. To demonstrate that the low work function polar surfaces on complex oxides (e.g., the {001} AO work function for a perovskite) can be formed and utilized for thermionic emission, the measurement needs to be performed *in-situ* under a condition relevant to thermionic emission, and with a local probe (e.g., KPFM) or strong applied electric field to reduce or remove the impact of patch fields.

To overcome the patch field effect and allow *in situ* characterization, thermionic emission measurements on $SrVO_3$ were performed with externally applied electric fields strong enough to reduce patch field effect. Such thermionic emission tests resulted in low effective work function values in the range of 2.3 to 2.7 eV, suggesting the presence of a significant fraction of low (~2 eV) work function surface when patch fields are considered. In addition, visual inspection of $SrVO_3$ surface grain morphologies from scanning electron microscopy (SEM) images combined with detailed DFT calculations of $SrVO_3$ surface energies suggest the low work function surface component is the SrO-terminated (001) surface. Meanwhile, the *ex-situ* UPS work functions for sintered polycrystalline $SrVO_3$

pellets were 3.45 eV for the as-sintered sample and 4.07 eV after sputtering and annealing. These results are similar in magnitude to previously studied perovskites described above, and much higher than the DFT-predicted value of 1.9 eV for SrO terminated (001) $SrVO_3$, but are consistent with patch field theory given the weak applied field in UPS. These UPS results show the importance of using *in-situ* and patch field reducing approaches to explore the work function of polar oxides.

Therefore, $SrVO_3$ likely has a stable, very low work function surface enabled by surface dipoles that can be realized under moderately high temperature and electric field and UHV conditions, suggesting $SrVO_3$ has significant promise for thermionic emitter applications. This result also provides experimental verification of patch field effect in perovskite oxides and suggests a practical approach for exploring low work function surfaces on heterogeneous systems with widely varying work function surfaces.

3.2 Experimental and computational methods

3.2.1 Sample Synthesis, treatments and characterizations

$SrVO_3$ bulk powders were synthesized via a wet chemistry sol-gel method which has been successfully used in previous works to synthesize related perovskite materials[233–235]. In a typical reaction, stoichiometric amounts of 1.288 g $Sr(NO_3)_2$ (Sigma Aldrich, 99.9%) and 0.712 g NH_4VO_3 (Sigma Aldrich, 99%) are dissolved in a solution containing 25 g of dissolved citric acid (Dot Scientific.inc, anhydrous) in 250 mL deionized water (18 MΩ·cm). The solution was slowly heated and kept boiling for 5 hours until the water was almost fully evaporated, and the solution formed a “souffle”-like texture. Then, the mixture was transferred to a box furnace and kept at 120 °C for 16 hours to evaporate the solvent.

After solvent evaporation, the mixture was heated to 600 °C with a 2 °C·min^{-1} ramping-up rate and kept at 600 °C for 12 hours to eliminate the nitrate and organic compounds in the system. The off-white product was then ground into a fine powder with a mortar and pestle, and calcined in 5% H_2/95% N_2 gas with a flow rate of 200 sccm at 1050 °C for 10 hours. To make samples for testing, the powder was pressed into disk-shaped pellets (with approximately 2.78 mm in diameter and 0.5 mm in thickness) at 300 MPa with a hydraulic press, and the pellets were sintered at 1350 °C in flowing 0.05% H_2 balanced with N_2 and Ar (which is achieved by mixing 2 sccm 5% H_2/95% N_2 gas and 198 sccm ultrahigh-purity Ar) for 9 hours. The H_2 gas concentrations used here were guided by previous DFT stability calculations on the energy above convex hull[236], and such energy was plotted versus temperature T and oxygen partial pressure $P(O_2)$, shown in Fig 3.1(a) (Figure 7 of Marks et al.[236]). Fig 3.1(a) suggests that $SrVO_3$ has a window consisting of intermediately high temperature and low oxygen partial pressure for which it is most stable (dark blue belt in Fig 3.1(a)). The $SrVO_3$ phase will become less stable for temperatures and $P(O_2)$, outside this region: $SrVO_3$ tends to over-oxidize (over-reduce) when T becomes lower (higher) or $P(O_2)$ becomes higher (lower).

The powder synthesis and pellet sintering steps were conducted in a tubular furnace with a flowing gas mixture containing hydrogen gas. During the reaction, hydrogen consumes residual oxygen near the sample through the water formation reaction, reducing oxygen partial pressure to a low level in order to drive the thermodynamic stability of $SrVO_3$. Based on this argument, one can estimate the required hydrogen concentration from the thermodynamic equilibrium of water formation reaction: $H_2+1/2O_2=H_2O$. Assuming that during synthesis and sintering the water formation reaction in the gas phase near the

sample is in equilibrium because of the high temperature (that is, the reaction is not significantly limited by kinetics), the following equation should be fulfilled:

$$K = \frac{P(\mathrm{H_2O})}{P(\mathrm{H_2}) \cdot P(\mathrm{O_2})^{\frac{1}{2}}} \qquad \text{Eq 3.1.1}$$

or

$$\log\big(P(\mathrm{H_2})\big) = \log\big(P(\mathrm{H_2O})\big) - \log(K) - 0.5\log\big(P(\mathrm{O_2})\big) \qquad \text{Eq 3.1.2}$$

where $P(\mathrm{X})$ stands for the partial pressure of the component X at equilibrium.

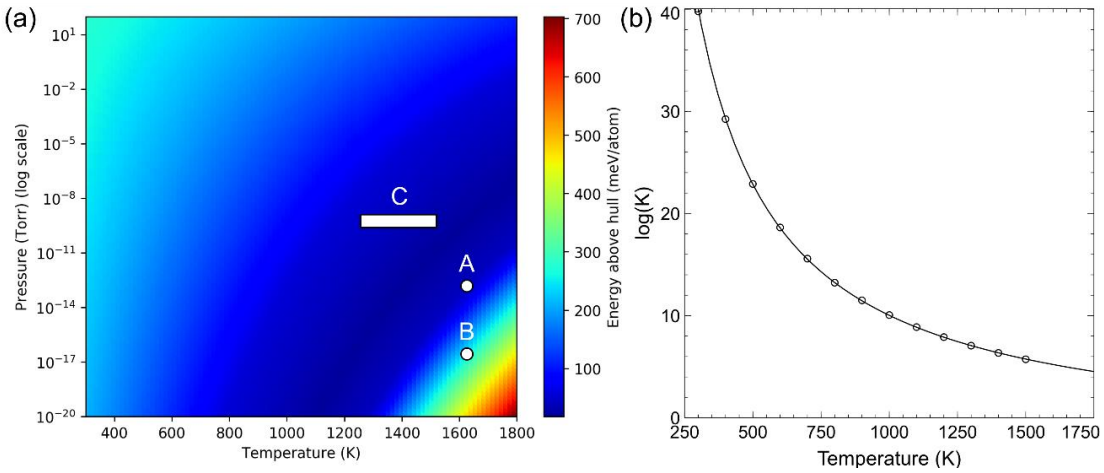

Fig 3.1. (a) Stability phase diagram of SrVO3 calculated through DFT (from Marks et al.[236]), with pellet sintering, over-reducing and emission testing conditions labeled as A, B and C, respectively. Reprinted figure with permission from Marks et al., *Phys. Rev. Mater. 5*, 83402, 2021. Copyright (2021) by the American Physical Society. (b) Plotted logarithm of the equilibrium constant of water formation reaction using values reported by Wagman et al.[237]. The original data set was up to 1500K, and the trend curve is the fitting result towards Van 't Hoff equation (Eq. 3.2).

Wagman et al. has reported the equilibrium constant K for this reaction between room temperature and 1500 K[237]. The results are plotted (in logarithmic form) in Fig 3.1(b). After fitting the data with the Van't Hoff equation[238]:

$$\log(K) = 2.303\left(\frac{\Delta S}{R} - \frac{\Delta H}{RT}\right) \quad \text{Eq 3.2}$$

The plot is extrapolated to the sintering temperature for the present work (1623 K), where the value of $\log(K)$ is estimated to be about 5.1.

The $P(O_2)$ range is estimated according to Fig 3.1(a). From previous studies correlating material synthesizability with DFT calculations of the energy above the convex hull, conditions for which the energy above the convex hull is less than approximately 50 meV/atom may reasonably be considered as stable[239,240]. At 1623 K, the $P(O_2)$ range corresponding to an energy above convex hull smaller than 50 meV/atom is between 4×10^{-17} atm and 4×10^{-7} atm. The $P(H_2O)$ estimation is based on the impurity level of the gases used in the experiments. The total gas pressure during sintering is about 1 atm. It is assumed here that the furnace is well-sealed, that negligible oxygen leaks into the furnace, and the residual oxygen mainly comes from the gases used here. According to Airgas (the gas supplier used for this work), the residual oxygen level of the gas mixture is 1 ppm. Since the equilibrium constant is much larger than 1, it could be assumed that almost all of the 1 ppm residual O_2 transfers to 2 ppm water vapor at equilibrium (note this *means at least 2 ppm of H_2 gas is needed* in order to consume up the residual oxygen). Also, the gases contain approximately 1 ppm of residual water vapor: therefore, $P(H_2O) \approx 3 \times 10^{-6}$ atm. If there are other oxygen sources, this value might be slightly higher.

Therefore, the estimated $\log\big(P(H_2)\big)$ range at equilibrium is between -2.4 and -7.4 (with atm as pressure unit), corresponding to a H_2 concentration range of 4×10^{-8} to 0.4%. Translating these values back to the purged H_2 gas concentration, the upper limit 0.4% value would not change since it is much larger than 2 ppm required to consume the residual

oxygen, while for the lower limit, since it is much smaller than the 2 ppm, the lower limit for the purged H_2 concentration needs to be 2 ppm (2×10^{-6}). The applied H_2 concentration for sintering, 0.05%, was just within this range and closer to the upper limit, which conservatively accommodated the possible existence of other oxygen sources, such as a small remaining leakage, or desorbed oxygen molecules from the furnace tube and flanges. It is noted that when the samples were cooling down at the end of sintering, the assumption of equilibrium might be no longer valid when the temperature was as low as a few hundred ℃, i.e., the water formation reaction was kinetically limited. This temperature might still be sufficiently high for $SrVO_3$'s oxidation, and the ~10^{-3} Torr $P(O_2)$ (corresponding to 1 ppm residue impurity level of the gas) is too oxidizing according to Figure 3.1(a). This likely attributed to the near-surface over-oxidation as observed in XPS (discussed below).

To intentionally make the sample slightly over-reduced, the pellets were kept at 1350 °C for an additional 1 hour, with the flowing gas switched to 5% H_2/95% N_2 for this step. This 5% H_2 concentration exceeded the upper limit of the stable window, which ensures an over-reducing environment. It is noted here that the choice of 5% H_2 balanced in N_2 as the reduction environment for this step is because exploratory experimentation and emission testing revealed that such an environment produced a much higher emission current compared to a H_2/Ar gas mixture. The reason for the improved performance obtained from 5% H_2 balanced in N_2 as the reduction environment over a H_2/Ar gas mixture remains unclear, and further study is needed to develop a better understanding of the impact of the ambient gas. After that, the samples were cleaved with a knife in the air to remove the over-reduced phase formed on the surface and expose the desired perovskite phase

beneath it. The samples were then rapidly placed into the ultrahigh-vacuum emission testing chamber, and an *in-situ* overnight annealing (at 1150 °C with 10^{-9} Torr $P(O_2)$) was processed right before the thermionic emission testing to preserve all low work function facets and terminations produced during these final processing steps.

The conditions corresponding to pellet sintering, intentional over-reduction and emission testing are also illustrated in Figure 3.1(a), labeled by A, B and C, respectively, indicating the pellet sintering and emission testing are processed within the stable window, while the intentional over-reducing condition is beyond the stable window.

Powder X-ray diffraction (XRD) was conducted using a Bruker D8 diffractometer with Cu Kα radiation (wavelength: 1.54 Å) to identify the phase information in sintered pellets. A Zeiss LEO 1530 was used for scanning electron microscopy (SEM) characterization of sample morphology. A Thermo Scientific K-Alpha X-ray photoelectron spectrometer (XPS) located at University of Wisconsin-Madison and a PHI 5000 VersaProbe III photoelectron spectrometer (UPS) located at University of Minnesota, Twin Cities, using Al Kα and He I radiation integrated with Ar^+ ion guns were used to measure the core level binding energies and work functions, to conduct Ar^+ ion sputtering with 3 keV ion energy for 60 seconds in each sputtering experiment, as well as post-sputter annealing experiment. All of the samples for XPS tests were transferred from the sintering furnace filled with reducing gas to the ultrahigh vacuum XPS chamber within 20 minutes to minimize the influence from possible oxidation, while the UPS was done in 2 days after the sample was taken out from the furnace due to required intercity travel. All the XPS characterizations were done using an X-ray beam with a 0.3 mm × 0.4 mm spot size, which corresponds to a lateral dimension comprising about 1.3 % of the sample surface. The UPS

spot size was about 1 cm in diameter, able to cover all the surface area. During work function measurements, the sample was biased to -29.7 V (with Thermo Scientific K-Alpha XPS) or -5.0 V (with PHI 5000 VersaProbe III UPS) in order to guarantee an overall negative applied field (see Secs 2.2.1.2 and 2.3.1), and the sample plate was perpendicularly aligned with the electron detector lenses at a distance of a millimeters[150,241]. The work function is extrapolated by subtracting the photoemission band width from the photon energy (1486.7 eV for Al Kα)[150,241]. Since the work function measurements are processed with negative sample biases, these biases have been removed when plotting the data for Figure 3.4(a). To process the post-sputtering heating, the sample was brought up to 700 °C with a bottom heater in PHI 5000 VersaProbe III instrument, and was kept for 0.5 h. The UPS spectra were collected both when the sample was at 700 °C and after it was cooled down to room temperature.

3.2.2 Thermionic emission testing

Thermionic emission tests were processed in UHV with a homemade electron-beam heater and anode fixture, as shown in Fig 3.2(a). The heater was modified from a W incandescent light bulb filament and driven by an adjustable AC voltage of 0 to 10 V, as shown in Fig 3.2 (b). The sample sit on a Mo sample holder positioned ~ 2 mm above the hot filament. There was a -750 V bias on the hot filament relative to the grounded Mo sample holder, directing an electron current to, and thus heating, the Mo platform and the sample to a desired temperature. In the initial experiments, some temperature nonuniformity across the sample was observed, where the center of the sample had a higher temperature than the edge. To eliminate the complications of such effect on interpreting the collected emission current, a small Mo ring with a 3 mm outer diameter, 2 mm inner

diameter and 0.025 mm thickness was placed on top of the sample, covering the cooler

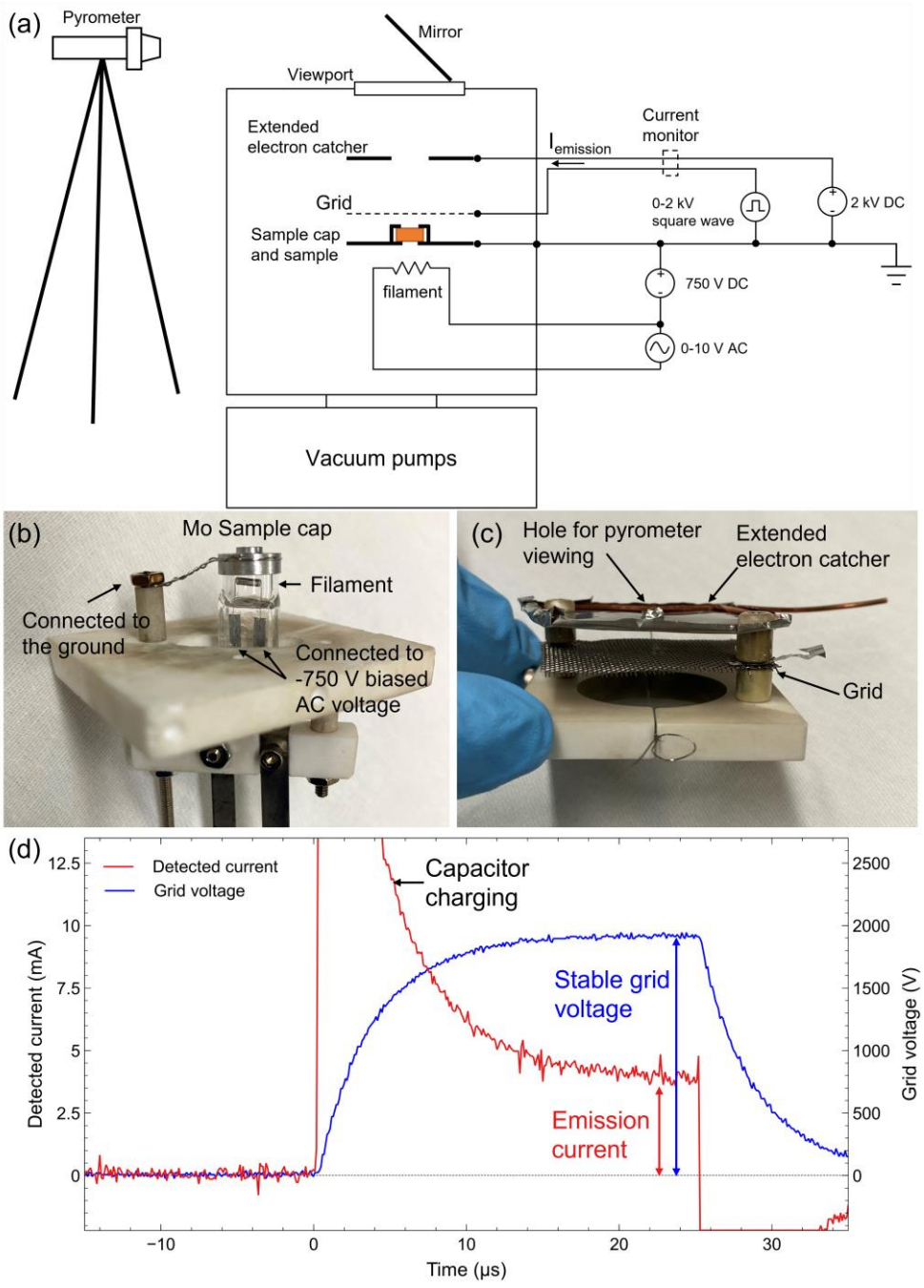

Fig 3.2. (a) Schematic diagram of thermionic emission testing fixture, chamber, circuit and optics for temperature measurement. (b) The photograph of the e-beam heater. (c) The photograph of the anode fixture. (d) A snapshot of one set of emission current and grid voltage data point. The large spikes in the emission current right after the pulse on and off are due to the capacitor charging and discharging. The non-zero current at a stable non-zero pulse bias on the grid is the actual measured emission current.

sample edge and reducing the emitting area from which current was collected and measured to an isothermal 2 mm diameter central area.

The anode fixture was designed for collecting the emitted current from the hot sample. It consisted of a grid, an extended electron catcher, as well as the ceramic holder and screws (shown in Fig 3.2(c)). The grid was a piece of monel-400 mesh (30 US mesh, with 0.56 mm square opening, 0.28 mm wire diameter and 45% transparency), and the extended electron catcher was a piece of Mo foil with a hole in the middle of it. During emission testing, the grid was sitting above the sample at a distance of ~2 mm (the exact distance depends on the sample thickness), and the extended catcher was placed at 6.35 mm above the grid, with its central hole directly above the sample. This grid-and-hole design enabled the direct observation and temperature measurement of the sample with a pyrometer.

In principle, one could directly bias the anode with a high DC voltage, and measure the DC current flowing through the anode, to get the emission current. In practice, however, this emission current, even if only a few milliamps, would significantly heat the grid and eventually melt it. To avoid this, the grid was connected to a high-voltage pulse generator, which creates a 25 μs-width square-wave pulse every 0.1 s, with a 0 to +2 kV tunable voltage. Meanwhile, the extended catcher was set to be at +2 kV constant bias, but the screening by the metal grid will make the sample only able to be affected by the grid voltage. Therefore, the emission would be enabled only when the pulse is activated, which significantly reduces the grid heating. This also means when calculating the electric field above the sample surface, one should divide the grid voltage by the sample-grid distance.

The extended catcher, on the other hand, collected the electrons that initially pass through the holes of the grid, to increase the measurement accuracy.

The use of low-duty-cycle pulse biasing makes it impossible to directly measure the emission current with a conventional ammeter because of the very low time-averaged values of the emission current. Instead, the sum of emission current on grid and catcher was measured with a current monitor made by Pearson Electronics which measures the voltage induced in its coil as a result of the time-varying magnetic field induced by the emission current pulse. The signal was input into a LeCroy WaveSurfer 44Xs 400 MHz oscilloscope, and the typical displayed wave shape is shown in Fig 3.2(d). In this figure, the large jumps in the detected signals after the start and the end of the pulse are due to the anode-cathode capacitor charging and discharging. After the pulse voltage becomes stable (corresponding to the last 5 μs of the pulse), the non-zero signal is the actual measured emission current, and the average value within this 5 μs is recorded, together with the stable pulse voltage. The current density was calculated by dividing this current with the 2 mm-diameter circular emission area.

The temperature was measured with an optical pyrometer from Leeds & Northrup, CO., by viewing the sample with a 655 nm red light filter through the grid, catcher hole, glass viewport, and a reflection mirror. To correct the brightness temperature T_b to the actual temperature T, the emissivity of the sample was assumed to be 1 (black body, which is a fairly good approximation for polycrystalline $SrVO_3$ samples), and the effect of the glass viewport and mirror was taken into account with a total effective emissivity of $\varepsilon = 0.7068$. Then, the actual temperature was calculated through Planck's law:

$$T = \frac{\mathrm{h}\nu}{\mathrm{k}_B} \frac{1}{\ln\left[1 + \varepsilon\left(\exp\left(\frac{\mathrm{h}\nu}{\mathrm{k}_B T_b}\right) - 1\right)\right]} \quad \text{Eq 3.3}$$

3.2.3 Surface energy calculations with DFT

(This section was primarily written by Dr Ryan Jacobs, with small modifications by Lin Lin)

All DFT calculations were performed using the Vienna *Ab Initio* Simulation Package (VASP) with a planewave basis set[242]. The projector augmented wave method[243] with Perdew-Burke-Ernzerhof-type pseudopotentials were used[244]. For all calculations, the planewave energy cutoff was set to 500 eV, spin polarization was enabled, and integration of the Brillouin zone was performed with the Monkhorst-Pack method[245]. The generalized gradient approximation (GGA) was used as the exchange-correlation functional. For materials containing V, the GGA+*U* method[246,247] was employed, with U=3.25 eV and J=0 eV following values in the Materials Project database[248]. In addition, the pseudopotentials and k-point grids for bulk materials also matched those employed in the Materials Project. Simulation cells were created using the pymatgen toolkit[249].

Here, numerous binary Sr-O, binary V-O, and ternary Sr-V-O bulk oxides were simulated to calculate the stable Sr and V chemical potentials at a given O chemical potential. The starting structures for these bulk materials were taken from the Materials Project database, and the Materials Project material ID number used for each material was indicated. For cases where multiple structural polymorphs of a given composition exist in the Materials Project database, the polymorph with the lowest calculated energy above the convex hull was selected, indicating it is likely to be the most stable polymorph, at least

based on DFT calculations. For Sr-containing materials, Sr metal (mp-1187073), SrO (mp-2472) and SrO_2 (mp-2697) were considered. For V-containing materials, V_2O_5 (mp-25279), VO_2 (mp-19094), V_2O_3 (mp-21579), VO (mp-19184), V_3O_5 (mp-1275946), V_7O_{13} (mp-27151), V_6O_{13} (mp-1094019), V_6O_{11} (mp-30518), V_8O_{15} (mp-556566), V_3O_7 (mp-622640), V_5O_9 (mp-542334), V_5O_{12} (mp-778252), and V_4O_7 (mp-555597) were considered. Note that V metal was not considered here due to incompatibility between GGA and GGA+U calculated energies. For Sr-V-O ternary materials, perovskite $SrVO_3$ (SVO113, mp-18717), $Sr_2V_2O_7$ (SVO227, mp-19368), $Sr_3V_2O_7$ (SVO327, mp-22391) and $Sr_3V_2O_8$ (SVO328, mp-19386) were considered. These ternary Sr-V-O materials comprise a reasonable set of stable ternary phases observed experimentally in the literatures[236,250–252].

For $SrVO_3$ surface slab calculations, a total of 15 different slab terminations were examined, belonging to (001)-, (011)-, and (111)-type orientations. The 1×1×1 bulk $SrVO_3$ perovskite cell (5 atoms) was used as a starting point for constructing the slabs. This bulk cell used an 8×8×8 k-point mesh, and simulation of each slab used appropriately scaled k-point densities based on this initial k-point mesh. For the (001)-oriented surface, symmetric slabs terminated with the native AO layer (SVO_001_AO), native BO_2 layer (SVO_001_BO2), an AO double layer (SVO_001_AO_double), an O vacancy on the AO surface (note this corresponds to 100% O vacancy concentration, yielding a purely Sr-terminated surface) (SVO_001_AO_Ovac), an O vacancy on the BO_2 surface (note this corresponds to 50% O vacancy concentration) (SVO_001_BO2_Ovac50), two O vacancies on the BO_2 surface (note this corresponds to 100% O vacancy concentration, yielding a purely V-terminated surface), and a mixed AO and BO_2 terminated surface with edge sizes of one unit cell wide (SVO_001_AO_BO2_1uc) and two unit cells wide

(SVO_001_AO_BO2_2uc). For the (011)-oriented surface, the native ABO-terminated surface (SVO_011_ABO) and the native O-terminated surface (SVO_011_O) were considered. For the (111)-oriented surface, the native AO_3-terminated surface (SVO_111_AO3) and the native B-terminated surface (SVO_111_B) were considered. Finally, two reconstructed surfaces based on the $\sqrt{2} \times \sqrt{2}$ (SVO_r2xr2) and $\sqrt{5} \times \sqrt{5}$ (SVO_r5xr5) reconstructions as observed on $SrTiO_3$ were also included [122]. Both reconstructions are based on (001)-oriented surfaces, with the $\sqrt{2} \times \sqrt{2}$ structure being BO_2-termination with a partial coverage of adsorbed O, and the $\sqrt{5} \times \sqrt{5}$ structure being BO_2-termination with adsorbed Sr. It should be noted that this set of $SrVO_3$ surfaces is by no means exhaustive and is meant to provide a qualitative account of the calculated $SrVO_3$ surface energies under a range of conditions. Therefore, the conclusions obtained from the present analysis as qualitatively useful for comparison with the experimental results and observations, but are not meant to provide an exhaustive, definitive assessment of the full scope of potential stable surfaces for $SrVO_3$.

3.3. Results

3.3.1 Phases and morphologies

The as-sintered bulk, polycrystalline $SrVO_3$ pellets exhibit a dark blue color, as shown in the inset photograph of Fig 3.3(a). Powder XRD results of $SrVO_3$ (Fig 3.3(a)) show a cubic perovskite lattice structure with space group $Pm\bar{3}m$, with peak positions in excellent agreement with the record retrieved from the XRD database. The absence of impurity peaks also suggests a high bulk phase purity (>99%), consistent with previous experimental studies.

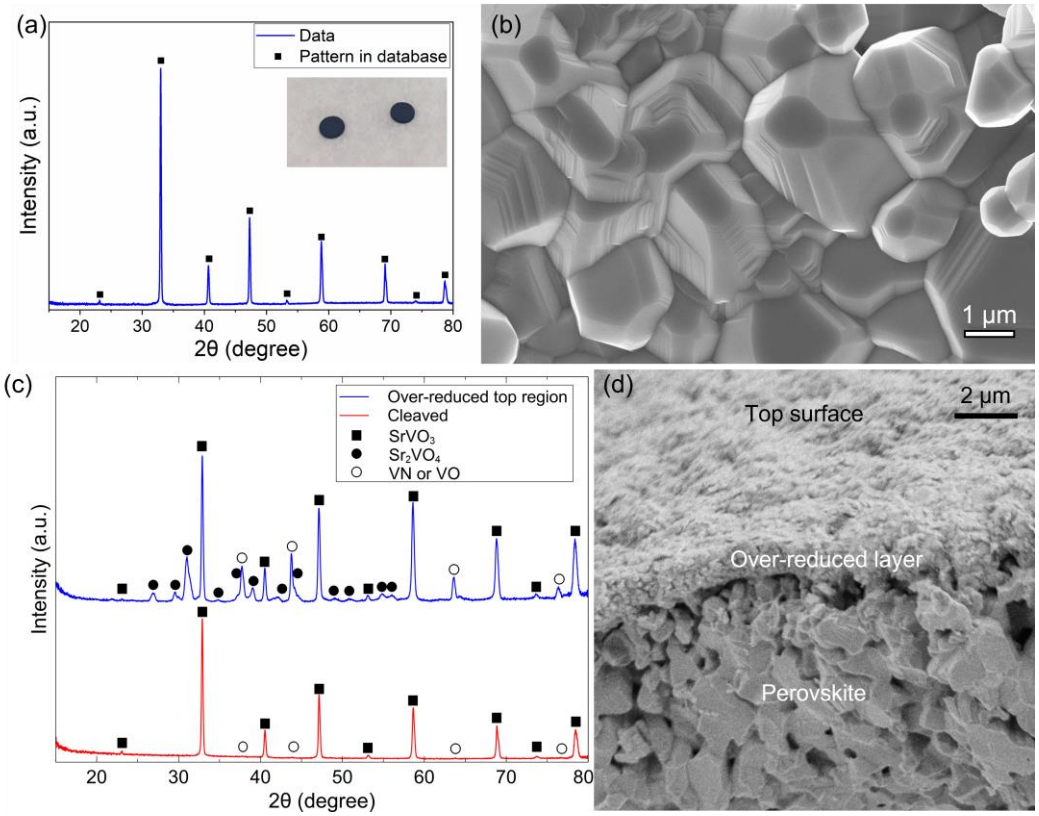

Fig 3.3. (a) Powder XRD data for polycrystalline $SrVO_3$ with retrieved record from database, showing a high phase purity. (b) Morphology of the sintered polycrystalline $SrVO_3$ pellet captured by SEM, suggesting the possible existence of (001) surfaces in comparison with Wulff shape predicted by DFT. The typical observed grain size is estimated to be between 0.5 to 2 μm. (c) XRD results for the top region of an over-reduced sample and the region beneath the top. The Top region contains perovskite $SrVO_3$, over-reduced phase Sr_2VO_4, as well as VN or VO. The region beneath contains mainly $SrVO_3$ with a very small amount of VN or VO. (d) SEM image of the top surface and cross-sectional profile of an over-reduced pellet, showing the over-reduced region serving as a capping layer on top of the perovskite beneath, with a thickness of ~1 μm.

The surface morphology of a representative sintered $SrVO_3$ pellet was characterized using SEM. As shown in Fig 3.3(b), the pellet surface is rough, consisting of distinct small grains, with a typical grain size between 0.5 to 2 μm. From Fig 3.3(b), some facets are square-shaped and have rectangular terraces, suggesting these facets belong to the {001} family of crystal orientations according to previous literatures[253] as well as DFT

surface energy calculations in Sec 3.3.4. Other facets are mainly hexagonal or triangular shaped, and are likely to be either (011)- or (111)-type surfaces[253].

For the samples experienced intentional over-reducing, an Sr_2VO_4 phase was formed on top of the pellet, as well as a phase that could be attributed to VN or VO, together with the perovskite $SrVO_3$ phase, as shown in Fig 3.3(c). Beneath such surface region, the major phase was still perovskite $SrVO_3$, with a negligible amount of VN or VO. Such heterostructure is clearly shown in the cross-sectional SEM image in Figure 3.3(d), which also suggests the thickness of this over-reduced region was about 1 μm. This surface over-reduced capping region likely prevents the gas molecule penetration and further oxidation on the perovskite phase beneath during furnace cooling down.

3.3.2 Surface composition and chemistry

To investigate the near-surface chemistry and composition of the $SrVO_3$ pellet surface, XPS core level scans and valence band scans were conducted, with the results shown in Fig 3.4. Note that the inelastic mean free path of the photoelectrons with photon energies ranging from 30 to 1500 eV is around 1 to 2 nm. Therefore, the XPS results discussed here should represent the properties of atoms and electrons within a 1-2 nm thick near-surface region of $SrVO_3$.

All Sr, V and O peaks were detected as the major components, with a small set of C 1s peaks showing up on the survey scan, as shown in Fig 3.4(a). The associated atomic percentages of each element are calculated using the Thermo Avantage software (the integrated data processing software of the XPS instrument), with Shirley-type background subtraction, yielding 17.0% of Sr, 13.9% of V, 60.4% of O and 8.7% of C within the near-

surface region. For an as-sintered pellet, the Sr:V atomic ratio is 1.3, suggesting the surface is slightly Sr-rich. Regarding carbon atoms, after a 15 second, 500 eV Ar^+ ion sputter etching (approximately corresponds to an etching depth of 0.7 nm), the carbon peak almost fully disappeared, suggesting carbon contamination is concentrated on the surface.

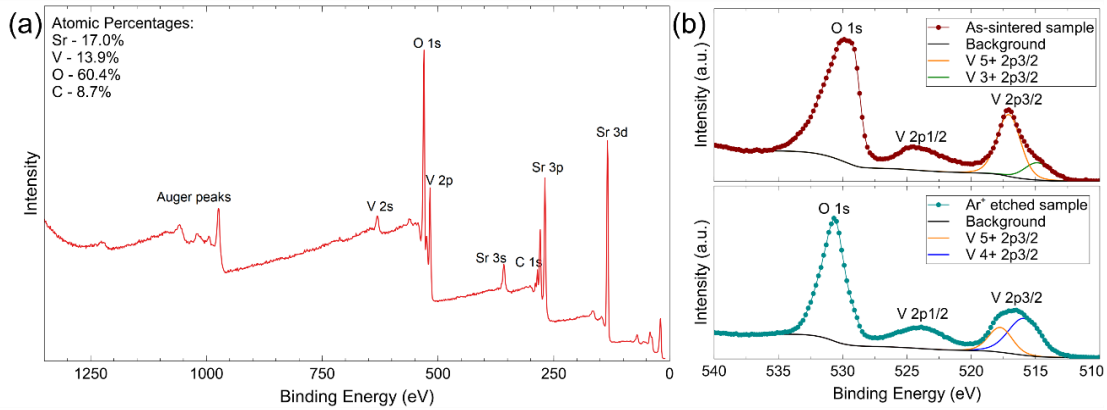

Fig 3.4. The XPS results of an $SrVO_3$ pellet. (a) The survey scan, with the corresponding atomic concentration summarized. (b) The vanadium core level scan before and after Ar^+ ion sputter-etching, with peak fitting processed by CasaXPS software, showing a predominantly V^{5+} component before etching and a majority of V^{4+} component after etching off the top few nanometers, suggesting that the over-oxidation is limited within the near-surface region.

The chemical states were also studied via XPS by zoomed-in scans on the core level of each element and proper peak fitting processed with CasaXPS sofware, with the results shown in Fig 3.4(b). The most consequential information of this scan comes from the vanadium 2p3/2 scan. The peak is centered at a binding energy of 517.4 eV, with only a weakly asymmetric shoulder on the lower binding energy side, suggesting the surface vanadium was predominantly in an over-oxidized V^{5+} state, rather than the nominal 4+ state associated with the bulk $SrVO_3$ phase. Conducting a detailed peak fit using a Shirley background, the vanadium 2p3/2 peak decomposed into a V^{5+} and another reduced (likely V^{3+}) component. The V^{5+} and the reduced components roughly constituted 76% and 24% of the total peak intensity, respectively.

The over-oxidized near surface layer of $SrVO_3$ was removable by Ar^+ ion sputter-etching. As shown in Fig 3.4(c), after etching off a ~5 nm thick near-surface region with a 3 keV ion beam for 30 seconds, the vanadium 2p3/2 peak was attributable to V^{5+} and V^{4+} components, with ratios of 33% and 67%, respectively. This suggests that the vanadium atoms buried in the bulk crystal predominantly have the nominal V^{4+} oxidation state. The remaining small (33%) component of V^{5+} after ion etching is likely due to V^{4+} oxidation by residual oxygen molecules in the XPS chamber, as well as V^{5+} from the as-sintered surface that was not removed due to uneven etching of the surface.

3.3.3 Work function measurements and thermionic emission testing

As mentioned in Sec 2.3.1, the use of photoemission (UPS or XPS) is the standard approach to study the work function of a surface, but the results is likely influenced by the complex surface chemistry, and only provides the observed work function with patch field effect. It does not directly reveal the individual local work functions of microscale patches comprising the $SrVO_3$ surface.

Photoemission-based work function measurements were first performed on as-sintered pellets. The XPS measured work function on a sample with 20 min air exposure is 3.6 eV, and the UPS measured value on a sample with 2 days of air exposure is 3.45 eV (this time difference is caused by intercity travelling for UPS experiment off campus), indicated by the secondary electron cutoff spectra (the UPS spectrum is shown in Figure 3(a) after bias correction). The two values agree with each other within the XPS measurement error. The UPS-measured sample was then sputter-etched with Ar^+ ion and annealed *in-situ* at 700 °C for 30 min to heal any surface modification by the Ar^+ ion beam. After this step, the work functions of the sample were measured again with UPS at both

700 ˚C and after cooling down to room temperature. This time, the results were 4.06 and 4.07 eV (shown in Fig 3.5(a)), respectively. The disagreement between these values and the 1.9 eV DFT prediction is attributed to complex surface chemistry and the patch field effect, which will be further discussed in Secs 3.4.1 and 3.4.2.

The samples were then tested by thermionic emission, which provides a direct evaluation of the applicability of a new material like $SrVO_3$ as a thermionic emitter. After the over-reduced top region being cleaved off, the samples were immediately placed into the emission testing chamber subsequently heated to 1150 °C in UHV (10^{-9} Torr) overnight to burn out any contamination from air exposure, as well as to convert any over-oxidation of the near-surface region into the correct perovskite phase and drive formation of the Sr-

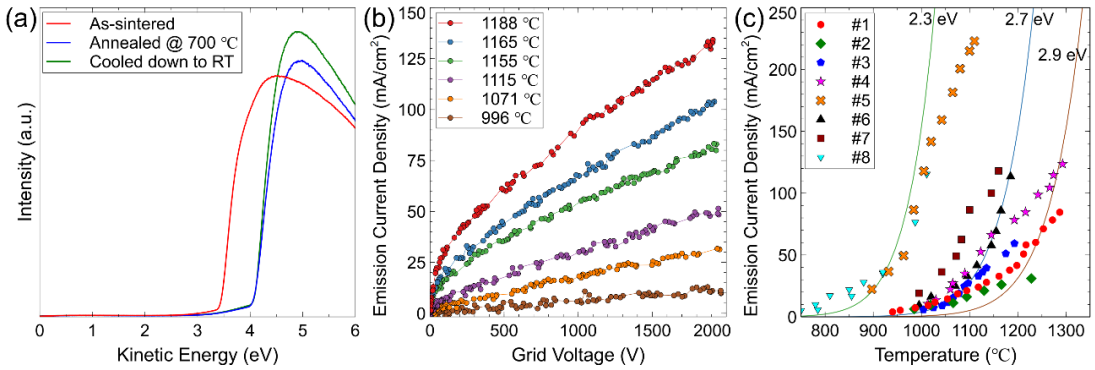

Fig 3.5. The work function measurement and thermionic emission test results on $SrVO_3$ pellets. (a) The UPS measured bias-corrected secondary electron cutoffs on an as-sintered pellet, and a pellet after Ar^+ ion sputter-etching plus annealing at 700 ˚C for 0.5 h, and after cooling down, suggesting 3.45, 4.06, and 4.07 eV, respectively. It is not unexpected that these values do not match the DFT prediction due to surface contamination and patch field effect. (b) The thermionic emission *J-V* plots from an over-reduced and cleaved sample at different temperatures, suggesting an increasing emission current as A-K voltage becomes larger, consistent with the patch field effect. (c) The thermionic emission *J-T* plots of several over-reduced-and-cleaved samples within the temperature-limited regime, with datasets #1 to #7 collected at 1.5 kV A-K voltage, and the A-K voltage of #8 unknown. These datasets indicate an *effective* 2.7 eV work function under the testing condition together with a few samples showing an *effective* work function close to 2.3 eV.

terminated surface. The emission current density data were then collected over a temperature range between 750 ℃ and 1300 ℃, with the grid-to-sample (anode-cathode, abbreviated as A-K) voltage ranging from 0 to 2 kV. The dependence of the emission current density J on the A-K voltage V and the sample temperature T has been plotted as Figs 3.5(b) and 3.5(c), respectively.

From Fig 3.5(b) a strong J-V dependence is immediately observable, which is not the typical case for a thermionic emission cathode under such high applied A-K voltage (known as the temperature-limited (TL) regime). This strong dependence of the current density on the A-K voltage is believed to be the direct consequence of the patch field effect existing on the heterogeneous surfaces of the polycrystalline samples.

For J-T relationship and work function extrapolation, several tests on different samples were conducted, with the results plotted in Fig 3.5(c). The *effective* work functions for all the datapoints were extracted using the RLD Eq 2.3[171,180] with setting the Richardson constant A to the theoretical value of $A_0 = 4\pi m_e e k^2/h^3 = 120$ A·(cm·K)$^{-2}$ (see discussions in Sec 2.3.3). The mean and standard deviation of the extracted work functions for all the data in each dataset were then calculated to show the effective work function of the corresponding sample and summarized in Table 3.1. The datasets in Fig 3.5(c) from different samples (except #5 and #8) show an average ~2.7 eV effective work function at 1.5 kV A-K voltage within the testing temperature range, with an observed spread of about ± 0.2 eV. Moreover, datasets #5 and #8 show significantly higher emission current densities, suggesting a ~2.3 eV effective work function. The fitting and interpretation of effective work function, as well as the variability between samples are further discussed in Section 3.4.2.

Table 3.1. Extrapolated effective work function values for all the datasets, with means and standard deviations collected.

Sample	#1	#2	#3	#4	#5	#6	#7	#8
Mean of the effective work function (eV).	2.7653	2.7657	2.7169	2.7407	2.3745	2.6678	2.5814	2.2342
Standard deviation of the effective work function (eV).	0.1261	0.1170	0.0386	0.1121	0.0604	0.0487	0.0471	0.0897

Additionally, to examine the durability of the $SrVO_3$ thermionic emitters, one sample has been repeatedly testing by cooling-heating for several times. In a typical set of such experiment, a sample was first properly treated as discussed in Section 3.2.1 with

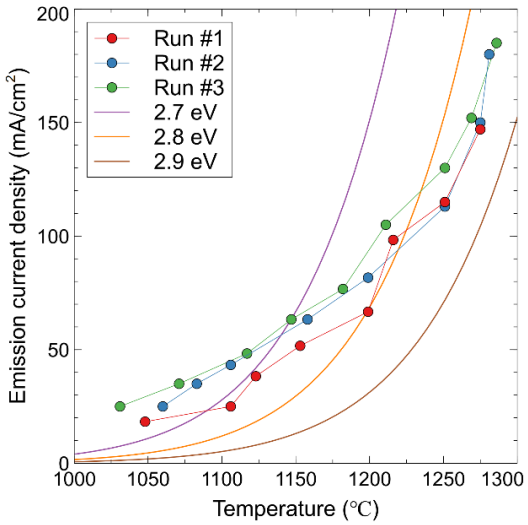

Fig 3.6. The reproducibility testing of a $SrVO_3$ thermionic emitter sample. The sample was heated up and tested for 3 cycles, labelled as Runs #1, #2 and #3. The theoretical RLD equations with 2.7, 2.8 and 2.9 eV work functions are also plotted for reference.

intentional over-reducing, cleaving and overnight in-situ annealing. The sample was then heated up to ~1300 ℃ and gradually cooled down in a couple of hours, with the thermionic emission current and temperature being recorded during this cooling procedure. Following that, the sample was again heated up to ~1300 ℃, cooled down and tested for 3 cycles. The data are shown in Fig 3.6, and the good reproducibility suggests relatively good durability when cycling the $SrVO_3$ samples up and down in temperature.

3.3.4 DFT verification on morphology and surface composition

To further understand the expected stability of various orientations and terminations of perovskite $SrVO_3$ surfaces under different conditions of synthesis and testing, their surface energies were studied using DFT calculations. Assessing the stability of different $SrVO_3$ surfaces under a given oxygen chemical potential μ_O (set by the temperature and partial pressure of oxygen) requires setting a Sr chemical potential μ_{Sr} and V chemical potential μ_V. These values both have certain possible ranges consistent with the source of Sr (V) being either the most stable Sr binary oxide (Sr-V-O ternary oxide) at a given μ_O, which coincides with Sr-rich conditions, or the most stable V binary oxide (Sr-V-O ternary oxide) at a given μ_O, which coincides with V-rich conditions. To provide a small number of specific guiding values, the standard approach of considering limiting cases was followed, specifically the Sr-rich and V-rich conditions[137,254]. It is expected that the Sr-rich limit is more representative of the experimental polycrystalline samples than the V-rich limit. This conclusion is based on both the $SrVO_3$ XPS atomic ratio observations (Sec 3.3.2) and previous studies on perovskites suggesting significant A-site element segregation onto the surface[255,256]. The plots of calculated surface energy as a function of

μ_0 for the Sr-rich limit for all 15 $SrVO_3$ surfaces considered here, as well as the corresponding Wulff construction shape at equilibrium, have been summarized in Fig 3.7.

In the surface energy plot under the Sr-rich limit (Fig 3.7(a)), the vertical blue dashed lines denote the approximate μ_0 values of the experimental $SrVO_3$ processing condition (T~1600 K, $P(O_2)$ ~10^{-12} Torr), the thermionic emission testing condition (T~1300 K, $P(O_2)$ ~10^{-9} Torr), the XPS/UPS characterization condition (T~298 K, $P(O_2)$ ~10^{-8} Torr), and the room condition (T ~298 K, $P(O_2)$ ~160 Torr (normal air)). The set of most stable $SrVO_3$ surfaces was observed to changes with μ_0. One aspect of most interests is the stability of the (001) SrO-terminated surface (SVO_001_AO) as available evidence indicates that this is the lowest work function surface of $SrVO_3$. Therefore, realizing some portion of the cathode with this low work function surface is likely key to enhancing its emission performance. The results of Fig 3.7(a) show that at the room condition, this termination is not stable. Instead, for the (001) orientation, the BO_2-terminated surface with adsorbed oxygen adatoms (SVO_001_BO2_Oads) is the most stable surface. However, as the value of μ_0 is lowered and more reducing conditions are realized, the stability of the (001) AO surface is enhanced. Under the processing condition for sintering $SrVO_3$ pellets, the (001) AO surface is the most stable surface. The analysis indicates at these processing conditions the Wulff construction predicts that up to about 80% of an equilibrium $SrVO_3$ particle may be populated with the (001) SrO surface. However, in practice, due to fluctuations and kinetic limitations it is easy to observe less than 80% coverage of the (001) AO surface under these conditions. Under the emission condition, the (001) AO surface is not the most stable surface. Instead, the (111) AO_3 surface is the most stable surface. However, the (001) SrO surface is competitive in stability with the (111) AO_3 surface, and

it is still present with a significant ratio of 30% in the Wulff construction in the Sr-rich limit. The surface area fractions predicted by the Wulff construction for the different conditions are summarized in Table 3.2, and the Wulff construction shape of the thermionic emission testing condition under the Sr-rich limit are shown in Fig 3.7(b).

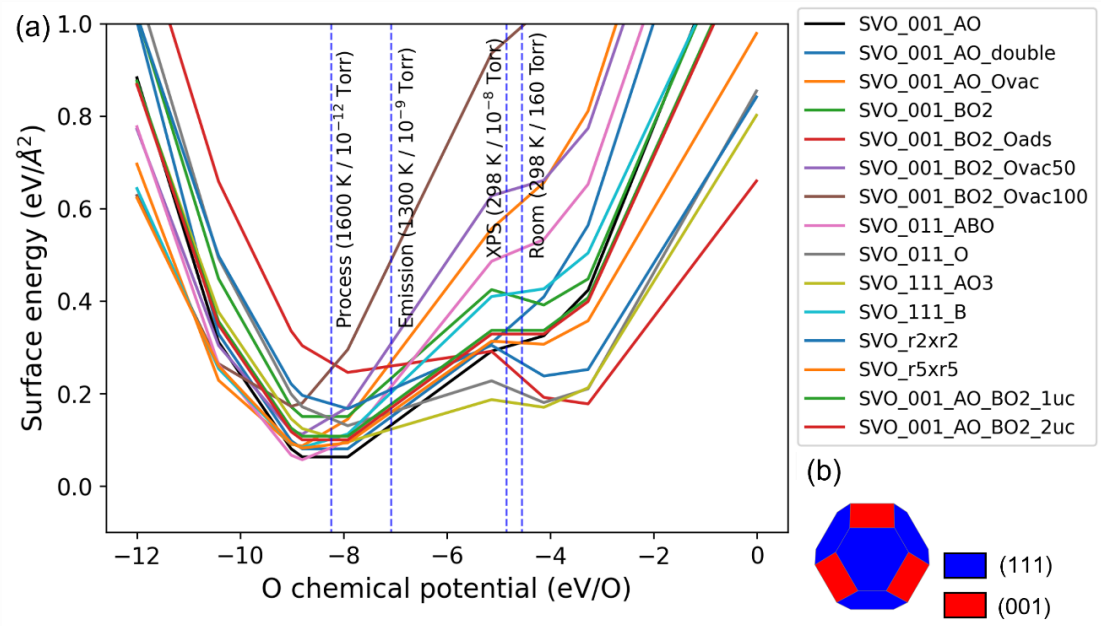

Fig 3.7. (a) Plots of the calculated $SrVO_3$ slab surface energies for various surfaces under Sr-rich limit. The vertical blue dashed lines denote approximate O chemical potential values representative of the experimental $SrVO_3$ processing condition, thermionic emission test condition, XPS characterization condition, and room condition. The detailed structures of these surfaces are introduced in Section 5. (b) The calculated Wulff construction shapes under the Sr-rich limit considering the lowest energy (001)-, (011)-, and (111)-oriented surface terminations under thermionic emission condition. The red and blue colors denote (001) and (111) surface facets, respectively. Legend description: SVO_001_AO: native AO layer, SVO_001_BO2: native BO_2 layer, SVO_001_AO_double: AO double layer, SVO_001_AO_Ovac: AO surface + O vacancy, SVO_001_BO2_Ovac50: BO_2 surface + O vacancy, SVO_001_BO2_Ovac100: BO_2 surface + two O vacancies, SVO_001_AO_BO2_1uc: mixed AO and BO2 1 unit cell wide, SVO_001_AO_BO2_2uc; mixed AO and BO2 2 unit cells wide. SVO_011_ABO: native ABO-terminated surface, SVO_011_O: native O-terminated surface. SVO_111_AO3: native AO_3-terminated surface, SVO_111_B: native B-terminated surface, SVO_r2xr2: (001) $\sqrt{2} \times \sqrt{2}$ reconstruction, SVO_r5xr5: (001) $\sqrt{5} \times \sqrt{5}$ reconstruction.

Table 3.2. Summary of Wulff construction equilibria calculated surface area fractions for Sr-rich limit, and the most stable surface terminations present under process, thermionic emission, and room conditions when considering the most stable (001)-, (011)- and (111)-based surfaces at each condition.

Sr-rich limit		
Condition	*Orientations and Area fractions*	*Surface terminations present*
Room	(0, 0, 1): 0.090	SVO_001_BO2_Oads
	(0, 1, 1): 0.259	SVO_011_O
	(1, 1, 1): 0.650	SVO_111_AO3
Emission	(0, 0, 1): 0.306	SVO_001_AO
	(0, 1, 1): 0.0	SVO_011_O
	(1, 1, 1): 0.694	SVO_111_AO3
Process	(0, 0, 1): 0.811	SVO_001_AO
	(0, 1, 1): 0.189	SVO_011_ABO
	(1, 1, 1): 0.0	SVO_111_B

3.4 Discussion

As mentioned in the introduction, there are two key issues existing on $SrVO_3$ for thermionic emission applications, namely the metastability of the material and the patch field effect induced by surface heterogeneity. These issues are critical for interpretating the experimental results and understanding the interesting physics and chemistry behind them.

3.4.1 Bulk and surface stability, morphology and surface termination.

Vanadium can exist in numerous oxidation states, with the most common oxidation states for vanadium-based oxides being 2+, 3+, 4+ and 5+. As a result, the Sr-V-O ternary

alloy has numerous possible stable compounds depending on the temperature and $P(O_2)$[257]. Previous DFT calculations on bulk phase $SrVO_3$ suggested the existence of a "stable window" of temperature and oxygen partial pressures where $SrVO_3$ is expected to be most easily synthesizable, although not the true ground state (see Sec 3.2.1 and Fig 3.1(a)). The synthesis, sintering and emission testing conditions in this work were carefully selected to be within the stable window. The correct bulk phase from the XRD results (Fig 3.2(a)) suggests that $SrVO_3$ is synthesizable within such window (i.e., 1350 ℃ and 0.05% H_2 concentration at 1 atm total pressure). Even within this processing window, bulk $SrVO_3$ is formally metastable and its formation depends on starting with precursors that favor its formation kinetically. Therefore, it is reasonable to expect that $SrVO_3$ may easily oxidize to more thermodynamically stable phases such as $Sr_3V_2O_8$ or $Sr_2V_2O_7$. When moving outside the optimum processing window, $SrVO_3$ will become increasingly thermodynamically unstable, and will have a tendency to oxidize (reduce) when T goes lower (higher) or $P(O_2)$ goes higher (lower). However, these tendencies, especially the over-oxidation at lower temperature, is likely often kinetically limited to the near-surface region, which is supported by the XRD measurements which suggest a high bulk phase purity over the relatively large X-ray penetration depth of ~0.1 to 1 μm.

In addition to the bulk metastability, $SrVO_3$ also exhibits complex surface chemistry. As suggested by XPS composition analysis, there was a significant amount of carbon on the surface, which were attributed to CO_2 and organic molecule adsorption (and possible carbonate formation) during sample transfer from the furnace to the XPS chamber. The fact that this carbon was removed by Ar^+ ion etching of the top 0.7 nm verified that it was localized to the surface. Furthermore, the fact that the surface vanadium of an as-

sintered sample was predominantly V^{5+} suggests that the near-surface region with a depth of ~5 nm was likely over-oxidized. Such oxidation was assumed to happen during cooling down after sintering, when the water formation reaction could have been kinetically inhibited, enabling the sample to react with residual oxygen and cause such over-oxidation within the top few nms. Additional oxygen adsorption and reaction was possible during transfer of the sample from the furnace to the XPS chamber. However, such a reaction is expected to be limited to the top few atomic layers due to kinetic limitations at room temperature. The fact that the nominal V^{4+} component became predominant after ~5 nm etching indicates that the oxidation was limited to the near-surface region of a few nm, acting to form a thin passivation layer that prevented further oxidation in the bulk. This conclusion agrees with the XRD results that suggest a high bulk $SrVO_3$ phase purity.

The XPS and UPS work functions of the as-sintered pellet were 3.6 eV and 3.45 eV. This measurement is for a polycrystalline material with somewhat uncontrolled surface orientations and terminations. Furthermore, given surface C contamination and over-oxidation, the work function of an as-sintered pellet is not likely to match any values derived from DFT predictions of clean surfaces. The deviation from a well-defined ideal surface could significantly alter the surface dipole and affect the local work function by up to several eV. Therefore, the absence of any obvious connection between the as-sintered pellet work function values of ~ 3.5 eV and the DFT-predicted low work function value of 1.9 eV for SrO terminated (001) $SrVO_3$ is not surprising. To have any hope of seeing a connection between the photoemission work functions and the low work function DFT predictions, it was necessary to obtain surfaces more representative of pure $SrVO_3$ under conditions that favor formation of SrO terminated (001). One simple approach was to apply

sputtering and annealing, which successfully removed C and reduced the amount of V^{5+} and yielded a work function of 4.06-4.07 eV. While this value is presumably more representative of $SrVO_3$ surfaces, it is still far from the DFT predicted low work function value of 1.9 eV for SrO terminated (001) $SrVO_3$. A primary reason for this is patch field effect, and it is also possible that the sputtering approach was not fully optimized to produce the SrO terminated (001) surfaces. Therefore, further optimization of the surfaces and thermionic emission approaches were explored to observe the low work functions in systems with large patch fields.

To increase the amount of pure $SrVO_3$ surfaces, and in particular SrO terminated (001) surfaces, one intentional over-reducing step was added, with details introduced in Sec 3.2.1. This resulted in a greyish-colored layer of Sr_2VO_4 and VO or VN covering the top of the pellet, which was easily distinguishable from the dark-blue perovskite both by the naked eye and with XRD (see Fig 3.3(c)). As suggested by the cross-sectional SEM image (Fig 3.3(d)), this 1-μm-thick over-reduced region served as a capping layer that protected the perovskite phase underneath from over-oxidation as the sample cooled.

Prior to thermionic emission testing, this capping layer was cleaved off with a knife to expose the dark-blue perovskite region, and the sample was rapidly placed in the vacuum chamber for emission testing (total air exposure ≈20 min). As discussed above, the freshly-exposed surface was expected to also adsorb carbon- and oxygen-containing molecules from the air, but such adsorption and oxidation will likely only occur within the top few atomic layers, compared to the direct furnace-cooled sample with a deeper over-oxidized region of a few nanometers. The *in situ* annealing step right before thermionic emission testing is speculated to have enabled (1) the desorption of surface contaminants like

adsorbed CO_2 and H_2O, (2) conversion of the shallow, over-oxidized surface to the correct phase, as well as (3) enrichment of the surface by Sr, all to achieve a significant fraction of (001) SrO-terminated low work function patches on the surface.

Complex oxides like perovskite $SrVO_3$ can consist of multiple surface orientations, terminations and possible reconstructions, and many of them may have comparable surface energies. As a result, even for a sample with perovskite phase throughout the surface, the exact surface structure might still be complex. As suggested by the surface energy and Wulff shape construction calculations (see Sec 3.3.4), there are a handful of surface terminations that are thermodynamically competitively favorable under the processing and thermionic emission testing conditions. This prediction is consistent with the samples' rough surface morphologies observed with SEM. On the other hand, qualitative visual observations from SEM (cf. Fig 3.3(b)) suggest there is a non-negligible fraction of the whole pellet surface which has (001)-type surface orientations and this is also consistent with thesurface energy calculations (cf. Fig 3.7(a)). Given the Sr-rich limit suggested by XPS measurements and other studies on perovskites suggesting a general A-site segregation trend[255,256,258], it is reasonable to expect that a significant fraction of the surface contains low-surface-energy (001) SrO-terminated surfaces, which is the low work function surface desirable for thermionic emission applications. Given the above considerations, it is reasonable to expect that the sample synthesis and preparation approach outlined above produced a material with significant area fractions of SrO terminated (001) $SrVO_3$. It is worth noting that even for (001) surfaces that are well annealed under conditions that stabilize SrO-termination, it is unlikely that a perfect SrO termination is formed on the entire surface. Thermal fluctuations and incomplete

equilibration are expected to lead to some regions of VO_2 termination, or other reconstructions not considered in the present analysis. As will be discussed in Sec 3.4.2, even a modest area fraction of VO_2 patches could significantly increase the effective work function of the (001) surface. But the overall significant amount of (001) SrO terminated would still be existing on the surface.

Therefore, it should be possible to measure the low work function of this surface with a probe that could provide *in situ* measurement as well as overcome the patch field effect. Here this low work function was probed with thermionic emission, and it provides at least an approximate approach to the ideal probe for measuring the SVO low work function surfaces.

3.4.2 Patch field, work function interpretation and emission behavior

In addition to the complex surface chemistry, the patch field effect discussed in Sec 2.2.1.3 also significantly impacts the vacuum level profile and electron emission behavior above a heterogeneous surface[1,8,9] and is a key consideration for understanding measurements on the polycrystalline $SrVO_3$ work function and emission properties.

In Sec 3.4.1, it is mentioned that the UPS work function from an *in-situ* sputter-etched and annealed sample is 4.1 eV, still much higher than DFT predicted 1.9 eV. Such discrepancy could be attributed to the patch field effect that prevents the measurement of the lowest local work functions on heterogeneous $SrVO_3$ surfaces under weak applied field of ~0.5 V/mm in the UPS experiment (Note the SI unit for electric field is V/m as discussed in Chapter 2, but it is more convenient to use V/mm in the perovskite experiments, so V/mm is selected to be the unit of electric fields in Chapters 3 and 4). From DFT predictions,

the work functions among different surface orientations and terminations range from 1.9 to 7.2 eV[67]. Therefore, it is reasonable to assume that the surface consists of micron-sized (or smaller) patches with work function differences of several eV. After inserting Φ_L=1.9, Φ_H=7.2 eV and $\sqrt{S}$ =1 μm (the typical facet length scale from SEM in Fig 3.3(b)) into critical field Eq 2.12.2 introduced in Sec 2.2.1.3, the critical field for cancelling the patch field would be on the order of a few kV/mm (or greater). This is a very approximate qualitative guide, but it does suggest fields on the scale of kV/mm is needed to overcome the patch field effect. This critical field is much larger than the applied fields in photoemission work function experiments, which implies that only the surface area-weighted average work function should be detectable in such studies. The ~4.1 eV UPS work function falls near the center of the DFT range (which is 4.55 eV[67]), and is thus a very plausible average of the surface local work functions, despite the much simplified model utilized.

To further investigate whether low work function surfaces exist on the $SrVO_3$ samples with relatively strong patch fields, one must conduct either local measurements on the surface e.g., KPFM, or electron emission experiments under relatively high electric fields[1]. Given the fact that most KPFM instruments conduct measurements in air, they could not be used because of the tendency of the $SrVO_3$ surface to oxidize. Therefore, *in situ* thermionic electron emission measurements under moderately high electric field were conducted on these $SrVO_3$ samples.

For an ideal material with a single work function Φ on a homogeneous emitting surface, the thermionic emission behavior can be categorized into two regimes. One is a temperature-limited (TL) emission regime, where the A-K bias is high and the temperature

is relatively low. In this case, the thermionic emission current density should be governed by the RLD Eq 2.3, and not directly depend on the applied voltage or A-K distance except the small Schottky surface barrier lowering (Eq 2.11). The other case is called the full-space-charge-limited (FSCL) regime at high temperature and low applied A-K voltage, where the emission current density is only a function of A-K voltage V and A-K distance d predicted by Child-Langmuir law, and is independent of the temperature.

$$J_{FSCL} = \frac{4\varepsilon_0}{9}\sqrt{\frac{2e}{m_e}}\frac{V^{\frac{3}{2}}}{d^2} \qquad \text{Eq 3.4}$$

Given the high applied voltage and short A-K distance in the experiment, the samples emitted within the TL regime when the A-K voltage exceeded ~100 V, which was the case for the majority of the data (see Fig 3.8(a)). While this framework is a simplified

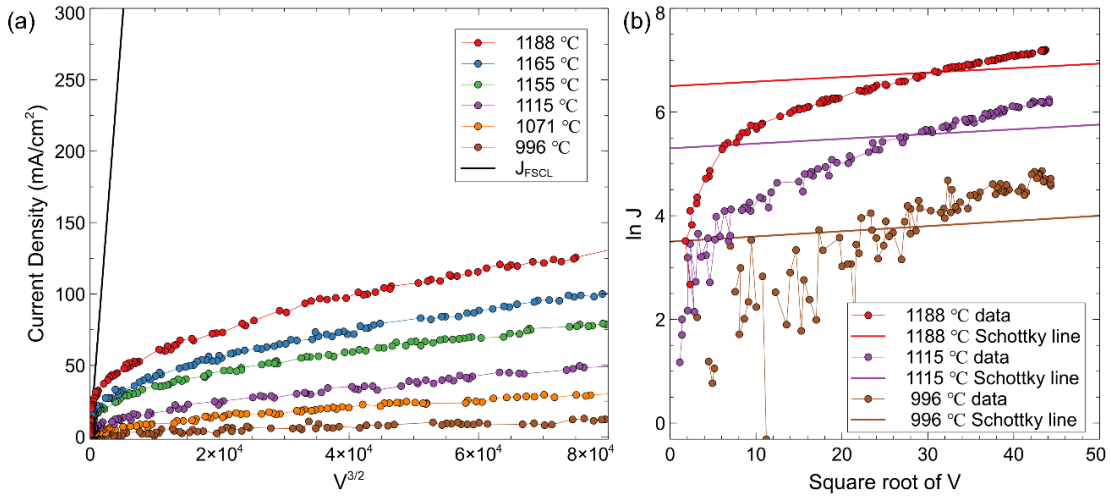

Fig 3.8. (a) Comparison between $SrVO_3$'s emission current density and FSCL current density, suggesting the emission is mainly temperature-limited because J_{FSCL} is much higher than the emission data, and the data curves deviate from any straight $V^{3/2}$ lines. (b) Comparison between the ln$J$ vs $\sqrt{V}$ slopes of $SrVO_3$ and Schottky slopes with the same corresponding temperatures, showing that the Schottky slopes are much smaller than those of $SrVO_3$.

representation of the samples and experimental conditions[111], it is still useful for qualitative guidance.

The J-V relationships shown in Figure 3.5(b) suggests that the TL emission current density J has a strong (increasing) variation with increasing A-K voltage V, in contradiction to the RLD Eq 2.3. It might be argued that such J-V dependence is due to the Schottky effect (Eq 2.11)[1,25]. However, as discussed in Sec 2.2.1.2, only when the applied field is more than 10^5 V/mm would the regular Schottky effect play a significant, which is more than 2 orders of magnitude stronger than the field applied in thermionic emission. The conclusion that such J-V dependence is not from the Schottky effect can be further verified the Schottky slope approach. By combining RLD Eq 2.3 Schottky effect Eq 2.11, it is straightforward to derive that for an ideal single-work-function cathode, there should be a linear relationship between $\ln J$ and $\sqrt{V}$:

$$\ln J = C + \frac{1}{kT}\sqrt{\frac{e^3}{4\pi\varepsilon_0 d}}\sqrt{V} \qquad \text{Eq 3.5}$$

where C is a constant[7]. The straight lines at various temperatures suggested by Eq 3.5 are known as Schottky lines, with slopes equal to $\sqrt{e^3}/\left(kT\sqrt{4\pi\varepsilon_0 d}\right)$. Then, comparing the slopes of $\ln J$ vs $\sqrt{V}$ plots and the ideal Schottky line slopes could tell if the J-V dependence is pure Schottky effect. For the $SrVO_3$ data plotted in Fig 3.8(b), the more than 1 order of magnitude larger slopes than the ideal Schottky cases indicate a much stronger J-V dependence than Schottky effect predicted in Eq 2.11. This strong the J-V dependence is sometimes called the *anomalous* Schottky effect[259], and it is generally understood to occur due to patch field predictions. With patch fields, the effective work function decreases as

the applied electric field increases, resulting in an increasing emission current. In the *J-V* curves of Figure 3.5(b), the emission current density still exhibits a strong increase with A-K voltage even at 2 kV, which was the highest allowed voltage of the experimental setup and corresponds to a ~1 kV/mm local electric field. This trend observed in Figure 3.5(b) indicates that the effective work function should further decrease with further increase in the applied field, closer to the estimated critical field, in agreement with patch field theory.

Next, the *J-T* dependence (also known as a Miram curve[3,260]) plotted at 1.5 kV A-K bias was investigated to understand the work function of $SrVO_3$. As discussed in Sec 2.3.3, in order to avoid the low-Φ-low-*A* fitting problem, the "*effective work function*" approach described by Hensley[180] was employed to identify Φ values directly from RLD Eq 2.3 with the theoretical $A_0 = 120\ \mathrm{A{\cdot}(cm{\cdot}K)^{-2}}$ value[34]. This simple RLD model is believed to still capture the majority of the emission physics from the metallic $SrVO_3$. Meanwhile, the use of theoretical *A* will also provide a standardized evaluation protocol to compare with other thermionic emitters. Such standardization may reduce claims of materials functioning as a "good emitter" only because of its low work function, with the fact of low emission current density being neglected. The use of this approach yields a typical 2.7 ± 0.2 eV effective work function for most of the $SrVO_3$ samples, as well as ~2.3 eV for some datasets. It is noted that this effective work function cannot be easily interpreted. It is almost certainly neither the work function of any specific surface, nor the observed work function defined in Equation 2.10. As discussed in Sec 2.3.3, separate calculations of emission curves using more complex patch surface models[111] suggest that these curves are not easy to explain quantitatively with even much more sophisticated models. However, a plausible and self-consistent understanding of the surface could be

provided by semi-quantitatively combining this 2.3-2.7 eV effective thermionic work function under strong applied field together with the strong *J-V* dependence and the 4.1 eV UPS work function. The 4.1 eV UPS work function is the surface average work function measured under weak field conditions. As the applied field increases to ~0.75 kV/mm, the 2.3-2.7 eV effective work function implies a partial cancellation of patch field. Since the *J-V* curve has not reached saturation even at 1 kV/mm, an additional effective work function decrease is expected upon further cancellation of patch field. This result suggests there are significant amounts of the surface component with a local work function lower than this range, which may be SrO terminated (001) surfaces with a work function being near the 1.9 eV value predicted by DFT.

3.4.3 Comparison between $SrVO_3$ and other materials with low work functions

The discussion above provides strong evidence on the existence of the DFT predicted low work function SrO terminated (001) surface. Although the 2.3 to 2.7 eV effective work function is higher (likely due to the *partial* cancellation of patch field effect), it is still extremely low for a monolithic material system and dramatically lower than previously reported bulk perovskites values (see Sec 3.1). This result is therefore particularly interesting for both device applications and fundamental science aspects.

As discussed in Sec 2.2.2.2, the most commonly employed approach for achieving a low work function surface is to apply surface functional groups, with examples including dispenser cathodes,[3,65] 2D material work function modification on graphene[60] and MXene[201] electrodes with functional groups, and the use of Cs atoms to lower photocathode work function[36]. A main shortcoming for applying these surface species is that they are typically unstable, causing lifetime and contamination issues.

Some alkaline or alkaline earth metal oxides, such as Cs_2O_2, Cs_2O or BaO, have been reported to have work function values as low as 1 eV, measured by various methods including thermionic emission or photoemission[129,261–263]. However, many of these values are from fitting both *A* and Φ to the RLD Eq 2.3 and yield very low *A* values with the low work functions, which does not necessarily mean the existence of the real low work function surfaces, and a low *A* value represents low emission current densities. Therefore, these materials are likely not practical candidates for typical applications seeking low work function materials in order to realize high electron transfer rates across interfaces into vacuum or other materials. On the other hand, although some low work function values measured by photoemission (where *A* was not involved) may suggest higher reliability, these materials also suffer from poor bulk electrical conductivity and low melting and decomposition temperatures[264], making them unsuitable for many high-temperature applications like thermionic emission.

Bulk materials, including metals, oxides, and many other material categories, typically have relatively high work functions (larger than 4 eV). The commonly known low work function metals are alkaline metals[188], but they exhibit poor stability in the presence of oxygen or water, and melt or vaporize at elevated temperatures. One bulk material with relatively low work function, high electrical conductivity and high bulk stability at high temperature is LaB_6 (~2.7 eV work function), which is used as a thermionic cathode for electron microscopes and e-beam writers[55,265]. It is noted that the effective thermionic emission work function of $SrVO_3$ is comparable to LaB_6 upon the partial cancellation of patch field effect. Thus, with better materials processing approaches to obtain larger patches of the low work function surfaces, it is possible that $SrVO_3$ will yield

a lower effective work function than LaB_6. The comparison between $SrVO_3$ and other low work function materials has been summarized in the Table 3.3 below.

Table 3.3. Comparison of work functions and other related aspects between $SrVO_3$ and other low work function materials. References for the quoted work function values of each material are provided in the main text.

Material	Work function(s) (eV)	Comments
$SrVO_3$	2.3 to 2.7 (Thermionic emission) 1.9 (DFT)	Monolithic low work function material. Patch field effect was not fully overcome during experiment.
W-Ba dispenser cathodes	2.0 (without Sc) or 1.5 (with Sc) (Thermionic emission)	Relying on volatile Ba surface species, causing contamination and lifetime issues.
Cs_2O, Cs_2O_2, BaO functional groups	As low as 1 eV (Thermionic and photoemission)	Possible error in work function interpretation. Poor electrical conductivity, stability and high-temperature capability.
Alkaline metals	K: 2.29 Cs: 1.95	Low melting point and poor stability.
Bulk materials other than alkaline metals	Mostly > 4 eV	Most have relatively high work functions.

LaB_6	~2.7 eV (Thermionic and photoemission)	Commercialized for e-beam writers. Work function likely comparable or higher than $SrVO_3$.

3.5. Chapter conclusion

In this chapter, the experimental investigation of bulk, polycrystalline $SrVO_3$ has been discussed. The samples were synthesized, characterized and tested as a new candidate thermionic emitter material. The influence of two key factors: metastability of $SrVO_3$ and patch field effect, were carefully investigated, and both of these factors were observed to have significant impact on the measured work function and emission behavior. Being aware of these two factors, the results of emission tests under carefully controlled conditions indicate the existence of low work function surface patches (~ 2 eV) and a reproducible ~2.7 eV effective work function. In a limited number of cases, the emission measurements realized effective work functions as low as ~2.3 eV. With a series of DFT calculations on surface energies, excellent consistency was shown between experimental and computational results, both supporting patch field arguments to interpret the results and suggesting the existence of low work function (001) AO terminated surfaces.

The thermionic emission results of 10-100 $mA \cdot cm^{-2}$ at ~1000 ℃ and an effective thermionic work function of 2.7 eV of polycrystalline $SrVO_3$ are comparable to commercial LaB_6 thermionic cathodes that are widely used in electron microscopes, e-beam lithography and X-ray tubes. In addition, $SrVO_3$ exhibits thermionic emission without relying on volatile barium to lower the work function, which is a possible solution to the shortcomings of current dispenser cathodes on contamination and lifetime. Moreover,

the 2.3 eV effective work function observed in some of the measured data sets is the lowest reported work function for a bulk, monolithic material so far, indicating that $SrVO_3$ is a practical cathode candidate for thermionic electron transfer across interfaces into vacuum or other materials.

These findings suggest that there are low work function perovskite surfaces consistent with those suggested by DFT predictions and demonstrate the potential of using carefully designed and processed perovskite oxides such as $SrVO_3$ for next-generation thermionic emitters[12]. More broadly, the combination of computational and experimental efforts validate the general idea that work function engineering with intrinsic polar materials like perovskites is realizable with processing design. A more detailed examination of processing and control of the surface termination and morphology could result in further reduction of the effective work function and higher emitted thermionic current densities. $SrVO_3$ and related materials therefore represent a promising subject for further research, where the use of intrinsically polar perovskites may be used for extreme (low or high) work function engineering, with potential applications in fields as diverse as solid-state electronic devices, electrocatalysts, and thermionic energy converters.

Chapter 4 – Investigation on polycrystalline $BaMoO_3$ as a thermionic emitter

This section contains the experimental exploration of $BaMoO_3$ for potential thermionic emission applications. This work results in an article I first authored: **L. Lin**, R. Jacobs, D. Morgan and J. Booske, "Investigation on polycrystalline $BaMoO_3$ as a thermionic emitter", which is currently in preparation and will be submitted to *IEEE Transactions on Electron Devices* very soon. Meanwhile, there are a bunch of highly speculative results and discussions regarding the emission behavior and surface chemistry of $BaMoO_3$ and related compounds, which are also included in this chapter.

4.1 Introduction

As mentioned in Sec 2.1.2.1 as well as other sections, it is critical to develop low work function materials for enhanced electron emission. The most commercialized electron emission cathodes in industry are dispenser cathodes relying on polar BaO adsorbates on W matrix to lower the work function from 4.5 eV to 2 eV[3,58,59,123]. Despite the success on lowering the work function and operating temperature, dispenser cathodes are generally not easy to fabricate by involving W particle sintering, Ba-containing salt preparation, impregnation, as well as Sc_2O_3 nanoparticle integration for scandate cathodes[3,58]. This is partially solved with the recent progress in 3D printing techniques, but more simplified and straightforward fabrication procedure would still be greatly beneficial to the electron source industry.

As introduced in Chapter 3, recently it has been shown both computationally and experimentally that complex oxides such as perovskites could exhibit low work functions

with intrinsic polar surfaces[11,67,121]. One outstanding example is perovskite $SrVO_3$, which exhibited evidence of low work function surface agreeing with previous DFT predictions, as well as 2.3 to 2.7 eV effective work functions in thermionic emission[11]. The emission behavior corresponding to low surface work functions on $SrVO_3$ were activated by recovering from surface over-oxidation and partially cancelling patch field effect, making $SrVO_3$ the first bulk, monolithic, conductive oxide material showing low work function surfaces and relatively high thermionic emission, without relying on any externally introduced dipoles. The success of $SrVO_3$ raised up another question: are there any other perovskite oxide that could also show this low work function and reasonably good thermionic emission with a similar mechanism?

This chapter addressed these aspects through the investigation of $BaMoO_3$, another conductive polar perovskite oxide with low 1.0 eV DFT predicted work function on its (001) AO-terminated surface[12]. Experimental results proved that polycrystalline $BaMoO_3$ could also show significant thermionic emission, although the exact emitting surfaces and emission mechanisms are not totally clear. The sample without 1270 to 1300 ℃ ultrahigh vacuum annealing showed ~2.7 eV effective work function, which provide another strong support for the idea of achieving relatively strong emissions and corresponding low work functions from intrinsic polar surfaces. It was also observed from the J-V relationship that the patch field effect induced by facets with several-micron sizes were likely fully overcome. However, the much higher experimental effective work function in this case than the DFT predicted lowest work function suggested that the single facets likely contained nanofeatures with sizes on the order of ~10 nm, altering the single-facet local work functions to much higher values. Moreover, a significantly increased thermionic

emission current density was observed after 1270 to 1300 ℃ annealing in ultrahigh vacuum, corresponding to 2.3 to 2.6 eV effective work functions, which was lower than the non-annealed case. Further characterizations indicated that these high-temperature annealed samples experienced significant phase transformations, likely corresponding to the volatility of Ba with some degree of similarity compared to dispenser cathodes.

4.2 Experimental methods

Many experimental steps were similar to the preparation and investigation of $SrVO_3$ described in Sec 3.2. Specifically, polycrystalline $BaMoO_3$ samples were prepared via a high-temperature solid state reaction route[266]. In a typical reaction, around 2 g of $BaMoO_3$ powders were synthesized by directly reducing the $BaMoO_4$ precursor powders (Alfa Aesar, 99.9%) at 900 ℃ with 280 sccm flowing 5% H_2/95% Ar gas (from Airgas). The dark red $BaMoO_3$ powders were then ground with a mortar-and-pestle set and pressed into round-disk-shaped pellets with a pressing die at 200 MPa pressure. The pellets were then sintered at 1250 ℃ with 280 sccm flowing gas mixture of 0.15% of H_2 balanced with Ar (achieved by mixing 8.4 sccm 5% H_2/95% Ar gas and 271.6 sccm ultrahigh purity Ar from Airgas).

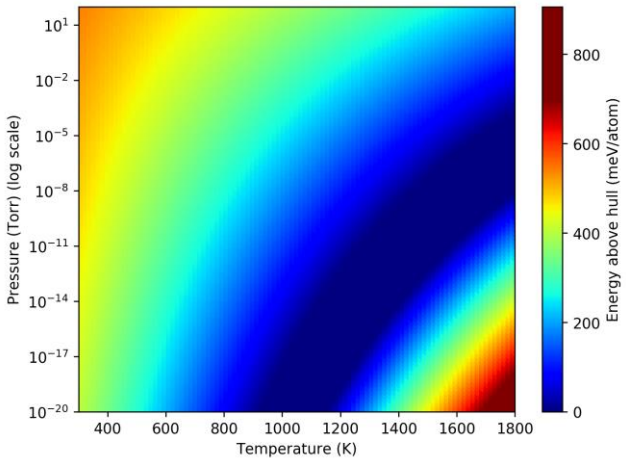

Fig 4.1. Stability phase diagram of $BaMoO_3$ calculated through DFT, also suggested a stable window for $BaMoO_3$.

The selections of preparation temperatures and hydrogen concentrations were based on the same strategy as what was employed in the $SrVO_3$ work[11,236], with the DFT predicted phase diagram shown in Fig 4.1. One more complexity of $BaMoO_3$ is, it has a relatively low melting point between 1350 ℃ and 1400 ℃, compared to the over 2000 ℃ counterpart of $SrVO_3$. These steps resulted in dark red pellets for further characterization and testing.

All Powder XRD experiments were processed a Bruker D8 Discovery diffractometer and Cu Kα radiation (wavelength: 1.54 Å). The morphologies of pellets were studied with a Zeiss Gemini 450 SEM and a Zeiss LEO 1530 SEM. Energy dispersive spectroscopy (EDS) was done with the SEM instruments. The atomic concentrations and chemical states within the near-surface regions were studied with a Thermo Scientific K-Alpha XPS with monochromatic Al Kα radiation (Photon energy: 1486.68 eV), and the atomic percentages were analyzed through the Thermo Avantage software integrated with the XPS spectrometer.

Thermionic emission testing was processed with a home-made experimental setup in UHV, very similar as described in Chapter 3. Basically, the samples were sitting above a filament and were heated up by the electron beam emitted from the filament, and the thermionic emission from the samples were collected by positively biased anode fixture. The major difference compared to the setup for $SrVO_3$ testing was, to not count the emission from the Mo sample cap with Ba contamination (which will be further discussed in Sec 4.3), the anode fixture was modified, as shown in Fig 4.2. In the modified setup, a piece of W foil with a 1 mm diameter hole at the center was used as the anode to provide acceleration field for emitted electrons, rather than the grid design employed in $SrVO_3$ experiments. The catcher for electron collection was also extended with a cylinder made

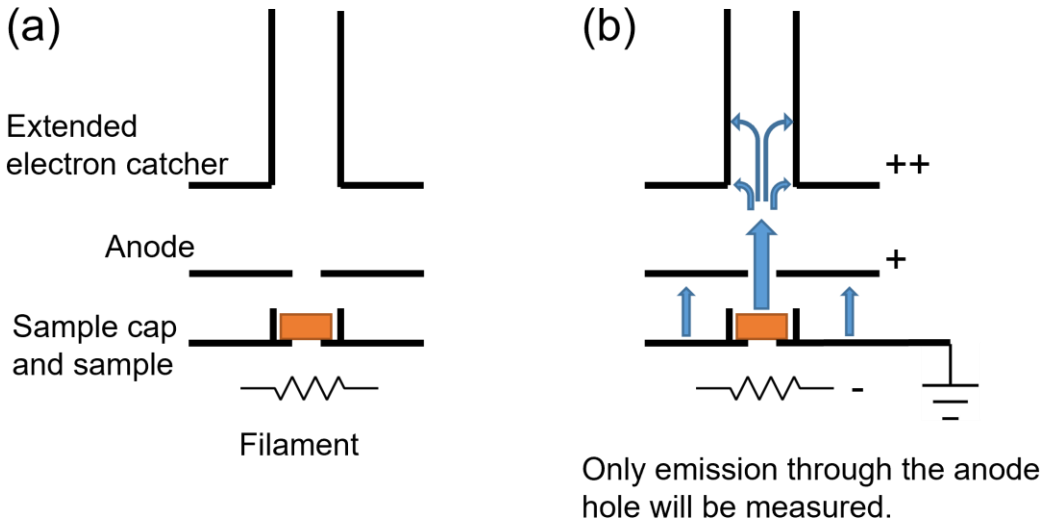

Fig 4.2. The modification of the emission testing fixture for $BaMoO_3$ testing due to the Ba contamination issue. (a) The anode was a solid piece of W metal with a hole rather than a mesh grid, and the electron catcher was further extended. (b) Electron flow during emission testing. Only the emission from the area directly aligned with the anode hole (presumably $BaMoO_3$ sample) would be collected by the extended catcher.

by Ta foil in order to collect more electrons. During a measurement, W anode was placed at a 3 mm distance above the sample with the hole aligned to near the sample center, and the extended catcher was placed at 5 mm above the W anode. The catcher was biased to constant +2.5 kV, and a set of pulses with 0 to +2 kV changeable voltages, 25 μs width and 10 Hz frequency were applied to the W anode to accelerate the electrons (same pulse setup used for $SrVO_3$ in Chapter 3). This design only enabled electrons emitted from the sample area right beneath the hole to pass through it and collected by the extended catcher (assuming electrons have predominantly perpendicular velocity). By only measuring the emission current flowing through the catcher, the impact of the Ba-contaminated Mo sample holder could be eliminated. The major drawback of this design was a much smaller effective emission area (0.79 mm^2 compared to the 3.1 mm^2 emission area in $SrVO_3$ experiments), which in turn decreased the total emission current and signal-to-noise ratio.

Similar as the argument provided in Sec 3.4.1 for $SrVO_3$, the $BaMoO_3$ samples were heated at 1150 ℃ for overnight prior to emission testing, to transform the near-surface over-oxidized phase into perovskite phase. The samples were then tested in a temperature range of 800 to 1300 ℃, and all the emission testing experiments were processed during sample cooling down (i.e., the samples were heated to the maximum temperature initially, and gradually cooled down to targeted temperatures for emission measurement). In some experiments, the samples were kept at 1270 to 1300 ℃ for 0.5 to 4 hours before emission measurement (such samples were categorized high-temperature *in situ* annealed samples). The corresponding emission current flowing through the extended catcher was then measured with a current monitor made by Pearson Electronics, and a LeCroy WaveSurfer 44Xs 400 MHz, with the same emission current extrapolation method discussed in Sec 3.2.2. The sample temperature was measured with an optical pyrometer from Leeds & Northrup, CO. by viewing the sample at 655 nm red light through the hole, catcher, glass viewport on the vacuum chamber wall, and a mirror, in the same manner as the $SrVO_3$ experiments. The measured brightness temperature T_b was corrected to the actual temperature T, again using Planck's black body radiation law (Eq 3.3) with an effective emissivity of $\varepsilon = 0.7068$ by assuming a black body approximation from the sample $\varepsilon_{Sample} = 1$ and considering the correction from the mirror and viewport.

4.3 Results and discussions

4.3.1 Phase, morphology, and surface chemistry of as-sintered pellets

The as-prepared pellets showed a dark red color, agreeing with previous reports on $BaMoO_3$[266]. As shown in Fig 4.3 (a), powder XRD results suggested the major bulk phase was cubic perovskite $BaMoO_3$ with a space group of $Pm\bar{3}m$, consisting of 98% of the total

crystalline sample mass. The major impurity phase is metallic Mo, which could be attributed to slight over-reduction during processing. Since the fraction of Mo phase was very low, and the work function of Mo is relatively high (4.6 eV), it will not strongly affect the thermionic emission behavior from the perovskite majority phase.

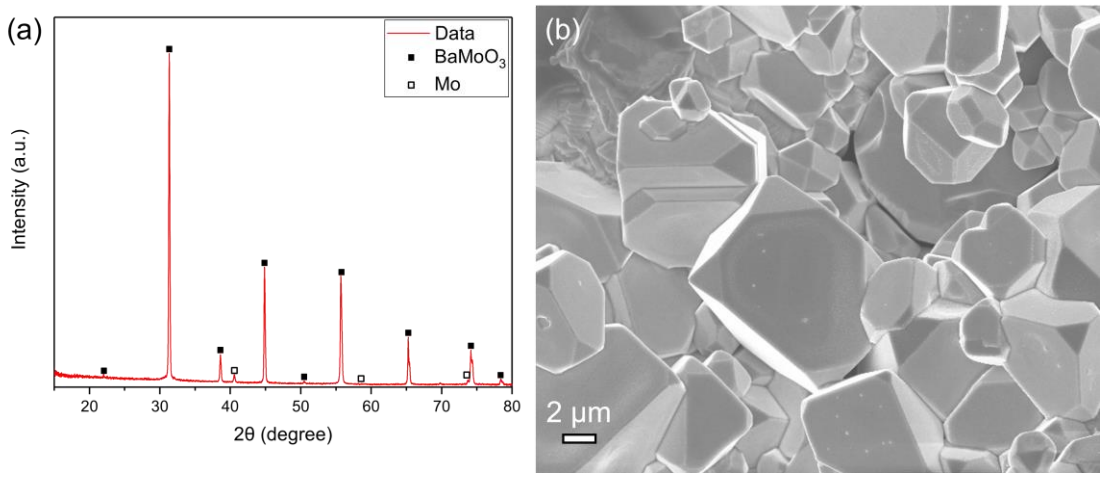

Fig 4.3. (a) Powder XRD data for polycrystalline $BaMoO_3$ with retrieved record from database, showing a high phase purity. (b) Morphology of the sintered polycrystalline $BaMoO_3$ pellet captured by SEM, suggesting the possible existence of (001) surfaces by evaluating the facet shape. The typical observed grain size is estimated to be between 2 to 10 μm.

The surfaces of polycrystalline $BaMoO_3$ pellets consisted of highly faceted grains, as indicated by SEM. Compared to the $SrVO_3$ samples in Chapter 3, the grain sizes of $BaMoO_3$ were much larger, with a typical value of 2 to 10 μm, due to the lower melting point of $BaMoO_3$ that means a lower kinetic limit for grain growth. This is important for its thermionic emission behavior due to the patch field argument provided in Secs 2.2.1.3, 2.3.3 and 3.4.2. Because of the cubic nature of perovskite $BaMoO_3$, the facets on the grains could be attributed to specific surface orientations by evaluating their shapes and geometric relationships with the adjacent facets on the same grain[253]. As shown in Fig 4.3(b), a

significant portion of surface area were attributed to (001) surfaces, the orientation possibly containing low work function AO terminated surface.

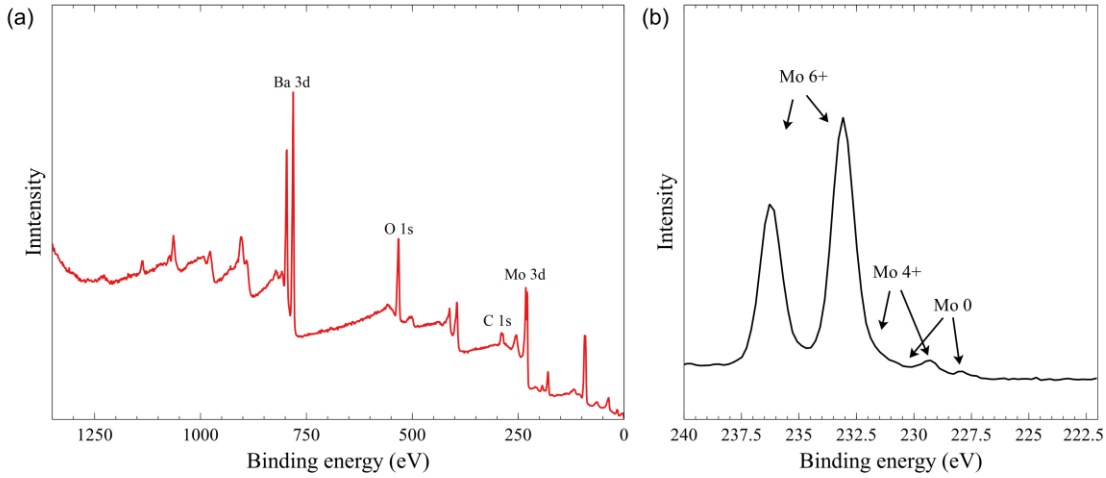

Fig 4.4. XPS results on as-sintered $BaMoO_3$ pellets. (a) Survey scan, showing the near-surface region contained Ba, Mo, O and C. (b) Mo 3d core level scan, indicating a mixed oxidation states of Mo 6+, 4+ and 0. The predominantly Mo 6+ suggested the surface was also over-oxidized during sample preparation and/or transition.

The surface sensitive XPS suggested the near surface region contained Ba, Mo, O and C elements, with a typical atomic ratio of 13.2%, 13.9%, 50.7% and 22.2%, respectively, shown in Fig 4.3 (a). The ratio of Ba to Mo was approximately 1, suggesting the A-site and B-site cation ratios on the surface were not significantly different from its bulk counterpart, indicating no significant A-site segregation happened during sample preparation and sintering. Additionally, there was a significant amount of C atoms on the surface, suggesting the surface was contaminated by CO_2 or organic molecules in the air or XPS chamber, and the much higher concentration of C indicated that the surface of $BaMoO_3$ is very carbon-philic. Similar as what was previously found in $SrVO_3$, this carbon signal could be easily removed by an Ar^+ ion sputter-etching process to etch away the top ~1 nm, suggesting the carbon contamination was limited to be on the surface. Furthermore, as shown in Fig 4.4(b), the oxidation states of Mo on the surface consisted of Mo 6+, 4+,

and 0 valence components, with the 6+ component as the predominant one, indicating the near-surface region was over-oxidized during cooling down, when the ambient H_2 gas in the furnace was not active enough to maintain a low oxygen partial pressure by water-formation reaction (see detailed discussion in Secs 3.2.1 and 3.4.1), or sample transfer from the furnace to the XPS chamber, when the samples had to be exposed to the air for at least 20 minutes. Therefore, in order to realize the properties associated with $BaMoO_3$'s possible low work function, a similar *in situ* thermionic emission testing approach was selected compared to the $SrVO_3$ discussed in Chapter 3, with an annealing step processed in UHV right before thermionic emission testing to transform the near-surface region into perovskite phase of interests.

4.3.2 Thermionic emission testing without high temperature annealing – multiple-scale patch field effects

The point and the spirit of patch field effect discussed throughout this dissertation is emphasized again here, i.e., the work function heterogeneity will introduce a lateral electric field that pulls back the electrons emitted from the low local work function areas. The observed work function, which is the energy barrier for an electron emitted from the surface, is a function of the local work function heterogeneity and applied electric field on the surface. Generally, the observed work function will be equal to the area-weighted average across the detection area when the applied electric field is weak, and will gradually decrease to lowest local work function as applied field increases. The critical field needed to cancel out the patch field and reveal the lowest local work function could be roughly estimated by dividing the surface work function heterogeneity with patch dimension, as shown in Eq 2.12.2.

Given a typical work function differences of several eV among different surfaces for perovskites like $BaMoO_3$, and a typical facet size of a few μm suggested by SEM images of $BaMoO_3$, a very rough estimation on the lower bound of the critical field will be several hundreds of V/mm, assuming there is one single local work function on each facet. This value is much higher than the typical applied field in the canonical ultraviolet photoelectron spectroscopy (UPS) work function measurement (~0.1 to 1 V/mm), meaning that the lowest work functions on the surfaces of the $BaMoO_3$ samples are nearly impossible to be directly measurable with UPS.

Therefore, the direct UPS work function measurement was not carried out on $BaMoO_3$. On the other hand, as in the case of $SrVO_3$ introduced in Chapter 3, thermionic emission testing was processed because it enabled the use of up to 700 V/mm electric field on the sample, which is likely larger than the lower bound of critical field estimated above. As discussed in Sec 4.3.1, the samples were *in situ* heated in UHV at ~1150 ℃ to eliminate the near-surface over-oxidized layer. The samples were first kept at temperatures lower than 1200 ℃ for testing the relationships between thermionic emission current density J and applied A-K voltage V, and between J and sample temperature T. Similar as Chapter 3, given the high V and short A-K distance d, the emission should be within TL regime, where J from an ideal surface with a single work function Φ at temperature T should be governed by RLD Eq 2.3 with ideal Richardson constant derived from quantum mechanics $A = 4\pi m_e e k^2/h^3 = 120$ A·(cm·K)$^{-2}$. Meanwhile, J should only be weakly dependent on V via Schottky effect Eq 2.11, with a combined J- V dependence indicated by Eq 3.5. However, based on the observations on $SrVO_3$ discussed in Chapter 3, there could be a strong positive J- V dependence for a patchy emitting surface even within the TL regime.

In fact, this behavior was also seen on $BaMoO_3$ at low voltages (shown in Fig 4.5(a)), where J significantly increased as V went higher. After and V reached about ~750 V, the

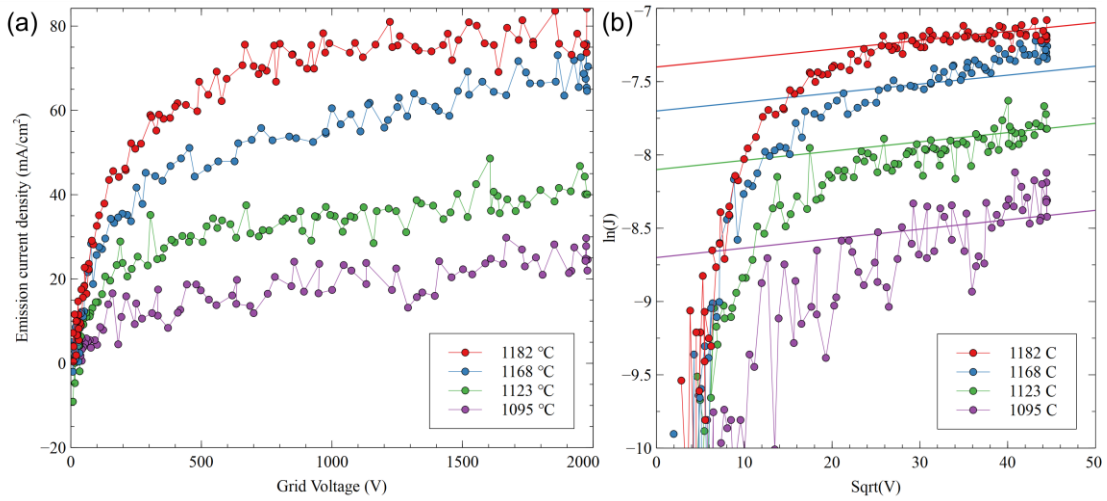

Fig 4.5. J- V relationship of the thermionic emission from $BaMoO_3$ pellets without prolonged high temperature annealing. (a) Direct J- V plot, showing an initial rapid increasing of J as V increases, and changed to a weaker positive dependence when V is greater than ~750 V. (b) $\ln J$ - $\sqrt{V}$ relationship, suggesting when V is high, the slopes of the data agrees with corresponding Schottky slopes predicted by Eq 3.5, especially for the higher temperature dataset due to a higher signal-to-noise level.

emission current density changed to a slow increasing trend vs. further increasing V. When further plotting the $\ln J$ - $\sqrt{V}$ relationships at different temperatures (cf. Fig 4.5(b)), it could be seen that the slopes of the slowly-increasing region matched Schottky slopes very well, indicating the patch field at this scale was fully overcome, and the weak J- V dependence could be attributed to (normal) Schottky effect. Furthermore, given that the emission current density changed to slow increasing when V reached ~750 V, the corresponding 250 V/mm could be thought of as the critical field, which also agreed well with patch field theory with the typical grain size of several μm and patch work function difference on the order of 1 eV.

The *J*- *T* relationship of one representative sample that was not heated to above 1200 ℃ was then plotted in Fig 4.6 as Dataset #BMO-1, with a 1.5 kV A-K voltage, to evaluate the cathode performance through effective work function extrapolated from RLD

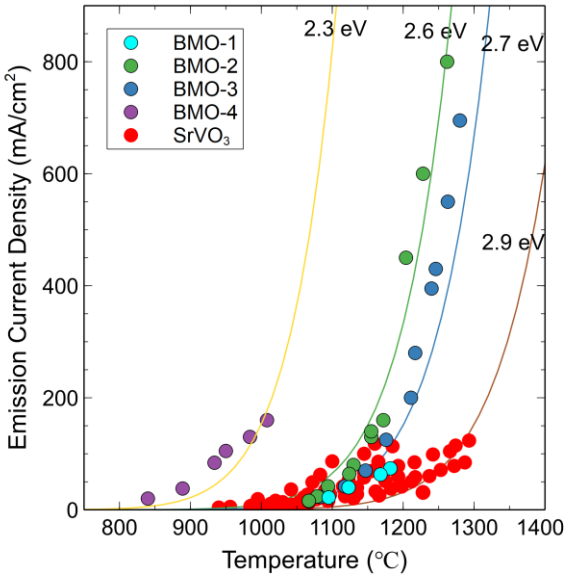

Fig 4.6. *J*- *T* relationship of the thermionic emission from $BaMoO_3$ pellets. Dataset #BMO-1without prolonged high temperature annealing, and the other dataset with such annealing associated with possible phase change, with the typical $SrVO_3$ emission behaviors also illustrated. The #BMO-1 behavior is discussed in Sec. 4.3.2, while the others are discussed in Sec. 4.3.3.

Eq. 2.3 (see detailed discussion in Secs 2.4.3 and 3.4.2). Such data from a sample without high-temperature annealing suggested that the emitting surface had a 2.7 eV effective work function, upon fully cancellation of micron-scale patch field, with emission current density deviates toward higher work function side from the ideal RLD Eq. 2.3, showing similarity as previous $SrVO_3$'s emission behavior. This is a relatively low work function value comparable to the previous report on $SrVO_3$ and commercialized LaB_6 cathodes[11,55,56], again proved the idea that the polar oxides such as perovskites could show low work functions, and likely be promising candidates for various applications requiring low work functions. However, this value is much higher than the DFT predicted 1.0 eV (001) BaO-

terminated work function (note the patch fields induced by several-micron sized facets have been fully overcome). One possible explanation on this inconsistency is the existence of more complex multi-length-scale patch fields.

To verify this assumption, the phase, surface chemistry and morphology of samples after (<1200 ℃) emission testing were carefully characterized. The color of these pellets remained dark red, and XRD suggested the majority phase was still perovskite $BaMoO_3$. The XPS results were similar as those from as-sintered pellets, also suggesting the pellets likely remained mostly as perovskites from the bulk throughout the surface, rather than transferring to other phases. SEM images shown in Fig 4.7(a) still exhibited the several-

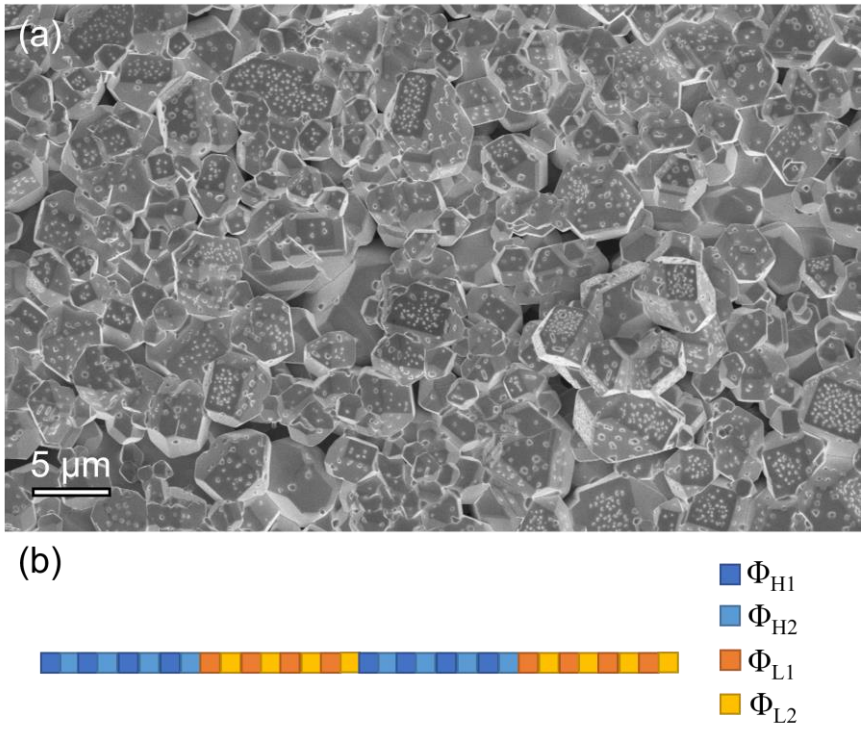

Fig 4.7. (a) SEM image of a $BaMoO_3$ sample after low-temperature emission testing. It could be clearly seen while the grain sizes were not significantly changed, there were small features evolved on each single facet, which may alter the overall facet work function. (b) Illustration of a surface containing patches with two different length scales, and the work function interpretation is usually not straightforward.

micron facets. However, there were small features shown up on top of each facet, which had length scales of ~10 nm. This indicated that each single facet, although likely shows a single work function at micron scale, may contain nano-scale surfaces associated with different work functions, as illustrated in Fig 4.7(b). Thus, the local work function (i.e., the work function defined at a few nanometers away from the surface of interests, see Sec 2.2.1.2) for a micron-scale facet may actually be the average of many nanometer-sized patches, and is possible to be much higher than the DFT predicted lowest (001) AO-terminated work function value. This provides a self-consistent explanation to the low-temperature annealed emission behavior.

Additionally, the patch field theory also suggested that in order to reveal the lowest work function for patches with this small dimension, a 10^5 V/mm electric field is needed. Such strong field is not achievable with the instruments available for me during my dissertation work for safety concerns. Moreover, this strong field will introduce much more complex emission physics which includes not only strong Schottky effect, but also significant electron tunneling through the surface barrier, making the actual emission combined with F-N field emission. Therefore, the DFT predicted 1.0 eV is not possible to be directly measured or straightforwardly extrapolated on these polycrystalline samples, but this two-scale patch field argument provides a self-consistent explanation to the observed thermionic emission behavior of $BaMoO_3$.

4.3.3 Emission testing with high-temperature annealing – Ba volatility, segregation, and material decomposition

(Note: some of the discussions in this section are highly speculative, and more work would be needed to confirm or deny some of the assertions made here.)

Despite the 2.7 eV relatively low effective work function, the emission current density was still relatively low in #BMO-1 dataset. Therefore, the samples were further heated up to 1300 ℃ to pursue a higher emission current density. This resulted in much higher emissions, but there were significant structural and surface chemical changes from the sample's original perovskite phase, likely originated from volatile Ba, making the emission behavior and emission physics much more complex.

Prior to emission testing, the sample yielding Datasets #BMO-2 and #BMO-3 were heated at 1270 ℃ for 4 hours to stabilize the higher emission. The resulting thermionic emission current densities shown in Fig 4.6 were able to reach a much higher level than the lower temperature emission from #BMO-1. Meanwhile, even when the samples were cooled down to the same lower temperature range of #BMO-1, the emission current density are also higher, resulting in a slightly lower 2.6 eV work function. Meanwhile, from the J-V plots of #BMO-2 and #BMO-3 (shown in Fig 4.8) it could be seen that there is a stronger J-V dependence at higher temperatures. This showed similarity to the patchy dispenser cathode's emission, especially for the trend that gradually deviated from the full space

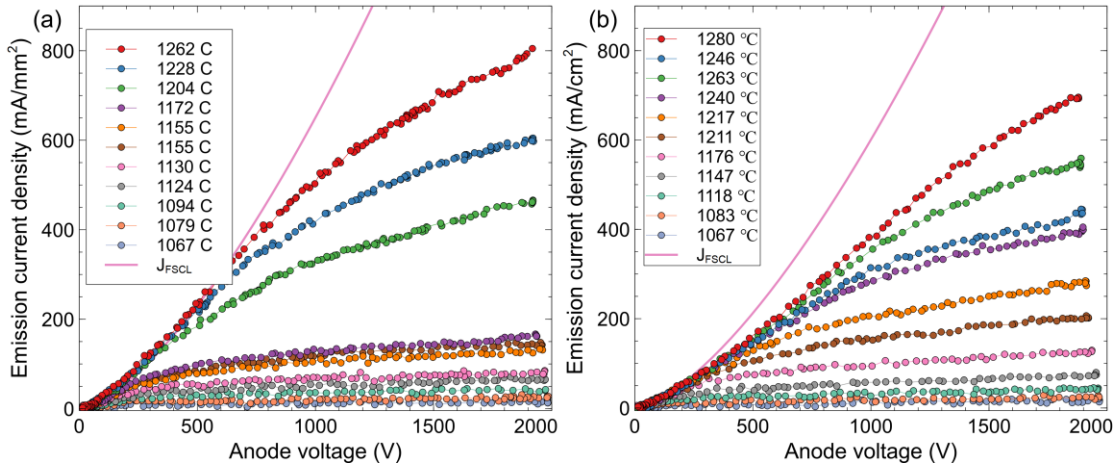

Fig 4.8. J-V dependence of thermionic emission from #BMO-2 (a) and #BMO-3 (b).

charge limited current density when V increases[111]. The fact that J did not quickly reached saturation for these conditions is also likely due to the heterogeneous emitting surfaces, and such behavior was also similar to some observations on dispenser cathodes.

When further heating up another sample to a temperature of 1300 ℃, the emission current first increases, but then rapidly diminished after kept at 1300 ℃ for 10 to 20 min. This is likely due to the evaporation loss of surface segregated Ba with strong desorption driving force. When the sample was cooled down to ~1000 ℃ and kept for ~10 min, the emission current recovered to ~ 170 mA/cm^2, corresponding to a 2.3 eV effective work function, as shown in Fig 4.6 as Dataset #BMO-4. When this sample was further cooled down until ~800 ℃, the emission current density still follows the approximately same 2.3 eV effective work function RLD curve (see #BMO-4 in Fig 4.6).

Post-emission characterizations further suggested the possible phase transformation and surface evolution for high temperature annealed samples. As suggested in Fig 4.9(a), XRD suggested the high-temperature annealed samples experienced significant phase transformation, resulting in a bunch of phases other than perovskite $BaMoO_3$, including metallic Mo, MoO_2, and many other complex phases containing Ba, Mo and O. SEM shown in Fig 4.9(b) suggested a dramatic morphological change by showing the formation of many large grains, with EDS suggested a significant higher Ba concentration than Mo (atomic percentage ratio of Ba:Mo is 3:1), indicating these grains were likely Ba-rich phases resulting from segregation. Surface atomic concentration analysis via XPS (Fig 4.8(c)) showed predominantly Ba and O signal, with much smaller Mo peaks, further indicating a strong surface Ba segregation. These characterization results

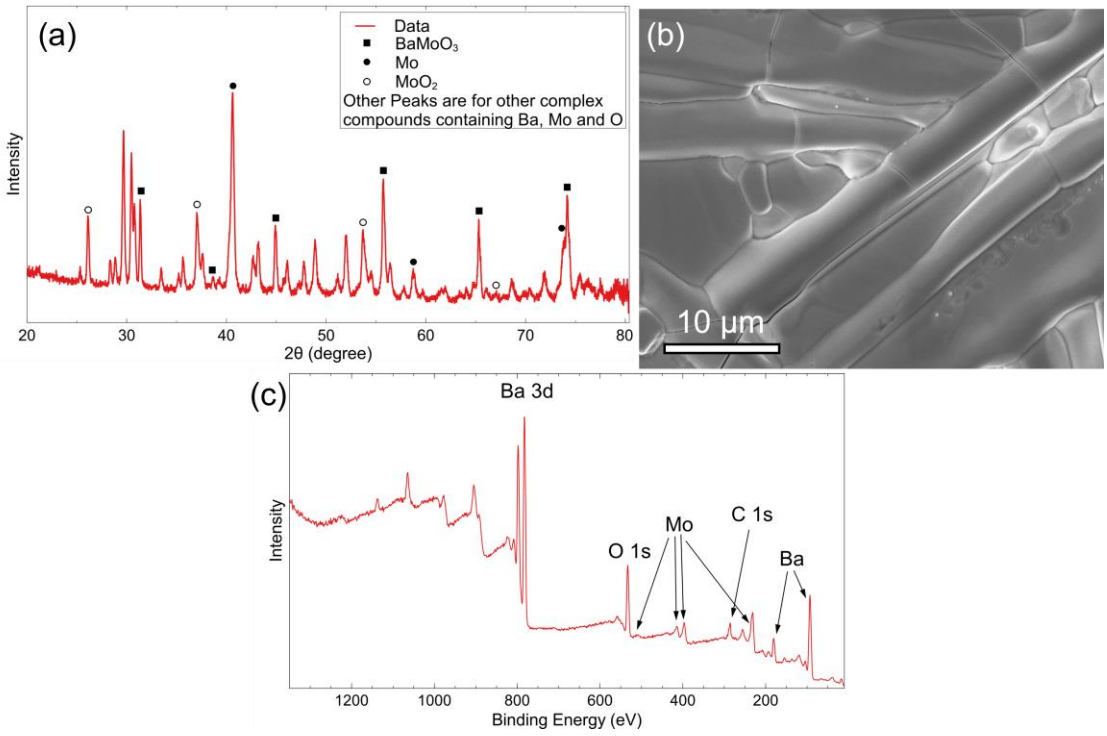

Fig 4.9. (a) XRD result on a $BaMoO_3$ sample after emission testing with high temperature annealing, indicating phase transformation by showing peaks attributed to Mo, MoO_2 and other complex Ba-Mo-O phases. (b) SEM image on a $BaMoO_3$ sample after emission testing with high temperature annealing, showing the formation of phases with large grain sizes. (c) XPS survey scan on a $BaMoO_3$ sample after emission testing with high temperature annealing, indicating the surface segregation of Ba by showing a dramatically increased Ba to Mo atomic ratio from 1:1 (pre-testing samples) to 3:1.

suggested that the high temperature emission testing possibly triggered the decomposition of perovskite $BaMoO_3$: During high temperature heating, volatile Ba likely segregated onto the surface and eventually evaporated, possibly leaving metallic Mo and MoO_2 behind in the bulk. The evaporation of Ba was likely supported by observing the deposition of Ba-containing film deposited on the bottom surface of W anode, as well as the EDS on some regions of the pellets showing only Mo as the primary element heavier than O.

Such $BaMoO_3$ decomposition and phase transformation likely suggested that an important reason causing the higher emission current densities of #BMO-2, #BMO-3 and

#BMO-4 was the possible Ba segregation towards the surface after high temperature annealing. Specifically for #BMO-4 dataset, the possible phase evolution and Ba enrichment on the surface provided a plausible explanation to the emission behavior. At very high temperatures (~1300 ℃), the Ba-rich species (one possible example is BaO) adsorption on the emitting surface is unstable, and most of the adsorption species were evaporated up. As the temperature went down to 1000 ℃, the kinetic factor of such Ba desorption was critically reduced, and a relatively (may be dynamically) stable Ba-rich layer is possible to form on top of the pellet surface by balancing the evaporated Ba from the surface to the vacuum, and Ba supply originally in the bulk phase, and released during thermionic emission at temperatures lower than 1000 ℃, making the emission behavior of the $BaMoO_3$ sample surface similar to a Ba-W dispenser cathode (relying on surface BaO layer to modify the work function). In fact, the work function of this emitting surface also showed some similarities compared to the ~2.0 eV (non-scandate) dispenser cathode effective work function.

It should be noted that although the effective work function values of $SrVO_3$ and $BaMoO_3$ are similar, the actual emission behavior and related physics differs a lot. First of all, the lower melting point of $BaMoO_3$ causes much larger grain sizes, which leads to weaker (micron-sized-facet-scale) patch field effect in $BaMoO_3$ that could be overcome with the applied field available in the lab. Furthermore, the decomposition of $BaMoO_3$ at 1270 to 1300 ℃ suggested that, unlike emitting as a conductive perovskite with intrinsic polar surfaces like $SrVO_3$, a $BaMoO_3$ cathode after some time of high temperature annealing was likely to have Ba-rich layers (which might be atomically-thin BaO dipole layer or a film containing some Ba-rich phases) attached on the top surface to assist the

thermionic emission. Such Ba volatility issue is similar as what has been widely known in dispenser cathodes. This possibly suggests that $BaMoO_3$ might serve as a possible substitution of conventional dispenser cathodes thanks to its similar emission mechanism but much simpler fabrication process, by straightforwardly synthesize and sinter the ceramic-based pellets at much lower temperature (1250 ℃), compared to conventional dispenser cathodes that require W or Mo matrix sintering at extremely high temperatures (over 2000 ℃) followed by complex procedure of impregnation of Ba-containing salts[3,10,64]. However, since the observed Ba evaporation, the durability of the emission from $BaMoO_3$ needs to be carefully examines, and likely to be further optimized towards longer lifetime.

4.4 Chapter conclusion

In this work, polycrystalline $BaMoO_3$ was synthesized and systematically investigated as a thermionic emitter candidate. There were clearly two types of emission behaviors depending on whether or not the samples were previously heated in ultrahigh vacuum at high temperature. The *J-V* relationship much flatter than $SrVO_3$ over 750 V A-K voltages, especially for the testing under lower temperatures, likely suggested that micron-sized patch fields were fully cancelled by applied electric field. The 2.7 eV effective work function for samples without experiencing 1270 to 1300 ℃ annealing was much higher than the DFT predictions although the samples themselves were likely perovskite $BaMoO_3$, possibly because of the nano-sized patches on each facet that raises the single-facet work functions. On the other hand, the samples that experienced higher temperature (1270 to 1300 ℃) annealing showed a much higher emission, but the phases and surface chemistry significantly changed due to the segregation and evaporation of Ba.

The nature of these higher-temperature-annealed samples showed some similarities to the dispenser cathodes, which might suggest a new simpler pathway of industrial cathode fabrication, but it is necessary to thoroughly explore the emission behavior and phase evolution of $BaMoO_3$ in the bulk and on the surface before making a certain conclusion.

Chapter 5 Concluding remarks

5.1 Summary and impact of this dissertation

In this dissertation, a number of key issues regarding work function have been discussed. Being the surface energy barrier for electron migration, the roles of work function in a vast array of cutting-edge applications including vacuum and solid-state electronics, catalysis, energy conversion, etc., have been discussed and evaluated. Targeting on solving the long-existing confusions on work function definition, measurement, and interpretation, an electrostatic energy approach has been employed, and a concept named observed work function has been introduced to evaluate the energy barrier behavior, especially with the presence of patch field effect. This approach greatly assisted the understanding on work function measurement methods. Moreover, work function could be effectively tuned by modifying the bulk electronic structures and surface dipoles, which is important in application aspects.

With the deeper understanding of work function physics, an approach of pursuing low work function materials with perovskite oxides for thermionic emitter applications. Guided by previous DFT predictions, $SrVO_3$ and $BaMoO_3$ were experimentally developed and investigated in their polycrystalline forms for work function and thermionic emission property evaluation. The relatively low 2.3 to 2.7 eV effective work functions and relatively high emission current density have been experimentally verified by realizing and interplaying with complex surface chemistry and patch field effect. $SrVO_3$ is the first bulk monolithic conductive oxide material being realized to have such low work function, providing strong support for the idea on work function engineering with intrinsic polar surfaces. The exploration on $BaMoO_3$ suggested that other perovskite oxides are also

possible to show relatively strong thermionic emission, with patch fields induced by micron-sized facets able to be fully overcome when patches are larger. Meanwhile, the nanofeatures on top of single facets could possibly induce nano-scale patch field that increases the facet local work functions. Moreover, the complex emission behavior, phase transformation and surface chemistry evolution of the high-temperature annealed samples are likely associated with the Ba volatility similar as commercialized Ba-W dispenser cathodes, but more thorough study is still needed for better understanding on these aspects.

The findings and discussions in this dissertation are crucial for research efforts involving work function and its engineering in different aspects. First of all, the work function physics discussed with the electrostatic energy treatment, together with the introductions of the observed work function and the discussion on patch field effect, is clear and informative, and the corresponding review article that is currently in the revision and resubmission process with *Physical Review Applied* for the first time provides such a clarification on confusing issues related to work function, and a useful guidance to correctly measure and interpret the work function of a surface. Additionally, the systematic summary of the application areas and approaching mechanisms of work function engineering could be potentially very useful for research involving surfaces and interfaces, which is extremely important both in frontier scientific research, and in industrial developments to make our everyday life better.

The realization of low work function on polycrystalline perovskite oxide $SrVO_3$ is an extremely critical finding. First of all, it validates the previous DFT work function prediction. Second, it belongs to a material system that never has been previously used for thermionic emission applications, which opens up a potential avenue for future exploration

on similar materials. Moreover, it is the first bulk, monolithic, conductive oxide material that shows this low work function without relying on any unstable surface species, which is particularly important not only for thermionic cathodes for vacuum electronic devices, but also has application potential in many related fields. Meanwhile, further exploration on $BaMoO_3$ will possibly provide a technological advance in electron source manufacturing in vacuum electronics community.

5.2 Suggestions for future work

Besides the further experimental exploration on the highly speculative discussions and assumptions on BaMoO3, there are a number of different directions deserving future research efforts. Some of them have been briefly summarized below.

5.2.1 Developing more physical electron emission models

In Secs 2.2, 2.3 and 3.4.2, work function and emission behaviors have been extensively discussed with the recognition of the roles of external and patch fields. Such understandings provide self-consistent explanations on work function measurements and emission behavior of $SrVO_3$ and $BaMoO_3$ emitters. However, the prediction and validation of the exact emission current densities versus temperatures and applied voltages (electric fields) with a fully theoretical or computational treatment by considering more precise surface characteristics are not yet available. As a result, the observed work function and emission behavior discussion remain relatively semi-quantitative by integrating only the simplest patch field and observed work function arguments.

Therefore, an emission model containing deeper physical understandings would be greatly beneficial not only for the fundamental research on electron emission, but also the

vacuum electronic and relevant industry. Some examples of deeper physical understandings include: more complex patch field models (e.g., patches with more than 2 local work functions, non-even sized patches, and multi-scale patches discussed in Sec 4.3.2), effect of surface roughness and porosity, temperature inhomogeneity, and models for non-thermionic emission (field emission or photoemission) current densities with patchy surfaces, etc.

5.2.2 More thorough investigation of processing-performance space for $SrVO_3$

In Chapter 3, the thermionic emission properties from polycrystalline samples have been studied carefully with the consideration of surface oxidation and patch field. However, the experiments described in Chapter 3 could still be further refined in terms of different processing and testing approaches, to get a more thorough investigation on the thermionic emission performance of $SrVO_3$.

In the previous experiments on $SrVO_3$, the samples were intentionally over-reduced to create a surface capping layer, and the layer was cleaved off before emission testing. This cleaving step introduced much uncertainty in sample preparation, which might be one of the major reasons of the emission behavior variations among different samples. Thus, it is worthwhile to develop a better-controlled $SrVO_3$ sample preparation process, to possibly reduce the deviations among samples.

The emission testing introduced in Chapter 3 showed a partial cancellation of patch field effect with a maximum 2 kV A-K voltage allowed by the available high-voltage power supply across a ~2 mm A-K gap. Since this electric field did not reach the critical field, a better understanding of patch field behavior on $SrVO_3$ samples, as well as a

presumably lower effective work function would be realized with stronger applied field, either by applying higher voltage with capable power supplies, or by altering the experimental setup to provide a better A-K gap control for smaller distances.

Additionally, the durability of $SrVO_3$ emission could also be further evaluated. In the previous tests, the typical testing time for each sample is ~20 to 40 hours. There were some initial results indicating the good reproducibility of the thermionic emission current densities, but prolonged testing (e.g., thousands of hours) is still needed to further verify the performance of $SrVO_3$ in a near-real cathode operating time scale.

5.2.3 Investigating work function and emission behaviors on higher quality well-controlled material surfaces

The $SrVO_3$ and $BaMoO_3$ samples included in this dissertation are all polycrystalline, thanks to their relatively low fabrication and processing difficulty. However, the polycrystalline nature of these samples have several significant drawbacks. First, the small grains induces huge patch field and anomalous emission behavior (especially in $SrVO_3$), greatly affected the overall emission performance, and caused confusions on the interpretation of exact emitting surface exploration. Second, the porous nature of the pellets significantly affected the electrical and thermal conductivity of the sample and between the sample and the heater base, making effective heating more difficult. Last, the rough top surface and possible associated field enhancement further complicate the emission physics.

These issues could be solved by performing research on highly controlled surfaces from high quality samples. For example, one work I co-authored on the transportation properties of $SrVO_3$ was performed on single-crystalline thin films grown on $SrTiO_3$

substrates with solid phase epitaxy[236], which is possible to have desirable low work function (001) SrO terminated surface in mm sizes, presumably having very weak patch field effects. Recently it is also reported that $SrVO_3$ could be grown as large single crystals[267], which would be greatly beneficial for both since understanding and device fabrication aspects. Highly controlled surfaces could also be achieved through molecular beam epitaxy or pulse laser deposition.

5.2.4 Studying materials with advanced characterization techniques

This dissertation has shown the work function heterogeneity and low work function evidence on $SrVO_3$ and $BaMoO_3$ with indirect experimental approaches including UPS work function measurement and thermionic emission testing. While this is a smart approach, it would be beneficial if the surface work function heterogeneity could be directly observed. According to the discussions in Secs 2.2.1.3, 2.3 and 3.4, this will require *in situ* measurements under high applied fields or with local probes.

One on-going work in collaboration with Brookhaven National Laboratory is using X-ray PEEM at elevated temperatures to directly observe the work function distribution of the $SrVO_3$ emitting surface, as well as the surface atomic arrangement and valence states of surface atoms associated with the work function distribution. Another promising technique is *in situ* KPFM, which presumably provides direct measurement of local work function of every single patch.

5.2.5 Investigating other material systems for thermionic emission, and broader work function engineering

The success of $SrVO_3$ and $BaMoO_3$ strongly indicated that the idea of work function engineering with intrinsic polar materials would be valid for more material systems. In fact, according to Jacobs et al.[67] and Zhong and Hansmann[121], a handful of perovskite oxides also have low work function (001) AO-terminated surfaces, good electrical conductivity, and robust stability under specific operating conditions. Therefore, it would be a very interesting and important topic to evaluate the performance of these materials with experiment.

Such effort has actually been started in my Ph.D. research. Other than $SrVO_3$ and $BaMoO_3$, a bunch of perovskite low work function candidates have been synthesized or commercially available, including $SrNbO_3$, $SrMoO_3$, $SrV_{1-x}Ti_xO_3$, Ba doped $SrVO_3$, $La_xSr_{1-x}MnO_3$, and Nb doped $SrTiO_3$. Further characterization and emission evaluation on these materials would be greatly helpful not only for perovskite thermionic emitter development, but also the general work function engineering.

References

[1] L. Lin, R. Jacobs, T. Ma, D. Chen, J. Booske, D. Morgan, *Submitt. to Phys. Rev. Appl.* **2022**.

[2] S. HaŁas, *Mater. Sci. Pol.* **2006**, *24*, 951.

[3] D. M. Kirkwood, S. J. Gross, T. J. Balk, M. J. Beck, J. Booske, D. Busbaher, R. Jacobs, M. E. Kordesch, B. Mitsdarffer, D. Morgan, W. D. Palmer, B. Vancil, J. E. Yater, *IEEE Trans. Electron Devices* **2018**, *65*, 2061.

[4] R. T. Tung, *Mater. Sci. Eng. R Reports* **2001**, *35*, 1.

[5] C. G. Vayenas, S. Bebelis, S. Ladas, *Nature* **1990**, *343*, 625.

[6] S. Lee, S. J. Tark, C. S. Kim, D. Y. Jeong, J. C. Lee, W. M. Kim, D. Kim, *Curr. Appl. Phys.* **2013**, *13*, 836.

[7] J. A. Becker, *Rev. Mod. Phys.* **1935**, *7*, 95.

[8] N. Bundaleski, J. Trigueiro, A. G. Silva, A. M. C. Moutinho, O. M. N. D. Teodoro, *J. Appl. Phys.* **2013**, *113*, 183720.

[9] T. Schultz, P. Amsalem, N. B. Kotadiya, T. Lenz, P. W. M. Blom, N. Koch, *Phys. Status Solidi Basic Res.* **2019**, *256*, 1.

[10] J.-M. Roquais, B. Vancil, M. Green, In *Modern Developments in Vacuum Electron Sources* (Eds.: Gaertner, G.; Knapp, W.; Forbes, R. G.), Springer International Publishing, Cham, **2020**, pp. 33–82.

[11] L. Lin, R. Jacobs, D. Chen, V. Vlahos, O. Lu-Steffes, J. A. Alonso, D. Morgan, J. Booske, *Adv. Funct. Mater.* **2022**, 2203703.

[12] T. Ma, R. Jacobs, J. Booske, D. Morgan, *J. Mater. Chem. C* **2021**, *9*, 12778.

[13] H. Hertz, *Ann. der Phys. und Chemie* **1887**, *267*, 983.

[14] W. Hallwachs, *Ann. der Phys. und Chemie* **1888**, *269*, 301.

[15] M. A. Stoletow, *London, Edinburgh, Dublin Philos. Mag. J. Sci.* **1888**, *26*, 317.

[16] J. Z. Buchwald, A. Warwick, *Histories of the electron: the birth of microphysics*, MIT Press, **2004**.

[17] P. Lenard, *Ann. Phys.* **1902**, *313*, 149.

[18] A. Einstein, *Am. J. Phys.* **1965**, *33*, 367.

[19] S. Klassen, *Sci. Educ.* **2011**, *20*, 719.

[20] R. A. Millikan, *Phys. Rev.* **1914**, *4*, 73.

[21] O. W. Richardson, *On the Negative Radiation from Hot Platinum...*, University Press, **1901**.

[22] O. W. Richardson, *J. Röntgen Soc.* **1922**, *18*, 150.

[23] C. Herring, M. H. Nichols, *Rev. Mod. Phys.* **1949**, *21*, 185.

[24] C. R. Crowell, *Solid State Electron.* **1965**, *8*, 395.

[25] W. Schottky, *Zeitschrift für Phys.* **1923**, *14*, 63.

[26] J. E. Lilienfeld, *Am. J. Roentgenol.* **1922**, *9*, 192.

[27] R. A. Millikan, C. F. Eyring, *Phys. Rev.* **1926**, *27*, 51.

[28] B. S. Gossling, *London, Edinburgh, Dublin Philos. Mag. J. Sci.* **1926**, *1*, 609.

[29] R. A. Millikan, C. C. Lauritsen, *Proc. Natl. Acad. Sci. U. S. A.* **1928**, *14*, 45.

[30] J. R. Oppenheimer, *Phys. Rev.* **1928**, *31*, 66.

[31] R. H. Fowler, L. Nordheim, *Proc. R. Soc. London. Ser. A, Contain. Pap. a Math. Phys. Character* **1928**, *119*, 173.

[32] R. Smoluchowski, *Phys. Rev.* **1941**, *60*, 661.

[33] R. Ahsan, M. A. Sakib, H. U. Chae, R. Kapadia, *Phys. Rev. Appl.* **2020**, *13*, 1.

[34] K. L. Jensen, *Introduction to the Physics of Electron Emission*, John Wiley & Sons, Ltd, **2017**.

[35] K. L. Jensen, *Electron emission physics*, Vol. 149, Elsevier, **2007**.

[36] S. Garbe, *Phys. Status Solidi* **1970**, *2*, 497.

[37] S. Xia, L. Liu, Y. Diao, Y. Kong, *J. Mater. Sci. 52*.

[38] Z. Cui, E. Li, X. Ke, T. Zhao, Y. Yang, Y. Ding, T. Liu, Y. Qu, S. Xu, *Appl. Surf. Sci.* **2017**, *423*, 829.

[39] W. He, S. Vilayurganapathy, A. G. Joly, T. C. Droubay, S. A. Chambers, J. R. Maldonado, W. P. Hess, *Appl. Phys. Lett.* **2013**, *102*, 071604.

[40] K. L. Jensen, M. McDonald, O. Chubenko, J. R. Harris, D. A. Shiffler, N. A. Moody, J. J. Petillo, A. J. Jensen, *J. Appl. Phys.* **2019**, *125*.

[41] H. Zhang, J. Tang, J. Yuan, J. Ma, N. Shinya, K. Nakajima, H. Murakami, T.

Ohkubo, L. C. Qin, *Nano Lett.* **2010**, *10*, 3539.

[42] M. Nakamoto, T. Hasegawa, T. Ono, T. Sakai, N. Sakuma, In *Technical Digest - International Electron Devices Meeting, IEDM*, **1996**, pp. 297–300.

[43] M. Nakamoto, J. Moon, *J. Vac. Sci. Technol. B, Nanotechnol. Microelectron. Mater. Process. Meas. Phenom.* **2011**, *29*, 02B112.

[44] R. U. Martinelli, D. G. Fisher, *Proc. IEEE* **1974**, *62*, 1339.

[45] J. Van Der Weide, Z. Zhang, P. K. Baumann, M. G. Wensell, J. Bernholc, R. J. Nemanich, *Phys. Rev. B* **1994**, *50*, 5803.

[46] R. J. Nemanich, P. K. Baumann, M. C. Benjamin, S. W. King, J. Van Der Weide, R. F. Davis, *Diam. Relat. Mater.* **1996**, *5*, 790.

[47] I. V. Bazarov, B. M. Dunham, Y. Li, X. Liu, D. G. Ouzounov, C. K. Sinclair, F. Hannon, T. Miyajima, *J. Appl. Phys.* **2008**, *103*, 054901.

[48] H. Yamaguchi, T. Masuzawa, S. Nozue, Y. Kudo, I. Saito, J. Koe, M. Kudo, T. Yamada, Y. Takakuwa, K. Okano, *Phys. Rev. B - Condens. Matter Mater. Phys.* **2009**, *80*, 165321.

[49] F. Rezaeifar, R. Ahsan, Q. Lin, H. U. Chae, R. Kapadia, *Nat. Photonics 2019 1312* **2019**, *13*, 843.

[50] F. Rezaeifar, H. U. Chae, R. Ahsan, R. Kapadia, *Appl. Phys. Lett.* **2021**, *118*, 071108.

[51] G. Gaertner, D. Den Engelsen, *Appl. Surf. Sci.* **2005**, *251*, 24.

[52] G. A. Haas, *J. Appl. Phys.* **1957**, *28*, 1486.

[53] L. E. Grey, *Nature* **1950**, *165*, 773.

[54] M. Futamoto, M. Nakazawa, K. Usami, S. Hosoki, U. Kawabe, *J. Appl. Phys.* **1980**, *51*, 3869.

[55] M. Futamoto, M. Nakazawa, U. Kawabe, *Surf. Sci.* **1980**, *100*, 470.

[56] G. H. Olsen, A. V. Cafiero, *J. Cryst. Growth* **1978**, *44*, 287.

[57] J. A. J. M. Deckers, T. H. Weekers, A. Manenschijn, F. M. M. Snijkers, P. A. M. Van Der Heide, *Dispenser cathode and method of manufacturing a dispenser cathode*, Google Patents, **1997**.

[58] M. N. Seif, Q. Zhou, X. Liu, T. J. Balk, M. J. Beck, *IEEE Trans. Electron Devices* **2022**.

[59] M. N. Seif, Q. Zhou, X. Liu, T. J. Balk, M. J. Beck, *IEEE Trans. Electron Devices*

2022, *69*, 3523.

[60] R. Garg, N. Dutta, N. Choudhury, *Nanomaterials* **2014**, *4*, 267.

[61] S. Halas, T. Durakiewicz, *Appl. Surf. Sci.* **2006**, *252*, 6119.

[62] M. P. Kirley, B. Novakovic, N. Sule, M. J. Weber, I. Knezevic, J. H. Booske, *J. Appl. Phys.* **2012**, *111*.

[63] H. Yamauchi, K. Takagi, I. Yuito, U. Kawabe, *Appl. Phys. Lett.* **1976**, *29*, 638.

[64] R. Jenkins, *Vacuum* **1969**, *19*, 353.

[65] Q. Zhou, X. Liu, T. Maxwell, B. Vancil, T. J. Balk, M. J. Beck, *Appl. Surf. Sci.* **2018**, *458*, 827.

[66] M. N. Seif, Q. Zhou, X. Liu, T. J. Balk, M. J. Beck, **2022**.

[67] R. Jacobs, J. Booske, D. Morgan, *Adv. Funct. Mater.* **2016**, *26*, 5471.

[68] S. M. Sze, K. K. Ng, *Physics of semiconductor devices*, John wiley & sons, **2006**.

[69] J. Tersoff, *Phys. Rev. Lett.* **1984**, *52*, 465.

[70] G. Çankaya, N. Uçar, *Zeitschrift fur Naturforsch. - Sect. A J. Phys. Sci.* **2004**, *59*, 795.

[71] M. Minohara, R. Yasuhara, H. Kumigashira, M. Oshima, *Phys. Rev. B - Condens. Matter Mater. Phys.* **2010**, *81*, 1.

[72] J. L. Freeouf, J. M. Woodall, *Appl. Phys. Lett.* **1981**, *39*, 727.

[73] A. C. Schmilz, A. T. Ping, M. Asif Khan, Q. Chen, J. W. Yang, I. Adesida, *Semicond. Sci. Technol.* **1996**, *11*, 1464.

[74] Y. Zhou, C. Fuentes-hernandez, J. Shim, J. Meyer, A. J. Giordano, H. Li, P. Winget, T. Papadopoulos, H. Cheun, J. Kim, M. Fenoll, A. Dindar, W. Haske, E. Najafabadi, T. M. Khan, H. Sojoudi, S. Barlow, S. Graham, J. Brédas, S. R. Marder, A. Kahn, B. Kippelen, *Science (80-.).* **2012**, *336*, 327.

[75] S. Heinze, J. Tersoff, R. Martel, V. Derycke, J. Appenzeller, P. Avouris, *Phys. Rev. Lett.* **2002**, *89*, 2.

[76] S. Deb, N. B. Singh, N. Islam, S. K. Sarkar, *IEEE Trans. Nanotechnol.* **2012**, *11*, 472.

[77] P. Saha, S. Sarkhel, S. K. Sarkar, *J. Comput. Electron.* **2017**, *16*, 648.

[78] A. Bhalla, S. K. Lui, *MOSFET using gate work function engineering for switching*

applications, Google Patents, **2012**.

[79] C. G. Vayenas, S. Bebelis, C. Pliangos, S. Brosda, D. Tsiplakides, *Electrochemical activation of catalysis: promotion, electrochemical promotion, and metal-support interactions*, Springer, **2001**.

[80] J. Y. Cheon, J. H. Kim, J. H. Kim, K. C. Goddeti, J. Y. Park, S. H. Joo, *J. Am. Chem. Soc.* **2014**, *136*, 8875.

[81] K. A. Stoerzinger, M. Risch, J. Suntivich, W. M. Lü, J. Zhou, M. D. Biegalski, H. M. Christen, Ariando, T. Venkatesan, S. H. Yang, *Energy Environ. Sci.* **2013**, *6*, 1582.

[82] W. T. Hong, K. A. Stoerzinger, B. Moritz, T. P. Devereaux, W. Yang, Y. Shao-Horn, *J. Phys. Chem. C* **2015**, *119*, 2063.

[83] S. Trasatti, *Electrochim. Acta* **1991**, *36*, 1659.

[84] F. Calle-Vallejo, M. T. M. Koper, A. S. Bandarenka, *Chem. Soc. Rev.* **2013**, *42*, 5210.

[85] B. Łosiewicz, M. Popczyk, I. Napłoszek, A. Budniok, *Solid State Phenom.* **2015**, *228*, 16.

[86] G. Kumar, S. Lap, J. Lau, M. D. Krcha, M. J. Janik, **2016**.

[87] R. Jacobs, J. Hwang, Y. Shao-Horn, D. Morgan, *Chem. Mater.* **2019**, *31*, 785.

[88] R. Jacobs, T. Mayeshiba, J. Booske, D. Morgan, *Adv. Energy Mater.* **2018**, *8*, 1702708.

[89] L. Giordano, K. Akkiraju, R. Jacobs, D. Vivona, D. Morgan, Y. Shao-Horn, *Acc. Chem. Res.* **2022**, *55*, 298.

[90] A. Grimaud, K. J. May, C. E. Carlton, Y. L. Lee, M. Risch, W. T. Hong, J. Zhou, Y. Shao-Horn, *Nat. Commun. 2013 41* **2013**, *4*, 1.

[91] D. Lee, Y. L. Lee, W. T. Hong, M. D. Biegalski, D. Morgan, Y. Shao-Horn, *J. Mater. Chem. A* **2015**, *3*, 2144.

[92] L. Tang, X. Meng, D. Deng, X. Bao, *Adv. Mater.* **2019**, *31*, 1.

[93] D. Vogel, C. Spiel, Y. Suchorski, A. Urich, R. Schlögl, G. Rupprechter, *Surf. Sci.* **2011**, *605*, 1999.

[94] K. A. A. Khalid, T. J. Leong, K. Mohamed, *IEEE Trans. Electron Devices* **2016**, *63*, 2231.

[95] F. Morini, E. Dubois, J. F. Robillard, S. Monfray, T. Skotnicki, *Phys. Status Solidi*

Appl. Mater. Sci. **2014**, *211*, 1334.

[96] B. Qi, J. Wang, *J. Mater. Chem.* **2012**, *22*, 24315.

[97] E. Centurioni, D. Iencinella, *Role of front contact work function on amorphous silicon/crystalline silicon heterojunction solar cell performance*, Vol. 24, **2003**, pp. 177–179.

[98] E. Fortunato, D. Ginley, H. Hosono, D. C. Paine, *MRS Bull.* **2007**, *32*, 242.

[99] A. Klein, C. Körber, A. Wachau, F. Säuberlich, Y. Gassenbauer, S. P. Harvey, D. E. Proffit, T. O. Mason, *Materials (Basel).* **2010**, *3*, 4892.

[100] R. Rössler, C. Leendertz, L. Korte, N. Mingirulli, B. Rech, *J. Appl. Phys.* **2013**, *113*.

[101] C. Quarti, F. De Angelis, D. Beljonne, *Chem. Mater.* **2017**, *29*, 958.

[102] P. H. Lee, T. T. Wu, K. Y. Tian, C. F. Li, C. H. Hou, J. J. Shyue, C. F. Lu, Y. C. Huang, W. F. Su, *ACS Appl. Mater. Interfaces* **2020**, *12*, 45936.

[103] M. F. Mohamad Noh, C. H. Teh, R. Daik, E. L. Lim, C. C. Yap, M. A. Ibrahim, N. Ahmad Ludin, A. R. Bin Mohd Yusoff, J. Jang, M. A. Mat Teridi, *The architecture of the electron transport layer for a perovskite solar cell*, Vol. 6, Royal Society of Chemistry, **2018**, pp. 682–712.

[104] A. Varpula, S. J. Laakso, T. Havia, J. Kyynäräinen, M. Prunnila, *Sci. Reports 2014 41* **2014**, *4*, 1.

[105] C. Beasley, M. Kumaran Gnanamani, E. Santillan-Jimenez, M. Martinelli, W. D. Shafer, S. D. Hopps, N. Wanninayake, D. Y. Kim, *ChemistrySelect* **2020**, *5*, 1013.

[106] K. H. Ye, H. Li, D. Huang, S. Xiao, W. Qiu, M. Li, Y. Hu, W. Mai, H. Ji, S. Yang, *Nat. Commun.* **2019**, *10*, 1.

[107] Y. Gao, Z. Wang, L. Chen, *J. Mater. Chem. A* **2015**, *3*, 23420.

[108] R. E. Warburton, J. J. Kim, S. Patel, J. D. Howard, L. A. Curtiss, C. Wolverton, D. B. Buchholz, J. T. Vaughey, P. Fenter, T. T. Fister, J. Greeley, *Chem. Mater.* **2021**, *33*, 8447.

[109] F. Li, X. Gao, R. Wang, T. Zhang, G. Lu, *Sensors Actuators, B Chem.* **2017**, *248*, 812.

[110] D. Cahen, A. Kahn, *Adv. Mater.* **2003**, *15*, 271.

[111] D. Chen, R. Jacobs, D. Morgan, J. Booske, *IEEE Trans. Electron Devices* **2021**, *68*, 3576.

[112] J. Trigueiro, N. Bundaleski, A. G. Silva, O. M. N. D. Teodoro, *Vacuum* **2013**, *98*,

41.

[113] A. Kahn, *Mater. Horizons* **2016**, *3*, 7.

[114] H. Ishii, K. Sugiyama, E. Ito, K. Seki, .

[115] C. Kittel, P. McEuen, *Introduction to solid state physics*, Vol. 8, Wiley New York, **1996**.

[116] K. Oura, V. G. Lifshits, A. A. Saranin, A. V Zotov, M. Katayama, *Surface science: an introduction*, Springer Science & Business Media, **2013**.

[117] W. Kohn, N. D. Lang, *Phys. Rev. B* **1971**, *3*, 1215.

[118] K. C. Kwon, K. S. Choi, S. Y. Kim, *Adv. Funct. Mater.* **2012**, *22*, 4724.

[119] M. T. Greiner, L. Chai, M. G. Helander, W. M. Tang, Z. H. Lu, *Adv. Funct. Mater.* **2012**, *22*, 4557.

[120] X. Peng, F. Tang, A. Copple, *J. Phys. Condens. Matter* **2012**, *24*.

[121] Z. Zhong, P. Hansmann, *Phys. Rev. B* **2016**, *93*, 1.

[122] T. Ma, R. Jacobs, J. Booske, D. Morgan, *APL Mater.* **2020**, *8*.

[123] V. Vlahos, J. H. Booske, D. Morgan, *Phys. Rev. B* **2010**, *81*, 054207.

[124] V. Vlahos, Y. L. Lee, J. H. Booske, D. Morgan, L. Turek, M. Kirshner, R. Kowalczyk, C. Wilsen, *Appl. Phys. Lett.* **2009**, *94*, 2007.

[125] G. N. Derry, P. N. Ross, *J. Chem. Phys.* **1998**, *82*, 2772.

[126] T. Schultz, J. Niederhausen, R. Schlesinger, *J. Appl. Phys* **2018**, *123*, 245501.

[127] H. L. Skriver, N. M. Rosengaard, *Phys. Rev. B* **1992**, *46*, 7157.

[128] H. B. Michaelson, *J. Appl. Phys.* **1977**, *48*, 4729.

[129] J. J. Uebbing, L. W. James, *J. Appl. Phys.* **1970**, *41*, 4505.

[130] K. Shen, R. Yang, D. Wang, M. Jeng, S. Chaudhary, K. Ho, D. Wang, *Sol. Energy Mater. Sol. Cells* **2016**, *144*, 500.

[131] T. Susaki, A. Makishima, H. Hosono, *Phys. Rev. B - Condens. Matter Mater. Phys.* **2011**, *84*, 2.

[132] S. A. Chambers, P. V. Sushko, *Phys. Rev. Mater.* **2019**, *3*, 125803.

[133] F. Hess, B. Yildiz, *Phys. Rev. Mater.* **2020**, *4*, 15801.

[134] N. Erdman, O. Warschkow, M. Asta, K. R. Poeppelmeier, D. E. Ellis, L. D. Marks, *J. Am. Chem. Soc.* **2003**, *125*, 10050.

[135] J. W. Harter, L. Maritato, D. E. Shai, E. J. Monkman, Y. Nie, D. G. Schlom, K. M. Shen, *Phys. Rev. B - Condens. Matter Mater. Phys.* **2015**, *92*, 035149.

[136] S. Hong, S. M. Nakhmanson, D. D. Fong, *Screening mechanisms at polar oxide heterointerfaces*, Vol. 79, Institute of Physics Publishing, **2016**, p. 076501.

[137] Y. L. Lee, D. Morgan, *Phys. Rev. B - Condens. Matter Mater. Phys.* **2015**, *91*, 195430.

[138] K. C. L. Bauerfeind, R. Roß, T. Bredow, *J. Phys. Chem. C* **2020**, *124*, 28520.

[139] H. Yuan, S. Chang, I. Bargatin, N. C. Wang, D. C. Riley, H. Wang, J. W. Schwede, J. Provine, E. Pop, Z. X. Shen, P. A. Pianetta, N. A. Melosh, R. T. Howe, *Nano Lett.* **2015**, *15*, 6475.

[140] A. Di Vito, A. Pecchia, M. Auf der Maur, A. Di Carlo, *Adv. Funct. Mater.* **2020**, *1909028*, 1.

[141] C. Leung, L. Kao, S. Su, J. Feng, T. Chan, *Phys. Rev. B - Condens. Matter Mater. Phys.* **2003**, *68*, 1.

[142] P. R. Norton, J. W. Goodale, E. B. Selkirk, *Surf. Sci.* **1979**, *83*, 189.

[143] F. Gossenberger, T. Roman, K. Forster-Tonigold, A. Groß, *Beilstein J. Nanotechnol* **2014**, *5*, 152.

[144] G. S. Tompa, W. E. Carr, M. Seidl, *Appl. Phys. Lett.* **1986**, *49*, 1511.

[145] Y. Joo, M. Jin, S. K. Kim, S. K. Kim, D. Um, C. Kim, *Appl. Surf. Sci.* **2021**, 149957.

[146] M. Bruening, E. Moons, D. Cahen, A. Shanzer, *J. Phys. Chem.* **1995**, *99*, 8368.

[147] S. Hüfner, *Photoelectron spectroscopy: principles and applications*, Springer Science & Business Media, **2013**.

[148] Y. Park, V. Choong, Y. Gao, B. R. Hsieh, C. W. Tang, *Appl. Phys. Lett.* **1996**, *68*, 2699.

[149] T. Schultz, T. Lenz, N. Kotadiya, G. Heimel, G. Glasser, R. Berger, P. W. M. Blom, P. Amsalem, D. M. de Leeuw, N. Koch, *Adv. Mater. Interfaces* **2017**, *4*, 1.

[150] M. G. Helander, M. T. Greiner, Z. B. Wang, Z. H. Lu, *Appl. Surf. Sci.* **2010**, *256*, 2602.

[151] S. Gutmann, M. Conrad, M. A. Wolak, M. M. Beerbom, R. Schlaf, *J. Appl. Phys.* **2012**, *111*.

[152] A. Sharma, M. Untch, J. S. Quinton, R. Berger, G. Andersson, D. A. Lewis, *Appl. Surf. Sci.* **2016**, *363*, 516.

[153] M. J. Morant, H. House, *Proc. Phys. Soc. Sect. B* **1956**, *69*, 14.

[154] Y. Wan, Y. Li, Q. Wang, K. Zhang, Y. Wu, *Int. J. Electrochem. Sci.* **2012**, *7*, 5204.

[155] W. Li, D. Y. Li, *J. Chem. Phys.* **2005**, *122*.

[156] M. Xue, S. Peng, F. Wang, J. Ou, C. Li, W. Li, *J. Alloys Compd.* **2017**, *692*, 903.

[157] J. Kaur, R. Kant, *J. Phys. Chem. C* **2017**, *121*, 13059.

[158] N. Nakagiri, H. Kaizuka, *Jpn. J. Appl. Phys.* **1990**, *29*, 744.

[159] Z. Knor, *Surf. Sci.* **1986**, *169*, 317.

[160] G. I. Kuznetsov, E. A. Sokolovsky, *Phys. Scr.* **1997**, *1997*, 130.

[161] W. Y. Li, K. Goto, R. Shimizu, *Surf. Interface Anal.* **2005**, *37*, 244.

[162] O. Renault, R. Brochier, A. Roule, P. H. Haumesser, B. Krömker, D. Funnemann, *Surf. Interface Anal.* **2006**, *38*, 375.

[163] W. Engel, M. E. Kordesch, H. H. Rotermund, S. Kubala, A. von Oertzen, *Ultramicroscopy* **1991**, *36*, 148.

[164] C. Wang, M. E. Kordesch, *Ultramicroscopy* **1991**, *36*, 154.

[165] K. Wandelt, *Appl. Surf. Sci.* **1997**, *111*, 1.

[166] U. Zerweck, C. Loppacher, T. Otto, S. Grafström, L. M. Eng, *Phys. Rev. B - Condens. Matter Mater. Phys.* **2005**, *71*, 1.

[167] M. Nonnenmacher, M. P. O'Boyle, H. K. Wickramasinghe, *Appl. Phys. Lett.* **1998**, *58*, 2921.

[168] W. Melitz, J. Shen, A. C. Kummel, S. Lee, *Surf. Sci. Rep.* **2011**, *66*, 1.

[169] J. S. Kim, B. Lägel, E. Moons, N. Johansson, I. D. Baikie, W. R. Salaneck, R. H. Friend, F. Cacialli, *Synth. Met.* **2000**, *111*, 311.

[170] M. M. Beerbom, B. Lägel, A. J. Cascio, B. V. Doran, R. Schlaf, *J. Electron Spectros. Relat. Phenomena* **2006**, *152*, 12.

[171] S. Dushman, *Rev. Mod. Phys.* **1930**, *2*, 381.

[172] C. Davisson, L. H. Germer, *Phys. Rev.* **1922**, *20*, 300.

[173] C. Davisson, L. H. Germer, *Phys. Rev.* **1927**, *30*, 634.

[174] V. S. Fomenko, *Handbook of Thermionic Properties* (Eds.: Fomenko, V. S.; Samsonov, G. V.), Springer US, Boston, MA, **1966**.

[175] J. Voss, A. Vojvodic, S. H. Chou, R. T. Howe, I. Bargatin, F. Abild-Pedersen, *J. Chem. Phys.* **2013**, *138*, 204701.

[176] H. Shelton, *Phys. Rev.* **1957**, *107*, 1553.

[177] F. A. M. Koeck, R. J. Nemanich, A. Lazea, K. Haenen, *Diam. Relat. Mater.* **2009**, *18*, 789.

[178] D. Chen, Modeling Nonuniform Thermionic Emission from Heterogeneous Cathodes, University of Wisconsin-Madison, **2022**.

[179] S.-Y. Ning, T. Iitaka, X.-Y. Yang, Y. Wang, J.-J. Zhao, Z. Li, J.-X. Zhang, *J. Alloys Compd.* **2018**, *760*, 1.

[180] E. B. Hensley, *J. Appl. Phys.* **1961**, *32*, 301.

[181] R. A. Tuck, *Appl. Surf. Sci.* **1979**, *2*, 128.

[182] M. E. Kordesch, J. M. Vaughn, C. Wan, K. D. Jamison, *J. Vac. Sci. Technol. B* **2011**, *29*, 4.

[183] X. Lu, Q. Yang, W. Chen, C. Xiao, A. Hirose, *J. Vac. Sci. Technol. B Microelectron. Nanom. Struct.* **2006**, *24*, 2575.

[184] R. G. Forbes, *Ultramicroscopy* **1999**, *79*, 11.

[185] R. G. Forbes, J. H. B. Deane, A. Fischer, M. S. Mousa, **2015**.

[186] M.-C. Lin, Y.-H. Liao, *J. Vac. Sci. Technol. B Microelectron. Nanom. Struct.* **2008**, *26*, 826.

[187] D. A. Shiffler, W. Tang, K. L. Jensen, K. Golby, M. LaCour, J. J. Petillo, J. R. Harris, *J. Appl. Phys.* **2015**, *118*, 083302.

[188] E. Wigner, J. Bardeen, *Phys. Rev.* **1935**, *48*, 84.

[189] J. Bardeen, *Phys. Rev.* **1936**, *49*, 653.

[190] V. Russier, J. P. Badiali, *Phys. Rev. B* **1989**, *39*, 13193.

[191] P. Hohenberg, W. Kohn, *Phys. Rev.* **1964**, *136*, B864.

[192] C. J. Fall, N. Binggeli, A. Baldereschi, *J. Phys. Condens. Matter* **1999**, *11*, 2689.

[193] S. De Waele, K. Lejaeghere, M. Sluydts, S. Cottenier, *Phys. Rev. B* **2016**, *94*, 235418.

[194] R. Tran, X.-G. Li, J. H. Montoya, D. Winston, K. A. Persson, S. P. Ong, *Surf. Sci.* **2019**, *687*, 48.

[195] M. Uijttewaal, G. De Wijs, R. De Groot, *J. Phys. Chem. B* **2006**, *110*, 18459.

[196] K. M. Schmidt, S. T. Misture, O. A. Graeve, V. R. Vasquez, *Adv. Electron. Mater.* **2019**, *5*, 1800074.

[197] M. G. Quesne, A. Roldan, N. H. De Leeuw, C. R. A. Catlow, *Phys. Chem. Chem. Phys.* **2018**, *20*, 6905.

[198] Y. Murata, E. Starodub, B. B. Kappes, C. V. Ciobanu, N. C. Bartelt, K. F. McCarty, S. Kodambaka, *Appl. Phys. Lett.* **2010**, *97*, 143114.

[199] B. Wang, S. Günther, J. Wintterlin, M. L. Bocquet, *New J. Phys.* **2010**, *12*, 43041.

[200] G. Giovannetti, P. A. Khomyakov, G. Brocks, V. M. Karpan, J. Van Den Brink, P. J. Kelly, **2008**.

[201] H. A. Tahini, X. Tan, S. C. Smith, *Nanoscale* **2017**, *9*, 7016.

[202] R. Jacobs, D. Morgan, J. Booske, *APL Mater.* **2017**, *5*, 116105.

[203] K. A. Stoerzinger, R. Comes, S. R. Spurgeon, S. Thevuthasan, K. Ihm, E. J. Crumlin, S. A. Chambers, *J. Phys. Chem. Lett.* **2017**, *8*, 1038.

[204] M. Chagas Da Silva, M. Lorke, B. Aradi, M. Farzalipour Tabriz, T. Frauenheim, A. Rubio, D. Rocca, P. Deák, *Phys. Rev. Lett.* **2021**, *126*, 76401.

[205] J. Heyd, G. E. Scuseria, M. Ernzerhof, *J. Chem. Phys.* **2003**, *118*, 8207.

[206] N. Li, T. Zong, Z. Zhang, In *2021 IEEE 6th International Conference on Big Data Analytics, ICBDA 2021*, Institute of Electrical and Electronics Engineers Inc., **2021**, pp. 87–91.

[207] Y. Xiong, W. Chen, W. Guo, H. Wei, I. Dabo, *Phys. Chem. Chem. Phys.* **2021**, *23*, 6880.

[208] W. Hashimoto, Y. Tsuji, K. Yoshizawa, *J. Phys. Chem. C* **2020**, *124*, 9958.

[209] P. Schindler, E. R. Antoniuk, G. Cheon, Y. Zhu, E. J. Reed, *arXiv* **2020**.

[210] M. Grätzel, *Nature* **2001**, *414*, 338.

[211] M. T. Greiner, Z. H. Lu, *NPG Asia Mater.* **2013**, *5*, e55.

[212] M. T. Greiner, M. G. Helander, W. M. Tang, Z. Bin Wang, J. Qiu, Z. H. Lu, *Nat.*

Mater. **2012**, *11*, 76.

[213] C. J. Brabec, A. Cravino, D. Meissner, N. S. Sariciftci, M. T. Rispens, L. Sanchez, J. C. Hummelen, T. Fromherz, *Thin Solid Films* **2002**, *403–404*, 368.

[214] H. Frohne, S. E. Shaheen, C. J. Brabec, D. C. Müller, N. S. Sariciftci, K. Meerholz, *ChemPhysChem* **2002**, *3*, 795.

[215] A. S. Gilmour, *Principles of traveling wave tubes*, Artech House, **1994**.

[216] G. Gärtner, P. Geittner, H. Lydtin, A. Ritz, *Appl. Surf. Sci.* **1997**, *111*, 11.

[217] D. Wang, T. Kako, J. Ye, *J. Phys. Chem. C* **2009**, *113*, 3785.

[218] M. Stars, N. Galaxies, *Nature* **1994**, *372*, 532.

[219] M. Suzuki, T. Ami, *Mater. Sci. Eng. B* **1996**, *41*, 166.

[220] Y. Wang, Z. Lv, L. Zhou, X. Chen, J. Chen, Y. Zhou, V. A. L. Roy, S. T. Han, *J. Mater. Chem. C* **2018**, *6*, 1600.

[221] B. Nagaraj, T. Sawhney, S. Perusse, S. Aggarwal, R. Ramesh, V. S. Kaushik, S. Zafar, R. E. Jones, J. H. Lee, V. Balu, J. Lee, *Appl. Phys. Lett.* **1999**, *74*, 3194.

[222] G. Srinivasan, E. T. Rasmussen, B. J. Levin, R. Hayes, *Phys. Rev. B - Condens. Matter Mater. Phys.* **2002**, *65*, 1.

[223] M. A. Peña, J. L. G. Fierro, *Chem. Rev.* **2001**, *101*, 1981.

[224] T. Maekawa, K. Kurosaki, S. Yamanaka, *J. Alloys Compd.* **2006**, *426*, 46.

[225] M. Karolak, T. O. Wehling, F. Lechermann, A. I. Lichtenstein, *J. Phys. Condens. Matter* **2011**, *23*.

[226] J. A. Moyer, C. Eaton, R. Engel-Herbert, *Adv. Mater.* **2013**, *25*, 3578.

[227] X. M. Ge, S. H. Chan, Q. L. Liu, Q. Sun, *Adv. Energy Mater.* **2012**, *2*, 1156.

[228] S. Hui, A. Petric, *Solid State Ionics* **2001**, *143*, 275.

[229] A. A. Yaremchenko, B. Brinkmann, R. Janssen, J. R. Frade, *Solid State Ionics* **2013**, *247–248*, 86.

[230] T. Kida, G. Guan, A. Yoshida, *Chem. Phys. Lett.* **2003**, *371*, 563.

[231] S. P. S. Badwal, T. Bak, S. P. Jiang, J. Love, J. Nowotny, M. Rekas, C. C. Sorrell, E. R. Vance, *J. Phys. Chem. Solids* **2001**, *62*, 723.

[232] L. F. Zagonel, M. Bäurer, A. Bailly, O. Renault, M. Hoffmann, S. J. Shih, D.

Cockayne, N. Barrett, *J. Phys. Condens. Matter* **2009**, *21*.

[233] H. Falcón, J. A. Alonso, M. T. Casais, M. J. Martínez-Lope, J. Sánchez-Benítez, *J. Solid State Chem.* **2004**, *177*, 3099.

[234] A. Aguadero, C. De La Calle, D. Pérez-Coll, J. A. Alonso, *Fuel Cells* **2011**, *11*, 44.

[235] A. Majid, J. Tunney, S. Argue, D. Wang, M. Post, J. Margeson, *J. Alloys Compd.* **2005**, *398*, 48.

[236] S. D. Marks, L. Lin, P. Zuo, P. J. Strohbeen, R. Jacobs, D. Du, J. R. Waldvogel, R. Liu, D. E. Savage, J. H. Booske, J. K. Kawasaki, S. E. Babcock, D. Morgan, P. G. Evans, *Phys. Rev. Mater.* **2021**, *5*, 83402.

[237] D. D. Wagman, J. E. Kilpatrick, W. J. Taylor, K. S. Pitzer, F. D. Rossini, *J. Res. Natl. Bur. Stand* **1945**, *34*, 143.

[238] A. Adamson, *A textbook of physical chemistry*, Elsevier, **2012**.

[239] C. J. Bartel, A. W. Weimer, S. Lany, C. B. Musgrave, A. M. Holder, *npj Comput. Mater. 2019 51* **2019**, *5*, 1.

[240] W. Sun, S. T. Dacek, S. P. Ong, G. Hautier, A. Jain, W. D. Richards, A. C. Gamst, K. A. Persson, G. Ceder, *Sci. Adv.* **2016**, *2*.

[241] D. Cahen, A. Kahn, *Adv. Mater.* **2003**, *15*, 271.

[242] G. Kresse, J. Furthmüller, *Phys. Rev. B* **1996**, *54*, 169.

[243] G. Kresse, D. Joubert, *Phys. Rev. B* **1999**, *59*, 1758.

[244] J. P. Perdew, K. Burke, M. Ernzerhof, *Phys. Rev. Lett.* **1996**, *77*, 3865.

[245] H. J. Monkhorst, J. D. Pack, *NUMBER* **1976**, *13*.

[246] J. Hubbard, *Proc. R. Soc. London. Ser. A. Math. Phys. Sci.* **1963**, *276*, 238.

[247] L. Wang, T. Maxisch, G. Ceder, *Phys. Rev. B - Condens. Matter Mater. Phys.* **2006**, *73*, 195107.

[248] A. Jain, P. Ong, G. Hautier, S. P. Ong, W. Chen, W. D. Richards, S. Dacek, S. Cholia, D. Gunter, D. Skinner, G. Ceder, K. A. Persson, *Cite as APL Mater* **2013**, *1*, 11002.

[249] S. Ping Ong, W. Davidson Richards, A. Jain, G. Hautier, M. Kocher, S. Cholia, D. Gunter, V. L. Chevrier, K. A. Persson, G. Ceder, **2012**.

[250] Y. C. Lan, X. L. Chen, M. He, *J. Alloys Compd.* **2003**, *354*, 95.

[251] Y. Bourlier, M. Frégnaux, B. Bérini, A. Fouchet, Y. Dumont, D. Aureau, *Appl. Surf.*

Sci. **2021**, *553*, 149536.

[252] B. Bérini, V. Demange, M. Bouttemy, E. Popova, N. Keller, Y. Dumont, A. Fouchet, *Adv. Mater. Interfaces* **2016**, *3*, 6.

[253] K. Huang, L. Yuan, S. Feng, *Inorg. Chem. Front.* **2015**, *2*, 965.

[254] S. Kim, M. Aykol, C. Wolverton, *Phys. Rev. B - Condens. Matter Mater. Phys.* **2015**, *92*, 115411.

[255] J. Druce, H. Tellez, M. Burriel, M. D. Sharp, L. J. Fawcett, S. N. Cook, D. S. McPhail, T. Ishihara, H. H. Brongersma, J. A. Kilner, *Energy \& Environ. Sci.* **2014**, *7*, 3593.

[256] Z. Feng, W. T. Hong, D. D. Fong, Y. L. Lee, Y. Yacoby, D. Morgan, Y. Shao-Horn, *Acc. Chem. Res.* **2016**, *49*, 966.

[257] Y. Kanke, K. Kato, E. Takayama-Muromachi, M. Isobe, *Acta Crystallogr. Sect. C* **1992**, *48*, 1376.

[258] Y. Bourlier, M. Frégnaux, B. Bérini, A. Fouchet, Y. Dumont, D. Aureau, *ChemNanoMat* **2019**, 1.

[259] L. K. Hansen, *J. Appl. Phys.* **1966**, *37*, 4498.

[260] M. Cattelino, G. Miram, **1997**, *111*, 90.

[261] J. E. Davey, *J. Appl. Phys.* **1957**, *28*, 1031.

[262] A. H. Sommer, *J. Appl. Phys.* **1980**, *51*, 1254.

[263] H. R. Philipp, *Phys. Rev.* **1957**, *107*, 687.

[264] S. J. Schneider, *Compilation of melting points of the metal oxides*, Vol. 68, US Department of Commerce, National Bureau of Standards, **1963**.

[265] T. Ma, R. Jacobs, J. Booske, D. Morgan, *J. Phys. Chem. C* **2021**, *125*, 17400.

[266] K. Kurosaki, T. Oyama, H. Muta, M. Uno, S. Yamanaka, *J. Alloys Compd.* **2004**, *372*, 65.

[267] T. Berry, S. Bernier, G. Auffermann, T. M. Mcqueen, W. A. Phelan, *J. Cryst. Growth* **2022**, *583*.